

UNCLASSIFIED

III F-COPY

2

SECURITY CLASSIFICATION OF THIS PAGE

AD-A201 067

Form Approved OMB No. 0704-0188

REPORT DOCUMENTATION

1a. REPORT SECURITY CLASSIFICATION UNCLASSIFIED		1b. RESTRICTIVE MARKINGS	
2a. SECURITY CLASSIFICATION AUTHORITY UNCLASSIFIED		3. DISTRIBUTION / AVAILABILITY OF REPORT Approved for public release; distribution unlimited.	
2b. DECLASSIFICATION / DOWNGRADING SCHEDULE OCT 06 1988		4. PERFORMING ORGANIZATION REPORT NUMBER(S) University of California Materials Department	
6a. NAME OF PERFORMING ORGANIZATION University of California Materials Department		5. MONITORING ORGANIZATION REPORT NUMBER(S) AFOSR-TR-88-1016	
6b. OFFICE SYMBOL (if applicable) ENMT		7a. NAME OF MONITORING ORGANIZATION AFOSR	
6c. ADDRESS (City, State, and ZIP Code) College of Engineering University of California Santa Barbara, CA 93106		7b. ADDRESS (City, State, and ZIP Code) Bldg. 410 Bolling AFB, DC 20332-6448	
8a. NAME OF FUNDING / SPONSORING ORGANIZATION AIR FORCE		8b. OFFICE SYMBOL (if applicable) AFOSR	
8c. ADDRESS (City, State, and ZIP Code) AFOSR/NE Building 410 Bolling AFB, D.C. 20332-6448		9. PROCUREMENT INSTRUMENT IDENTIFICATION NUMBER AFOSR-87-0291	
10. SOURCE OF FUNDING NUMBERS			
PROGRAM ELEMENT NO. 61108F	PROJECT NO. 2306	TASK NO. A2	WORK UNIT ACCESSION NO.
11. TITLE (Include Security Classification) <u>Unclassified</u> "Partitioning Resources to Develop and Control Unique Ceramic Microstructures"			
12. PERSONAL AUTHOR(S) Fred F. Lange and Manfred Rühle			
13a. TYPE OF REPORT Annual Interim Report		13b. TIME COVERED FROM 6/15/87 TO 6/14/88	
14. DATE OF REPORT (Year, Month, Day) 1988 July 31		15. PAGE COUNT 86	
16. SUPPLEMENTARY NOTATION (TRANSMISSION ELECTRON MICROSCOPY)			
17. COSATI CODES			18. SUBJECT TERMS (Continue on reverse if necessary and identify by block number) Ceramic Microstructures
FIELD	GROUP	SUB-GROUP	
19. ABSTRACT (Continue on reverse if necessary and identify by block number) ZIRCONIUM Dioxide TEM studies for different ZrO ₂ ceramics are reported. Observations are described to characterize the atomistic defects present in Mg-PSZ. TEM is applied to study phase stability and transformation in Y-TZP. The nucleation of stable m-ZrO ₂ at stress singularities associated with grain boundaries was studied in situ and related to strains and strain distributions determined by high resolution electron microscopy. The effect of grain growth on the morphological stability of polycrystalline fibers, constrained by a matrix, was determined. Analogous to thin films, grain growth was observed to cause the fiber to break-up into individual grains when the grain size to fiber diameter ratio exceeded a critical value. Calculations show that the free energy of the system continuously decreases as this break-up occurs. These results are important when polycrystalline fibers are intended to reinforce a matrix to produce a stronger composite material, viz., extensive grain growth must be avoided to maintain a fiber morphology within the composite. JES			
20. DISTRIBUTION / AVAILABILITY OF ABSTRACT <input checked="" type="checkbox"/> UNCLASSIFIED / UNLIMITED <input type="checkbox"/> SAME AS RPT. <input type="checkbox"/> DTIC USERS		21. ABSTRACT SECURITY CLASSIFICATION Unclassified	
22a. NAME OF RESPONSIBLE INDIVIDUAL Dr. Alan H. Rosenfeld		22b. TELEPHONE (Include Area Code) (202) 767-4933	
Schuler		22c. OFFICE SYMBOL AFOSR/NE	

19. The break-up of a dense, polycrystalline thin film into isolated, individual grains is described. This break-up is shown to result from grain growth. Two mechanisms are observed to uncover the substrate: a) very small grains disappear to expose the substrate and b) large amplitude perturbations at triple points grow as grain surfaces become spherical. Calculations show that the free energy of the system continuously decreases during this uncovering process when the grain size to film thickness ratio is greater than a critical value. Calculations and experimental observations show that the film will continue to cover the substrate if the critical size to thickness ratio is not exceeded. These results are important when thin films are used either to coat fibers for composite materials or for electronic devices, i.e., grain growth must be controlled.

The science and technology for eliminating heterogeneities from powders using the colloidal approach, consolidating colloidally prepared powders to form engineering shapes, densifying these shapes and methods of controlling microstructure are reviewed with the goal of increasing mechanical reliability through processing reliability. Research directions, required to implement these concepts, are summarized.

Accession For		
NTIS	CRA&I	<input checked="" type="checkbox"/>
DTIC	TAB	<input type="checkbox"/>
Research and		<input type="checkbox"/>
Development		
By		
Distribution		
Availability Codes		
Dist	Special	
A-1		



Interim Report

15 June, 1987 through 14 June, 1988

Grant: AFOSR-87-0291

Partitioning Reactions to Control and Develop Unique Microstructures

Technical Reports:

- 1 TEM Studies on Phases and Phase Stabilities of Zirconia Ceramics, M. Rühle, L.T. Ma, W. Wunderlich, and A.G. Evans
- 2 Instability of Polycrystalline Thin Films: Experiment and Theory, K.T. Miller, F.F. Lange, and D.B. Marshall
- 3 Morphological Stability of Polycrystalline Fibers, K.T. Miller and F.F. Lange
- 4 Powder Processing Science and Technology for Increased Reliability, F. F. Lange

Submitted to

Department of the Air Force
Air Force Office of Scientific Research
Electronic and Material Sciences
Bolling Air Force Base, DC 20332-6448

Submitted by

Materials Department
College of Engineering
University of California, Santa Barbara
Santa Barbara, CA 93106

Co-Principal Investigators: F. F. Lange and M. Rühle

Summary of Technical Reports

The research performed under Grant AFOSR-87-0291 for the period 15 June, 1987 to 14 June 1988 is detailed in the attached Technical Reports. The following are brief summaries of these reports.

Technical Report No. 1

TEM Studies on Phases and Phase Stabilities of Zirconia Ceramics, by M. Rühle, L.T. Ma, W. Wunderlich, and A.G. Evans

TEM studies for different ZrO_2 ceramics are reported. Observations are described to characterize the atomistic defects present in Mg-PSZ. TEM is applied to study phase stability and transformation in Y-TZP. The nucleation of stable $m-ZrO_2$ at stress singularities associated with grain boundaries was studied in situ and related to strains and strain distributions determined by high resolution electron microscopy.

Published: Electron Structure and Phase Stability in Advanced Ceramics, Physica B 150, 86-98 (1988)

Technical Report No. 2

Instability of Polycrystalline Thin Films: Experiment and Theory, by K.T. Miller, F.F. Lange, and D.B. Marshall

The break-up of a dense, polycrystalline thin film into isolated, individual grains is described. This break-up is shown to result from grain growth. Two mechanisms are observed to uncover the substrate: a) very small grains disappear to expose the substrate and b) large amplitude perturbations at triple points grow as grain surfaces become spherical. Calculations show that the free energy of the system continuously decreases during this uncovering process when the grain size to film thickness ratio is greater than a critical value. Calculations and experimental observations show that the film will continue to cover the substrate if the critical size to thickness ratio is not exceeded. These results are important when thin films are used either to coat fibers for composite materials or for electronic devices, i.e., grain growth must be controlled.

In Press: Better Ceramics Through Chemistry III, Materials Research Soc., Ed. by D.E. Clark, C.J. Brinker, and D.R. Ulrich, Pub. of the Spring MRS Meeting, 1988 (in press).

Technical Report No. 3

Morphological Stability of Polycrystalline Fibers, by K.T. Miller and F.F. Lange

The effect of grain growth on the morphological stability of polycrystalline fibers, constrained by a matrix, was determined. Analogous to thin films, grain growth was observed to cause the fiber to break-up into individual grains when the grain size to fiber diameter ratio exceeded a critical value. Calculations show that the free energy of the system continuously decreases as this break-up occurs. These results are important when polycrystalline fibers are intended to reinforce a matrix to produce a stronger composite material, viz., extensive grain growth must be avoided to maintain a fiber morphology within the composite.

Sent to: Acta Met.

Technical Report No. 4

Powder Processing Science and Technology for Increased Reliability, by F. F. Lange

The science and technology for eliminating heterogeneities from powders using the colloidal approach, consolidating colloidally prepared powders to form engineering shapes, densifying these shapes and methods of controlling microstructure are reviewed with the goal of increasing mechanical reliability through processing reliability. Research directions, required to implement these concepts, are summarized.

Sent to: J. Am. Ceram. Soc. (Sosman Memorial Lecture, 1987)

Technical Report No. 1

**TEM Studies on Phases and Phase
Stabilities of Zirconia Ceramics**

by

M. Rühle*, L.T. Ma, W. Wunderlich**, and A.G. Evans***

***Materials Department
College of Engineering
University of California, Santa Barbara
Santa Barbara, CA 93106**

and

****Max-Planck-Institut für Metallforschung
Institut für Werkstoffwissenschaften
Stuttgart, FR Germany**

Grant: AFOSR-87-0291

**Department of the Air Force
Air Force Office of Scientific Research
Electronic and Material Sciences
Bolling Air Force Base, DC 20332-6448**

TEM STUDIES ON PHASES AND PHASE STABILITIES OF ZIRCONIA CERAMICS

M. RÜHLE, L.T. MA*, W. WUNDERLICH** and A.G. EVANS

Materials Department, University of California, Santa Barbara, CA 93106, USA

Transmission electron microscopy (TEM) is a powerful tool to study defects and structures of materials. A comparison between quantitative evaluation of micrographs and diffraction patterns with results of contrast simulations allows a quantitative determination of many parameters. TEM is applied to study phase stability and phase transformations in ZrO_2 . Number densities of point defects can be evaluated for cubic zirconia, the nucleation of stable m - ZrO_2 at stress singularities of grain boundaries can be studied *in situ*. A quantitative evaluation of displacement fields in m - ZrO_2 which exist close to terminating twins can be measured and stress concentrations can be evaluated. The information is useful for a better understanding of phase stability in ZrO_2 .

1. Introduction

Transmission electron microscopy (TEM) studies allow the characterization of defects in materials as well as their undisturbed structure [1, 2]. Microstructural studies can also be used to investigate different stable and metastable configurations of ceramics which may undergo phase transformations. Additionally, *in situ* experiments allow the observation of the nucleation process of new phases.

In this paper, TEM studies for different ZrO_2 ceramics are reported. In section 2, observations will be described which allow a characterization of atomistic defects present in a stable configuration. Then, *in situ* observations of the martensitic tetragonal (t) to monoclinic (m) transformation in ZrO_2 are described and conditions are formulated for which a reversible transformation occurs within the electron microscope. Finally, by means of high resolution electron microscopy (HREM) studies, strains and strain distributions in ZrO_2 ceramics are evaluated.

2. Studies of point defect agglomerates in partially stabilized zirconia

In partially stabilized zirconia (PSZ), tetragonal t - ZrO_2 precipitates exist in a cubic (c) matrix [3]. The t - ZrO_2 precipitates may transform to a stable monoclinic (m) polymorph in front of the crack tip. The transformation leads to an increase in the material's toughness.

The shape of t - ZrO_2 precipitates depends on the relative change of the lattice parameters between the cubic and the tetragonal polymorph and can be predicted by a phenomenological theory developed by Khachaturyan [4, 5]. For Mg-PSZ lens-shaped precipitates develop. The shape can be approximated by an oblate rotation ellipsoid. MgO, dissolved in the cubic matrix, stabilizes the fluorite structure. Charge neutrality of these strongly ionic oxides, which is necessary on formation of solid solutions with these aliovalent solutes, requires a high density of vacancies on the oxygen sublattice, actually up to 22%. Lattice relaxation adjacent to oxygen vacancies leads to a shift of both cation and anion atomic positions which has been studied by X-ray and neutron diffraction (Morinaga et al. [6]). The t - ZrO_2 precipitates contain a much lower solute concentration; the crystal structure is essentially a tetragonally distorted version of fluorite.

* Presently at: Shanghai Institute of Ceramics, Shanghai, People's Republic of China.

** Max-Planck-Institut für Metallforschung, Institut für Werkstoffwissenschaften, Stuttgart, Fed. Rep. Germany.



Fig. 1. (a) Mg-PSZ aged to an optimum. "Typical" micrograph. The contrast of the *t* precipitates is bright compared to the *c* matrix. (b) Selected area diffraction (SAD) of fig. 1a.



Fig. 2. (a) Mg-PSZ, orientation $o \sim (001)$, thickness $4.25\xi_c$, $g = (200)$, dynamical images. (b) SAD of fig. 2a.

It was recognized [7] that TEM micrographs reveal a lower intensity of the ZrO_2 matrix compared to the *t*- ZrO_2 precipitates, independent of detailed imaging conditions. An example is shown in fig. 1, with fig. 1a showing a typically kinematical micrograph of 8.1 mol% Mg-PSZ and fig. 1b showing the corresponding diffraction pattern.

Fig. 2a displays an area with the same thickness of the foil as in fig. 1a imaged dynamically with a (200) matrix reflexion. Contrast experiments revealed that under dynamical imaging conditions only those precipitates show a characteristic strain contrast for which $(c_i \cdot g) \geq 0.3$ with c_i being the lattice vector parallel to $[001]_i$ of the precipitate. Fig. 2b represents the diffraction pattern of fig. 2a. It was not possible to excite two beam diffraction conditions as this is usually possible for a perfect TEM foil. High order diffraction vectors were always strongly excited for $E = 1$ (for the definition of E see Häussermann et al. [8]) and no Kikuchi lines [1] could be observed. Significant diffuse scattering was also present on all diffraction patterns. Scattering is caused by short range ordering processes in the

anion-deficient fluorite-related oxides [6]. The intensity and the intensity distribution of the diffuse scattering depend on the foil thickness and sensitively on the foil orientation. It is very difficult to evaluate diffuse electron scattering since dynamical effects are important for nearly all diffraction conditions and the dynamical theory of the multibeam situation is usually too complicated to be treated accurately.

With increasing excitation error ($E > 1$), the strain contrast disappears and, for $E \geq 2$, the characteristic contrast of bright precipitates is observed (fig. 1a). The latter contrast is more pronounced for unspecific kinematical diffraction conditions.

An interpretation of the contrast observed for different diffracting conditions is difficult as several scattering processes contribute to the image formation. Contrast arises from the following factors:

(i) *Structure factor contrast.* The precipitate and the matrix possess different structure factors due to their different crystal structures, resulting in different extinction lengths, even when the excitation errors are similar.

(ii) *Different excitation condition E.* The lattice parameters of *t*-ZrO₂ and *c*-ZrO₂ are different, resulting in different excitation conditions in precipitate and matrix.

(iii) *Strain contrast.* In Mg-PSZ, the *c/a* ratio of *t*-ZrO₂ results in a ~2% (homogeneous) compressive strain along [001]_t within the precipitate. The strain is further modified by the thermal expansion mismatch of *t*- and *c*-ZrO₂ along (100)_t. The net result is that the precipitate acts as a center of dilatation and strains the surrounding matrix. The strain distribution within the precipitate is only homogeneous if the precipitates possess the shape of an ideal oblate ellipsoid [9].

(iv) *Scattering from defects.* The composition of the *c*-ZrO₂ matrix in equilibrium with *t*-ZrO₂ precipitates at 1400°C can be determined from the equilibrium phase diagram (Grain [10]), and is Mg_{0.14}Zr_{0.86}O_{1.86}V_{0.14}^o, where V^o represents oxygen vacancies. Short range ordering of these defects results in elastic diffuse scattering, which can readily be seen on the diffraction patterns.

(v) *Strain around point defect clusters.* The oxygen vacancies are present in a very high concentration in the *c*-ZrO₂ matrix, and it is very likely that they will interact coulombically with the aliovalent cations to form a high density of defect clusters, which, due to lattice relaxation, are surrounded by a significant strain field. These strain fields can in principle be estimated by thermal diffuse scattering during X-ray examination, although individual defects are, of course, not able to be observed.

Wilkins and Rapps [11] have developed a statistical theory for understanding diffraction patterns of such highly defective crystals, which considers scattering by a high density of defects. With increasing defect density, the intensities of the low-order diffraction spots in the diffraction pattern decrease. Quantitative contrast evaluation of a series of micrographs taken under dynamical conditions with a variety of *g* showed that contrast according to factors (i) and (ii) can be neglected compared to factors (iii), (iv), and (v). It could also be shown that the strain contrast (factor (iii)) leads to much higher intensities than the contrast due to the presence of the

small defects in the cubic matrix (iv and v).

Consistent with these conclusions, we have also found that for dynamical diffraction conditions with *E* = 1, only those precipitates show strong strain contrast for which (*c_t · g*) > 0.3. These observations indicate that strain contrast outweighs all other contrast formation mechanisms. Furthermore, for specific kinematical diffraction conditions with *E* > 2 (fig. 2), only those variants show appreciable contrast for which (*c_t · g*) > 0.3. Those variants are bright with respect to the background intensity of the cubic matrix, the other variants, again, are out of contrast [7]. Strong diffuse scattering can always be observed on the diffraction pattern. These observations suggest that vacancies on the oxygen sublattice (or oxygen vacancy clusters) cause sufficient scattering to reduce the intensity of the cubic matrix. The diffraction pattern shows, however, that the intensity is always distributed over the row of systematic reflections. This implies that the high density of the vacancy-defect agglomerates acts as a scattering center distributing the intensity of the incoming beam over many reflections.

The statistical theory by Wilkins and Rapps [11] can be applied to these experimental observations. Wilkins and Rapps assumed that those defects which lie within a critical distance *r_c* from a column passing through a foil of thickness *t*, modify the diffraction conditions. Results of calculations are represented in fig. 3. It is the number of defects per column, *m*, which mainly affects scattering into higher order reflections:

$$m = \delta t \pi r_c^2,$$

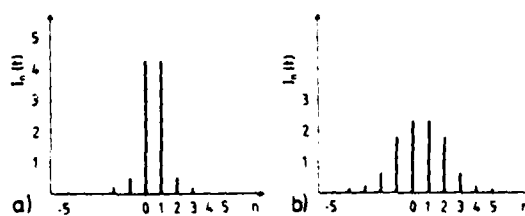


Fig. 3. The diffraction intensities $I_n(t)$ as a function of n (n = order of reflection) for the defect model by Wilkins and Rapps [11]. (a) Perfect lattice, (b) defect lattice ($c \sim 10^{22} \text{ cm}^{-3}$).

where δ is the number density of defects. The result is valid for kinematical conditions. A comparison of the observed diffraction (fig. 2b) with the prediction (see fig. 3b) of the theory shows good agreement for $m \sim 40$. For a further evaluation of these images, assumptions for δ and r_c have to be made.

For a foil thickness of $t = 872 \text{ \AA}$ (fig. 2a) and $r_c = 10 \text{ \AA}$, δ results in $0.183 \times 10^{21} \text{ cm}^{-3}$ which approximately corresponds to the density of point defects present in the cubic matrix of Mg-PSZ. The comparison suggests that the background contrast of the cubic matrix is predominantly produced by the presence of single point defects.

High resolution studies allow the determination of the atomistic structure of the interface between the cubic matrix and the tetragonal precipitate. However, for lattice parameters equal to the resolution limit of the TEM, there is no direct connection between the arrangement of atoms in the object and the images observed. Lens aberrations influence the image strongly. By iteration, beginning with assumed atomic positions, followed by computation of the image contrast (where the influence of lens operations of electron microscopes on the image is included) and comparison with observed images, an approach to the true (or most likely) structure can be made [12]. HREM studies determine the position of atom columns at and near the interface. These studies, however, have not yet been completed for the coherent interface between the cubic matrix and the tetragonal zirconia. Detailed computations are still required.

3. In situ transmission electron microscopy observations

It is well-founded that the kinetics of a martensitic (t) \rightarrow (m) transformation in ZrO_2 is nucleation controlled. Ma et al. [13] and Heuer and Rühle [14] observed *in situ* the nucleation process in a TEM and discussed different mechanisms leading to the nucleation of the martensite phase. In accordance with recent theoretical studies [15], it could be shown that nucleation

via localized soft mode mechanism under strain concentration is always possible. Nucleation is always stress-assisted, even if the transformation occurs spontaneously.

Experimental *in situ* TEM studies concentrated on Y_2O_3 containing *t*- ZrO_2 polycrystals (Y-TZP). The microstructure of different materials (containing 3–5 wt% Y_2O_3) was described [16]. Usually, *t*- ZrO_2 grains are $< 1 \mu\text{m}$ in diameter. In some samples, *c*- ZrO_2 grains are present if the ceramic was sintered in the two-phase (t + c) field of the phase diagram. Grain boundaries are usually covered with a thin thoroughly amorphous grain boundary phase. No grain boundary dislocations can therefore be present. Such boundaries are, however, sites of localized residual stresses arising from thermal expansion anisotropy of *t*- ZrO_2 [17]. Schubert determined for a 4.5 wt% Y-TZP $\alpha_a = 7.1 \times 10^{-6}/\text{K}$ and $\alpha_c = 11.4 \times 10^{-6}/\text{K}$.

Y_2O_3 is a very effective solute for stabilizing the c and t forms of ZrO_2 , and reduces the driving forces for t \rightarrow m transformation. Y_2O_3 also increases the difficulty of nucleation. This is manifested by a non-continuous transformation zone adjacent to propagating cracks in a TEM foil.

However, the stability of *t*- ZrO_2 in Y-TZP can be used to study the nucleation of the martensitic transformation. The *t*- ZrO_2 is stable in an unstressed bulk or thin specimen if the grain size of Y-TZP lies below a critical value: thermal mismatch stresses present at grain boundaries are insufficient to create a nucleus [14]. If, however, additional stresses are applied and result in a critical stress required for the nucleation, the transformation starts. These additional stresses can be created by the electron beam of a TEM. This is shown schematically in fig. 4. Focusing of the beam onto the specimen leads to a local heat generation by inelastic scattering of the electrons. The associated temperature and temperature profile may be estimated if certain simplifying boundary conditions are presumed [18]. If, however, the specimen thickness varies over the size of the beam (fig. 4a), it is very difficult to evaluate temperature distributions. Experimental studies reveal that the very thin

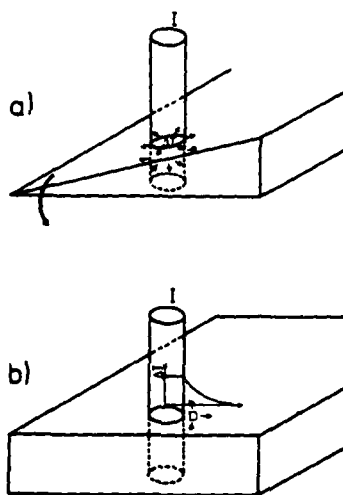


Fig. 4. Interaction of a high intensity electron beam with a TEM specimen. (a) Inhomogeneous thickness, the specimen bends during irradiation; (b) homogeneous thickness, stresses develop in the surrounding of the beam.

part of the specimen bends (as indicated in fig. 4a) and bend contours move during these observations. Sometimes, additional stresses by bending are sufficient to nucleate a m - ZrO_2 lath in the very thin part of the grain, always starting at a grain boundary.

No bend contours are observed when a film with homogeneous thicknesses is irradiated with electrons. For this situation, temperature and temperature-induced stresses can be calculated [18, 19]. Here, the specimen is regarded as a thin disc of radius R and thickness t and it is assumed that the beam is focussed in the center over a radius r_0 . Then, heat is generated constantly throughout the cross section (over region r_0).

The heat generated per electron is

$$Q = 7.8 \times 10^4 (Z\rho t/AE) \ln(E/J), \quad (1)$$

where ρ is the density, Z the number of electrons per atom, A the atomic number, J the mean ionisation potential and E the energy intensity of the incoming beam. For ZrO_2 eq. (1) gives

$$Q \sim 1.1\rho t \text{ eV}/\mu\text{g cm}^2. \quad (2)$$

By assuming that the heat results only in radial conduction, a steady-state temperature distribution may be readily computed as

$$T = T_0 + \lambda \ln(R/r_0) \quad (r > r_0), \quad (3a)$$

where T_0 is the imposed temperature at the disc perimeter and

$$\lambda \sim (jr_0^2/2e\kappa)(\delta Q/t), \quad (3b)$$

with j being the electron beam intensity, and κ the thermal conductivity [18]. By combining eqs. (2) and (3b) and inserting the appropriate properties for ZrO_2 , the temperature distribution becomes (in SI units)

$$T - T_0 = jr_0^2 \ln(R/r).$$

For the present experiments: $r_0 \sim 0.5 \mu\text{m}$ and j varies between 10^4 and $5 \times 10^5 \text{ A m}^{-2}$, λ is in the range $100 \text{ K} < \lambda < 500 \text{ K}$.

It is frequently assumed that thermal stress in thin foils induces buckling. However, micrographs of a plane foil do not reveal bend contours that would develop upon buckling. Indeed, buckling is highly constrained in edge supported discs and would normally not be anticipated. Consequently, stress analysis for an unbuckled disc is deemed appropriate and will be emphasized.

For a thin disc subject to a radial temperature distribution $T(r)$, the thermal stresses can be evaluated [19]. It can be shown that the central hot spot is under hydrostatic compression, while the remainder of the disc is under uniform hydrostatic tension; furthermore, the in-plane shear stress is zero at the center, reaches a maximum immediately after leaving the hot zone and then diminishes rapidly beyond the focal spot. The maximum shear strain results in

$$\tau^{\text{max}} = \frac{1}{2} \alpha Y (T_0 - T),$$

where α is the thermal expansion coefficient of ZrO_2 , Y the Young's modulus (of the material in the hot spot) and $T_0 - T$ the change of temperature. Maximum shear stresses of

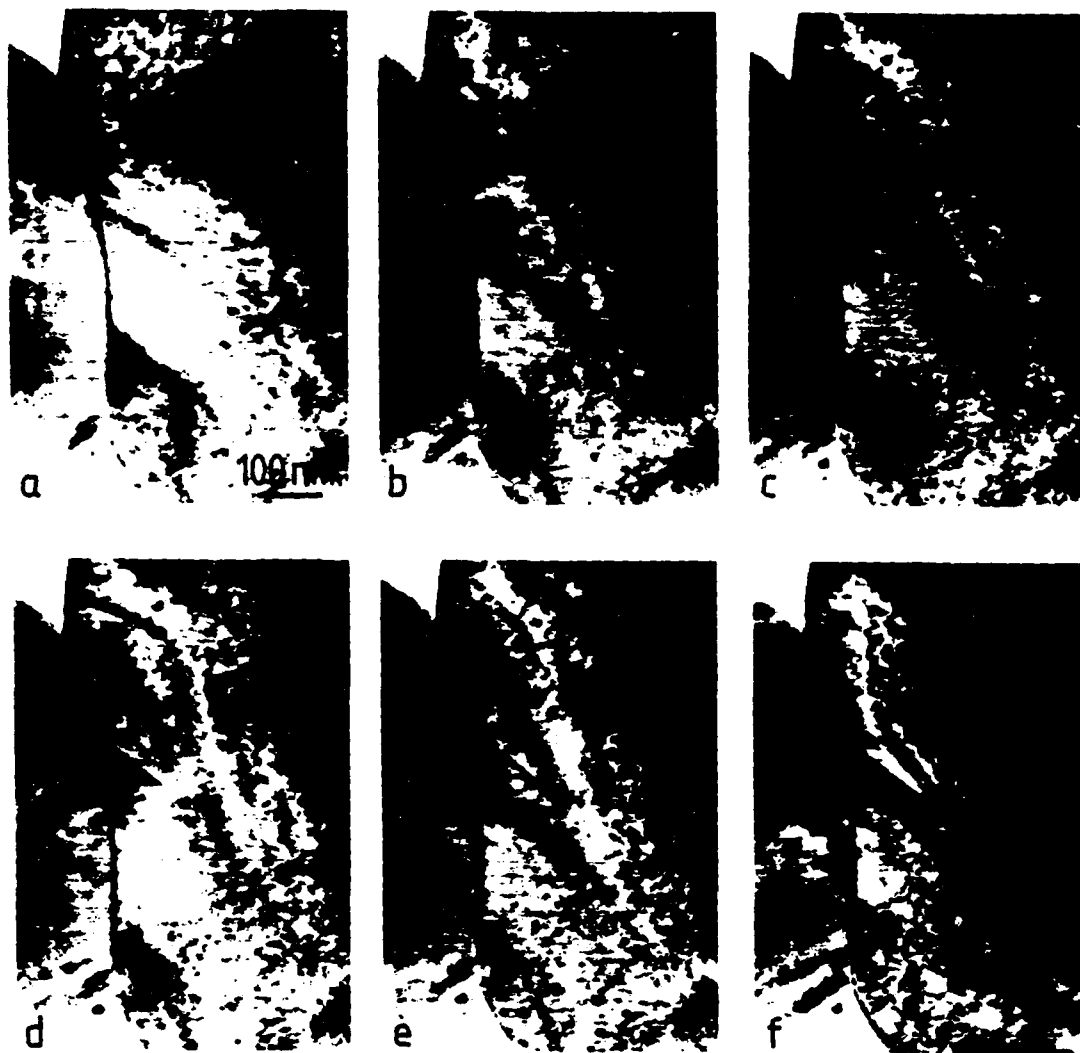


Fig. 5. Nucleation in Y-TZP: at the beginning of the experiment (a) no defects or localized strain contours are visible on the grain boundary but develop during irradiation (b) as shown by the arrow, disappear (c) and eventually an untwinned martensite lath (an m - ZrO_2 plate) develops (d) and grows into the grain (e + f).

$$\tau^{\max} = 2 \times 10^{-3} Y$$

can be reached.

Experimental observations verify the model. It was possible to nucleate the transformation at grain boundaries and propagate a martensite lath across the grain when the region of the grain

boundaries lay at the outer perimeter of the hot region. The lath is either parallel to the tangent of the hot spot or forms a small angle.

Figs. 5, 6, and 8 show typical examples. Fig. 5 shows a typical essentially featureless high angle grain boundary at the beginning of the experiment. After a short interval of electron irradiation



Fig. 6. Partially transformed t -ZrO₂ grain in Y-TZP. The m -ZrO₂ lath formed at the grain boundary. No nucleation occurred at dislocations.

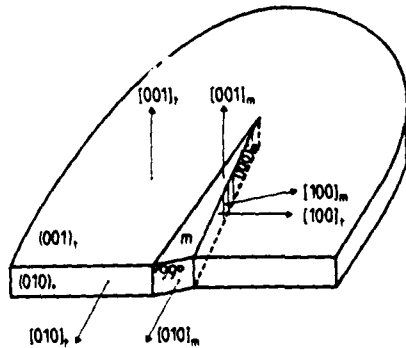


Fig. 7. Orientation relationship for region near the lath in fig. 6.

tion, strain contours develop at a particular site along the grain boundary (the arrowed features in fig. 5b perpendicular to the tangent of the hot spot). These strain contours oscillate during the experiment and sometimes die away (fig. 5c). On occasion, however, a small lath of martensite (m -ZrO₂) will grow out of these oscillatory contours and will begin to grow across the grain, as is shown in fig. 5d and 5e. It is significant that the strains close to the few isolated dislocations, small-angle boundaries, and stacking faults present in such ceramics do not usually act as potent embryos, as most grains containing such defects

and being transformed under electron irradiation also form nuclei at grain facets and boundaries. For example, fig. 6 is a bright field/micrograph showing several martensite laths (the arrowed features), one of which has completely grown across the grain and has nucleated at an otherwise featureless site at a grain boundary. Note that these nucleation events occurred in a grain containing both a small angle grain boundary and a stacking fault.

An analysis of the crystallography shows that in these two examples (figs. 5 and 6) a shear component occurs out of the foil, as is shown in fig. 7.

Fig. 8 shows a third example where the martensite lath is completely included in the foil. If, for this situation, the partially transformed grain is moved into the center of the hot spot then the transformation is reversed: the temperature of one part of the specimen which includes the m -ZrO₂ lath is raised and compressive stresses are applied so that the transformation can be reversed [20]. The grain could be completely transformed to the t -ZrO₂ phase. The reverse transformation could only be observed if (i) no relaxation outside the foil occurred and (ii) high-temperature increases could be obtained.

The example of the $t \rightarrow m$ transformation supports the hypotheses that the nucleation of the monoclinic phase in Y-TZP is stress-assisted and starts at grain boundaries in regions of the highest shear stress intensity.

For the reverse transformation in figs. 8a-d, both the local temperature and the local stress state are unknown, so it is not possible to determine their independent contributions to driving back the transformation. The temperatures reached by focusing an electron beam on ZrO₂ samples can be quite high (up to 700°C). It is possible that the temperature of the grain increases near or to the point where the monoclinic phase would no longer be stable. Because Y₂O₃ stabilizes the tetragonal phase, the equilibrium temperature for the reverse transformation ($m \rightarrow t$) should be lower than that for pure ZrO₂ (1150°C). Exact M_s and A_s temperatures are currently unknown as a function of Y₂O₃ content. Any increase in the temperature of the

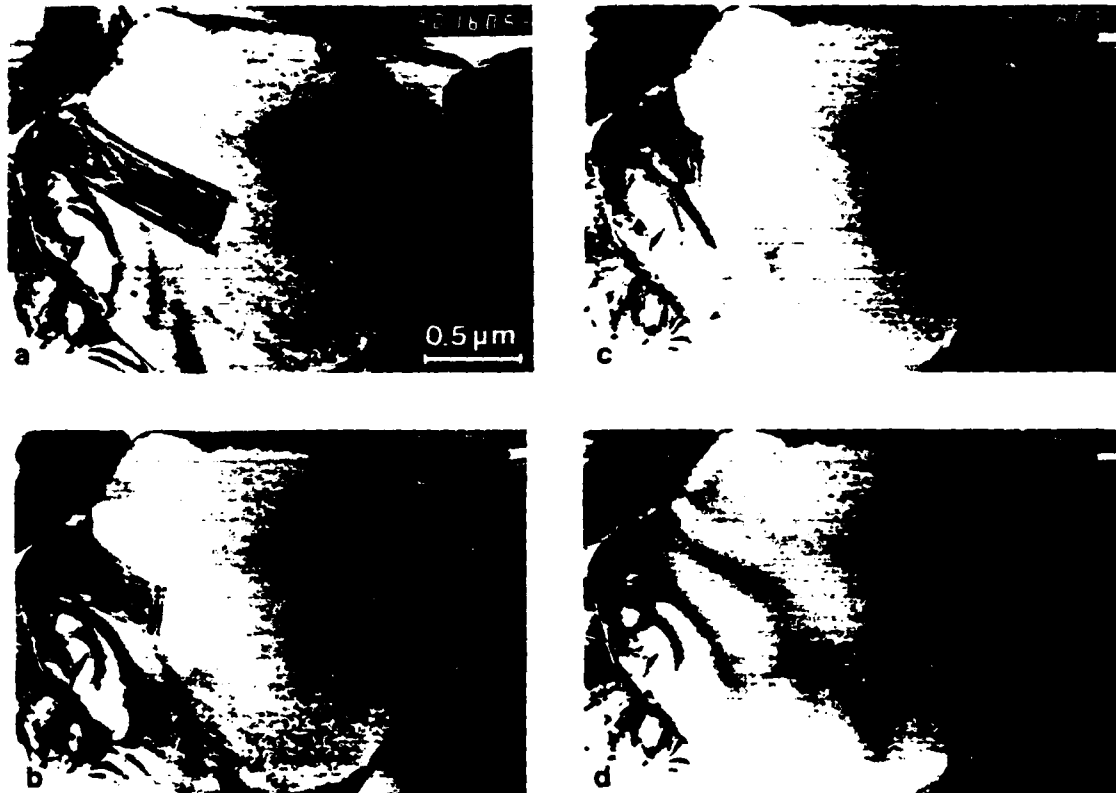


Fig. 8. Reverse $m \rightarrow t$ transformation. The monoclinic lath in the tetragonal grain diminished with increased beam intensity. Sequential micrographs are shown in (a)-(d). (By courtesy of M. McCartney.)

sample would diminish the driving force needed to cause the reverse transformation.

A second contribution supporting the reverse transformation comes from stresses generated due to the volume expansion of the monoclinic needle in the tetragonal matrix. In partially transformed grains, these stresses were not relieved or reduced by twinning. Additionally, compression stresses from the surrounding grains could also assist the reverse transformation due to the thermal expansion of the hot spot. We suppose that the stress state must have aided the reverse transformation, and that temperature was not the only influence because fully transformed and twinned regions of the sample (where the stresses due to the transformation had been accommodated) would not revert to the tetra-

gonal phase despite being subjected to the same high beam intensity as the regions which exhibited the reverse transformation (fig. 8). Additionally, the monoclinic needle in fig. 8 appeared to be constrained in three dimensions in the foil, generating considerable stresses for the back transformation. This could be contrasted by figs. 5, 6, where the needles penetrate the upper and lower surfaces of the foil, and allow an out-of-the-film relaxation.

Transformation could occur slowly in these $Y_2O_3-ZrO_2$ samples. Bailey [20] found that for pure single crystal ZrO_2 the transformation in both directions was very rapid and that it was not possible to record intermediate states. In these experiments with Y-TZP, however, it was possible to both slowly grow and decrease the mono-

clinic areas by careful adjustment of the beam intensity. This is reminiscent of thermoelastic martensite, in which the growth of martensitic plates is halted when the free energy to drive the reaction is counterbalanced by strain energy produced in the matrix phase [21]. Even if the sample is at a temperature where the monoclinic phase should be chemically stable, stresses in the system can counteract this tendency and cause the tetragonal phase to reappear.

Defects such as oxygen vacancies generated by the presence of substitutional Y^{3+} could also play a role in decreasing the chemical driving force and also hindering the progression of the interface. There may be a dislocation present at the leading edge of the monoclinic lath in fig. 8. A moving dislocation at the transforming interface would be slowed by defects or defect clusters, these impeding both the waxing and waning of the monoclinic phase.

4. High resolution TEM studies of m -ZrO₂

The $t \rightarrow m$ phase transformation involves a shape change of the unit cell. The introduction of twins reduces the strain energy of the total system. Therefore, all martensitic phase transformations result in a highly twinned martensite structure [4]. The twin structure and internal strains in m -ZrO₂ were studied by TEM, particularly by HREM. For these studies, pure skull-melted m -ZrO₂ was used. The t -ZrO₂ transforms to m -ZrO₂ at the martensite temperature of $M_s \sim 900^\circ\text{C}$. Thick lamellae (fig. 9, 100 to 300 nm thick) are observed.

Frequently, triangularly shaped regions can be observed at the end of such twins (fig. 9). The triangularly shaped regions contain also twins and additional smaller triangles of orthorhombic ZrO₂ [22] which may be (formed) during TEM specimen preparation. An example of a twinned triangular region is shown in fig. 10a. The crystallographic orientation relationships are represented in fig. 10b.

The two-dimensional defects in fig. 10a are also (100) twins. The measured width of the lamella is 0.25 of its length. Either lattice bend-

ing (due to elastic strains) or microcracking occurs in the regions of intersection of the small twin with the surrounding m -ZrO₂ plates. Small triangles are present within the regions of compression. The latter observations may correspond to "domains of closure" [23]. Strained regions close to the terminating twins can be mapped by HREM for platelets of m -ZrO₂ with different thicknesses. The difference between the unstrained and the strained lattice results in a displacement field. The corresponding strains can be obtained by taking the appropriate derivatives. Maximum strains are expected for platelets with large thicknesses. A micrograph taken with higher magnification and resolution is shown in fig. 11a while fig. 11b represents a drawing of the crystallographic orientation relationships. Fig. 11a shows a micrograph of a corner of a twin boundary at a higher magnification. Bending of the lattice planes (resolved by HREM) can readily be observed in fig. 11a if the monoclinic matrix is adjacent to the twin planes. In this example, the stress is not large enough to form a crack. The displacement field at the interface between the twin lamellae and the

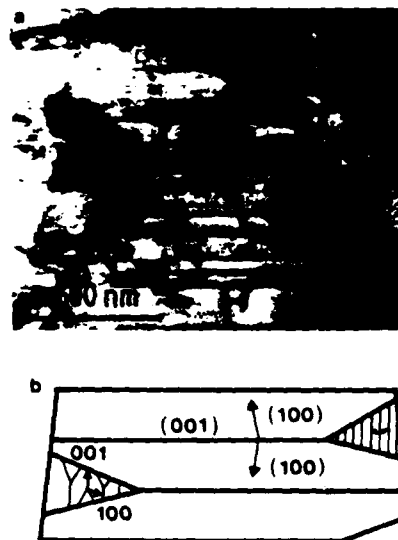


Fig. 9. (a) Skull-melt m -ZrO₂ TEM micrograph of low magnification. (b) Schematic drawing of twinned structures. The interface between a large twin and a triangle is studied.

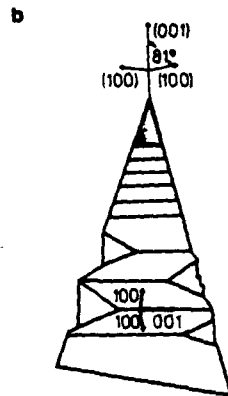


Fig. 10. (a) Pure monoclinic zirconia contains many twin structures. At some places, triangles are observed which are twinned on a finer scale. Microcracking can be observed where the twins strain the interface. (b) Crystallographic orientation of the twin lamellae. The coarse-dotted triangles probably have orthorhombic symmetry.

monoclinic matrix accommodates to the 6% misfit between the patterns. Large bending can be observed caused by the strong atomic bonding at a coherent or partially coherent interface.

A coordinate system (x, y) is introduced as shown in fig. 11b. The displacement fields $u(x, y)$ and $v(x, y)$ can be measured in fig. 11a. A direct evaluation from HREM images is possible and no change of the HREM image is expected due to lens aberrations of the TEM, since the lattice parameters of $m\text{-ZrO}_2$ are large ($\sim 5 \text{ \AA}$) compared to the point-to-point resolu-

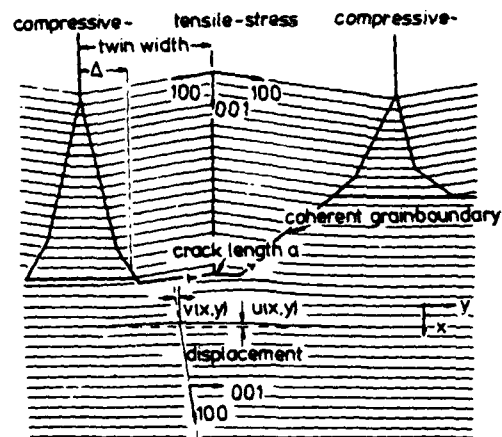
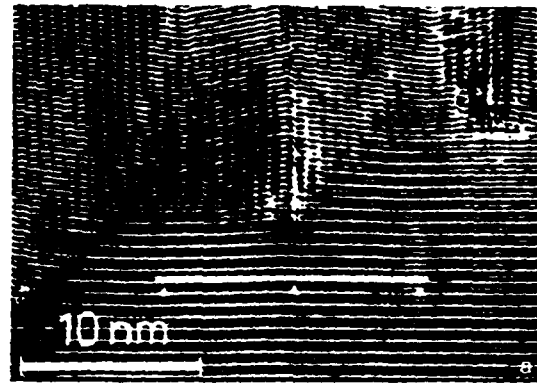


Fig. 11. (a) Micrograph of a corner of a twin boundary at a higher magnification. The lattice planes are bent due to the stress caused by the twin. In this example, the stress is not high enough to form a crack. (b) Characterization and experimental parameters on the tensile stress side of a twin boundary. The assumed stress field is shown above. The position of the coordinate system (x, y) is noted in (b).

tion of the used TEM (2.3 \AA). The displacement fields $u(x, y)$ and $v(x, y)$ were evaluated for various regions near a terminating twin and the results for $u(x, y)$ and for one twin configuration are depicted in fig. 12. Experimentally measured displacements are smoothed before derivatives are formed. The very thin foil used for HREM studies represents, in a very good approximation, a plane stress configuration. The strain components can be evaluated by

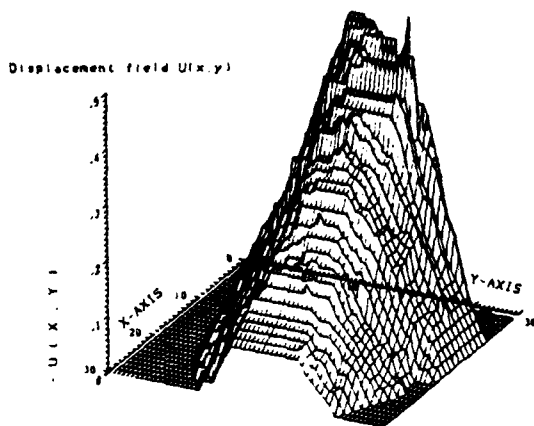


Fig. 12. Three-dimensional representation of the displacement field $u(x, y)$. The undisturbed mesh in the x - y plane corresponds to the m - ZrO_2 lattice. The units of $u(x, y)$ correspond to 0.1 nm.

$$\varepsilon_x = \frac{\partial u}{\partial x}, \quad \varepsilon_y = \frac{\partial v}{\partial y}, \quad \varepsilon_{xy} = \frac{1}{2} \left(\frac{\partial u}{\partial y} + \frac{\partial v}{\partial x} \right).$$

The experimentally evaluated components of the strain tensor are shown in figs. 13a-c. A comparison with the selected geometry shows that, as expected, the highest tensile strains ε_x are noticed close to the twin plane ($x = 0, y = 0$).

The results of the displacement field for $u(x, 0)$ for twin lamellae of 4 different lamellae thicknesses are shown in fig. 14. Differentiation in x -direction leads to the strain ε_x . Maximum tensile strain approaches $\varepsilon_x \sim 0.14$ and the maximum shear component ε_{xy} is also in the same order of magnitude. The results support the assumption that very high local stresses are required for debonding the interface.

The stresses can be evaluated under the assumption that m - ZrO_2 is an isotropic material:

$$\sigma_x = \frac{E}{1-\nu^2} [\varepsilon_x + \nu\varepsilon_y],$$

with $E = 200$ GPa and $\nu = 0.19$ one obtains

$$\sigma_x^{\max} = 29 \text{ GPa}.$$

The assumption of elastic isotropy is clearly inappropriate. Recent experiments by Chan et

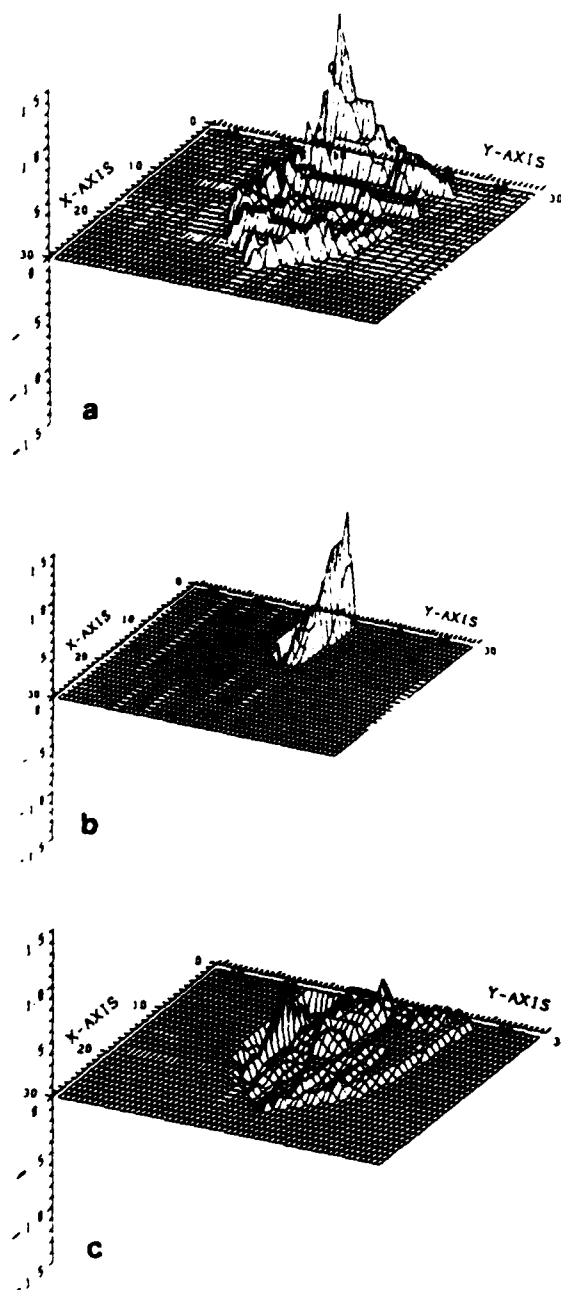


Fig. 13. Three-dimensional representation of the three strain components of the strain tensor for plane stress configuration. The strain fluctuations are partially caused by errors due to the noise on the TEM micrograph. (a) ε_x -component, (b) ε_y -component, (c) ε_{xy} -component.

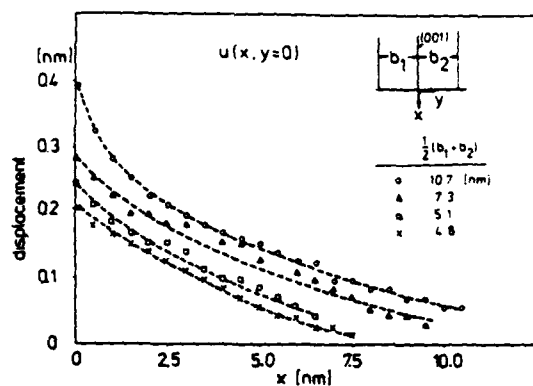


Fig. 14. The measured displacement field $u(x, 0)$ as a function of the distance from the interface. The symbols correspond to lamellae of different thicknesses.

al. [24] will result in the elastic constants of $m\text{-ZrO}_2$. If these constants are known, actual stresses existing in the twin-near regions can be evaluated and compared to model calculations by finite element techniques.

The observations demonstrate, however, that $m\text{-ZrO}_2$ bonds across twins can withstand large local strains. HREM studies allowed a quantitative determination of local strains. Rather large values of strains were observed. Microcracking requires breaking of ionic bonds. Dislocations or disclinations present near the mid-twin plane reduce the maximum internal stresses observed at interfaces.

The experimental results can be compared to a theoretical model evaluated by Fu et al. [25] who analysed the stress distribution at the ends of the twins for an $m\text{-ZrO}_2$ particle embedded in Al_2O_3 and composed of 2, 4 or 6 twins. Using linear elasticity, they found that for very small microcracks the stress intensity factor dropped below the critical stress intensity factor for crack growth which had been estimated from experimentally determined crack lengths. They thus concluded that spontaneous initiation of very small microcracks cannot be explained by using linear elasticity and they suggested that microcrack nucleation requires the presence of lattice defects (e.g. dislocations), or involves nonlinear bond displacement in response to the

very high stress concentrations. The experimental observations presented in this paper support the latter model (cf. fig. 11). With these results, data assuming the nonlinear theory have to be reevaluated.

5. Summary and conclusions

Transmission electron microscopy, analytical electron microscopy and high resolution electron microscopy can be used for studies of phase stability and phase transformations in ceramics. The techniques were applied to ZrO_2 . An analysis of images as well as diffraction patterns of $c\text{-ZrO}_2$ and $t\text{-ZrO}_2$ results in an understanding of the characteristic parameters of defects in these materials. The nucleation of a $t \rightarrow m$ transformation can be studied although not yet to the atomistic level. The nucleation can be triggered in metastable $t\text{-ZrO}_2$ by radial shear stresses existing close to a high intensity electron beam. Shear produced by the untwinned martensite lath opposes shear due to beam heating. An $m\text{-ZrO}_2$ lath within a $t\text{-ZrO}_2$ matrix can be retransformed to $t\text{-ZrO}_2$ if $m\text{-ZrO}_2$ is irradiated by a high intensity electron beam and heated to very high temperatures, due to the compressive stresses within this region. High resolution studies allow a quantitative evaluation of strain components existing near twins. The atomistic structure of twins can also be determined.

Acknowledgements

The authors acknowledge the experimental assistance of Mrs. D. Waidelich (Stuttgart). We also would like to thank Mrs. D. Jilg (Stuttgart) for the linguistic revision and the effective typing of the paper. The authors thank the Air Force Office of Scientific Research for financial support under contract No. AFOSR-87-0291.

References

- [1] P.B. Hirsch, A. Howie, R.B. Nicholson, D.W. Pashley and M.J. Whelan. *Electron Microscopy of Thin Crystals* (Krieger, Huntington, NY, 1977).

- [2] M. Rühle and M. Wilkens, in: *Physical Metallurgy*, vol. I, R.W. Cahn and P. Haasen, eds. (Elsevier, Amsterdam, 1983).
- [3] N. Claussen, M. Rühle and A.H. Heuer, eds., *Science and Technology of Zirconia II*, *Advances in Ceramics*, vol. 12 (The American Ceramic Society, Columbus, OH, 1984).
- [4] A.G. Khachaturyan, *Theory of Structural Transformation in Solids* (Wiley, New York, 1983).
- [5] V. Lanteri, T.E. Mitchell and A.H. Heuer, *J. Am. Ceram. Soc.* 69 (1986) 564.
- [6] M. Morinaga, J.B. Cohen and J. Faber Jr., *Acta Cryst.* A 35 (1979) 789; A36 (1980) 520.
- [7] A.H. Heuer, M. Rühle and D. Waidelich, *Inst. Phys. Conf. Ser.* 68 (1983) 389.
- [8] F. Häussermann, K.-H. Katerbau, M. Rühle and M. Wilkens, *J. Microscopy* 98 (1973) 135.
- [9] T. Mura, *Micromechanics of Defects* (Martinus Nijhoff, Leiden, 1976).
- [10] C.F. Grain, *J. Am. Ceram. Soc.* 50 (1967) 288.
- [11] M. Wilkens and R. Rapps, *Phys. Stat. Sol. (a)* 44 (1977) 173.
- [12] M.A. O'Keefe, in: *Electron Optical Systems*, J. Ohari, ed. (SEM, AMF O'Hara, 1981), p. 209.
- [13] L.T. Ma, M.L. Mecartney and M. Rühle, unpublished results.
- [14] A.H. Heuer and M. Rühle, *Acta Metall.* 33 (1985) 2101.
- [15] G.B. Olson and M. Cohen, *Ann. Rev. Mater. Sci.* 11 (1981) 1.
- [16] M. Rühle, N. Claussen and A.H. Heuer, in ref. [3], p. 352.
- [17] H. Schubert, *J. Am. Ceram. Soc.* 69 (1986) 270.
- [18] L. Reimer, *Transmission Electron Microscopy* (Springer, Berlin, Heidelberg, New York, Tokyo) 1984.
- [19] M. Rühle, L.T. Ma, M.L. Mecartney and A.G. Evans, unpublished results.
- [20] J.E. Bailey, *Proc. Roy. Soc. (London) A* 279 (1964) 395.
- [21] N.N. Thadhani and M.A. Meyers, *Progr. Mat. Sci.* 30 (1986).
- [22] S.-K. Chan, unpublished results.
- [23] E. Bischoff and M. Rühle, *J. Am. Ceram. Soc.* 66 (1983) 123.
- [24] S.-K. Chan, personal communication.
- [25] K. Fu, A.G. Evans and W.M. Kriven, *J. Am. Ceram. Soc.* 67 (1984) 626.

Technical Report No. 2

**Instability of Polycrystalline Thin
Films: Experiment and Theory**

by

K.T. Miller*, F.F. Lange*, and D.B. Marshall**

***Materials Department
College of Engineering
University of California, Santa Barbara
Santa Barbara, CA 93106**

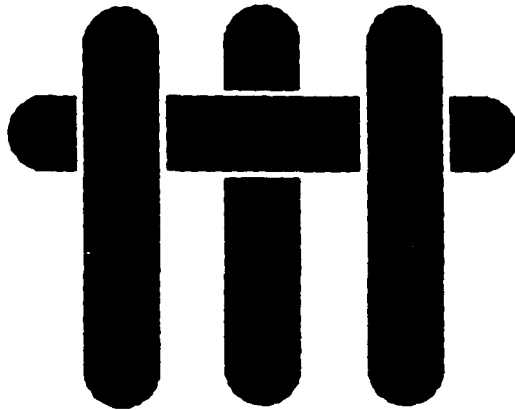
and

****Rockwell International Science Center
1049 Camino dos Rios
Thousand Oaks, CA 91360**

Grant: AFOSR-87-0291

**Department of the Air Force
Air Force Office of Scientific Research
Electronic and Material Sciences
Bolling Air Force Base, DC 20332-6448**

M A T E R I A L S



THE INSTABILITY OF POLYCRYSTALLINE THIN FILMS:
EXPERIMENT AND THEORY

by

K. T. Miller, F. F. Lange, and D. B. Marshall

Department of Materials
College of Engineering
University of California
Santa Barbara, CA 93106

April 5, 1988

THE INSTABILITY OF POLYCRYSTALLINE THIN FILMS: EXPERIMENT AND THEORY

K. T. MILLER,* F. F. LANGE,* and D. B. MARSHALL**

*Department of Materials, University of California, Santa Barbara, Santa Barbara, CA
93106

**Rockwell International Science Center, Thousand Oaks, CA 91360

ABSTRACT

Dense polycrystalline thin films of ZrO_2 (3 and 8 mol% Y_2O_3) were produced by the pyrolysis of zirconium acetate precursor films, which were deposited on single crystal Al_2O_3 substrates by spin-coating solutions of zirconium acetate. With grain growth, these films broke into islands of ZrO_2 grains. Thermodynamic calculations show that this break up lowers the free energy of the system. These calculations also predict the conditions needed for polycrystalline thin film stability.

1. INTRODUCTION

Liquid precursors (for example, solutions of alkoxides, acetates, and citrates) can be used to form ceramic thin films. In this process, the liquid precursor is deposited on a chemically compatible substrate by either spin-coating or dip-coating. An oxide thin film is then formed by the pyrolysis of the precursor film. To better understand this process, a program of study has been initiated, emphasizing the relations between processing and microstructural development during heat treatment required to convert the precursor into a dense ceramic thin film.

Water soluble zirconium acetate was the precursor used in this study. A water soluble yttrium salt was added to form ZrO_2 -rich compositions within the ZrO_2 - Y_2O_3 binary system. This system includes the transformation toughening tetragonal structure (3 mol% Y_2O_3) and a cubic structure (8 mol% Y_2O_3). These two compositions were chosen because grain growth is extremely sluggish for the tetragonal composition and very rapid for the cubic composition.¹ Single crystal wafers of Al_2O_3 , which is chemically compatible with ZrO_2 , were used as substrates.

Initial experiments showed that dense, polycrystalline thin films of ZrO_2 could be formed. When subjected to further heat treatment, the films would uncover the substrate by breaking up into an interconnected network of zirconia grains. Such behavior has been observed in a variety of systems. Srolovitz and Safran^{2,3} suggested that grain boundary grooving at triple grain junctions in polycrystalline films could create a pinhole-like defect which would grow to rupture the film. In the present study, we investigate the break up process by examining the microstructural evolution of relocatable areas on the film after

sequential heat treatments. In addition we have calculated the free energy of thin film configurations consistent with the grain growth phenomena observed to produce film break up. These calculations show that when the grain size to film thickness ratio is greater than a critical value, the grains will lower the free energy of the system by uncovering the substrate.

2. EXPERIMENTAL PROCEDURE

ZrO₂ (3 and 8 mol% Y₂O₃) thin films on single crystal Al₂O₃ (Adolph Meller Co., Providence, RI) were produced by the pyrolysis of films deposited by spin coating aqueous solutions of zirconium acetate and yttrium nitrate. The liquid films were produced by spinning for 30 seconds at 5000 rpm, which was sufficient time for the solution to dry to a glassy precursor film during spinning.

The films were pyrolyzed by heating to 1000 °C in air and cooling. These films were then subjected to a series of heat treatments. The heat treatment series consisted of heating to 1200 °C, 1300 °C, and 1400 °C, followed by immediate cooling. The films were then subjected to treatments at 1400 °C for different periods. After each heat treatment, the microstructure of the relocatable areas was examined with the scanning electron microscope. The films were coated with a thin carbon layer to prevent charging in the microscope. This layer would burn off during the subsequent heat treatment.

3. RESULTS

After the 1200 °C heat treatment, the films consisted of a low density network of crystallites with a size (~ 25 nm) near the resolution limit of the SEM. During the higher temperature heat treatments, the grain size increased rapidly and the films sintered, becoming nearly dense at 1300 °C and fully dense at 1400 °C. When the films were held at 1400 °C, both the 3 and 8 mol% Y₂O₃ films began to break up into islands. In each case, the break up is associated with grain growth. The break up mode, however, differs for these two different compositions. Figure 1 shows micrographs of the break up in the 3 mol% Y₂O₃ film. In this case, the smallest grains disappear (possibly through evaporation/condensation), leaving bare spots of exposed substrate. Figure 2 shows the breakup of the 8 mol% Y₂O₃ film. Here two breakup mechanisms were observed. In the first, which is similar to that observed in finer grained 3 mol% Y₂O₃ film, the smallest grains shrink, exposing the substrate at triple grain boundary junctions, and eventually disappear, exposing substrate. In the second, grain boundaries migrate, enveloping smaller grains. The larger grains formed by this migration then spheridize to expose the substrate.

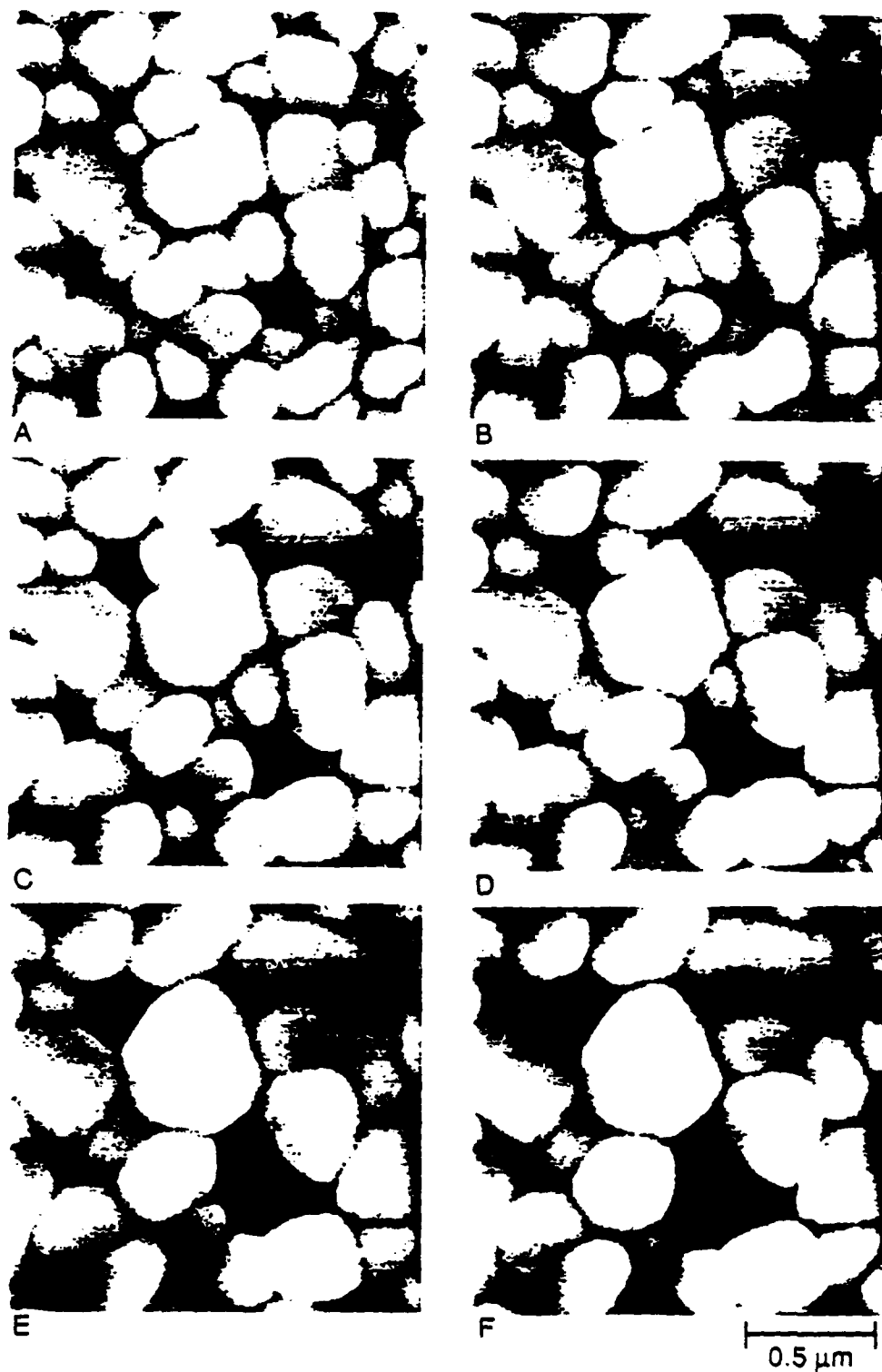


Figure 1. Microstructural evolution of a ZrO_2 (3 mol% Y_2O_3) thin film during heat treatments at 1400 °C. a) 1 h, b) 2 h, c) 3 h, d) 4 h, e) 5 h, f) 6 h.

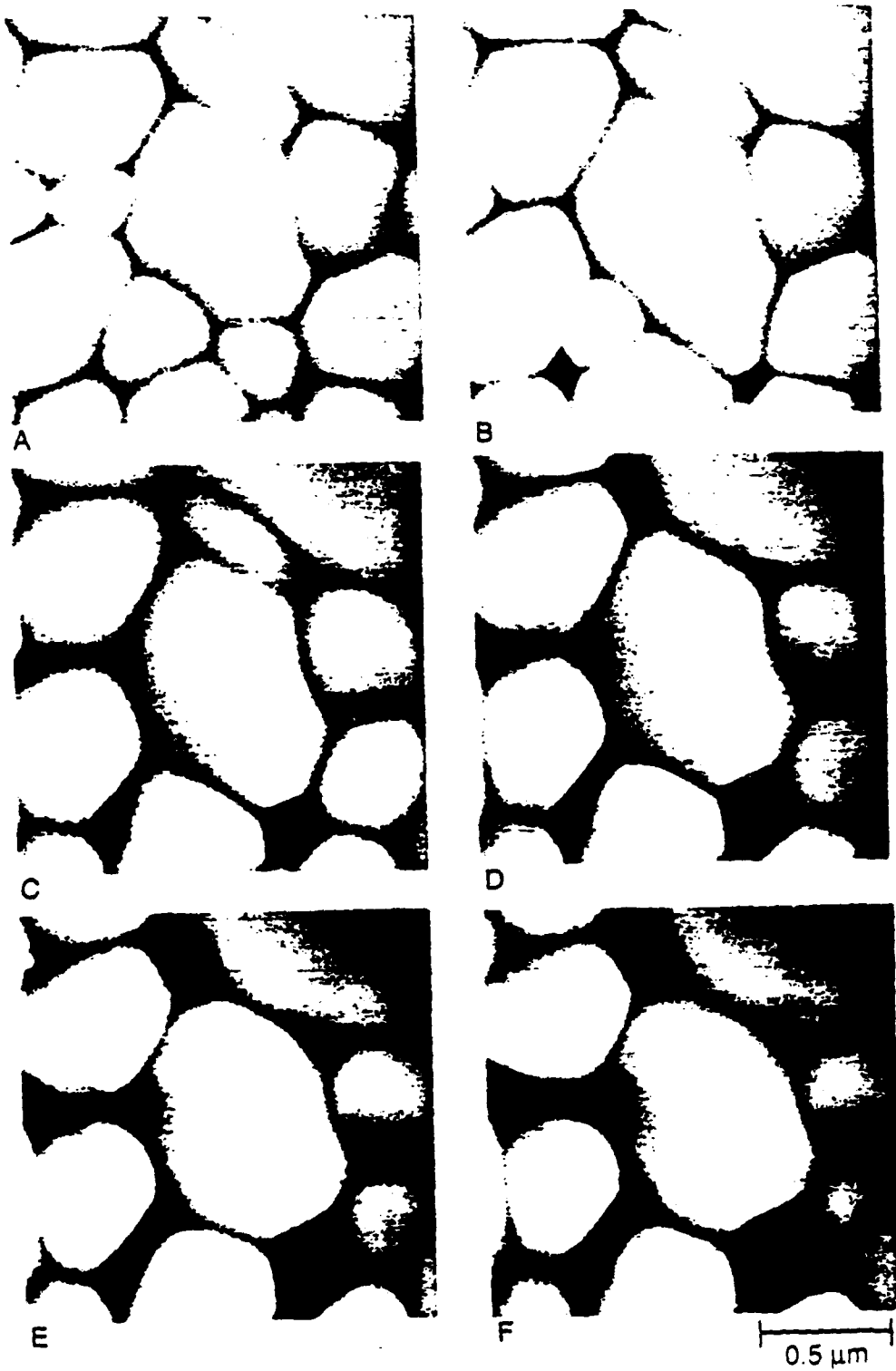


Figure 2. Microstructural evolution of a ZrO_2 (8 mol% Y_2O_3) thin film during heat treatments at 1400 °C. a) 1 h, b) 2 h, c) 3 h, d) 4 h, e) 5 h, f) 6 h.

4. FREE ENERGY CALCULATIONS

To understand this uncovering process, the energetics of the configurational changes associated with grain spheridization was examined. A 2-dimensional analysis was performed. Figure 3 shows the geometrical changes used to model the breakup of thin films. The model film is composed of uniform grains of initial grain size D and thickness t . These grains are allowed to spheridize at constant volume. Initially, the extent of spheridization can be described by the angle ψ . Calculations show that films with an initial D/t ratio less than $8/\pi$ will always retain a boundary between the film grains. Films with a D/t ratio larger than $8/\pi$ will, however, reach a point where the grain boundary disappears. The critical value of ψ where this occurs, ψ_{crit} , is related to D/t through the relationship:

$$\frac{D}{t} = \frac{4(1 + \cos \psi_{crit})}{(\pi - \psi_{crit} - \sin \psi_{crit})} \quad (1)$$

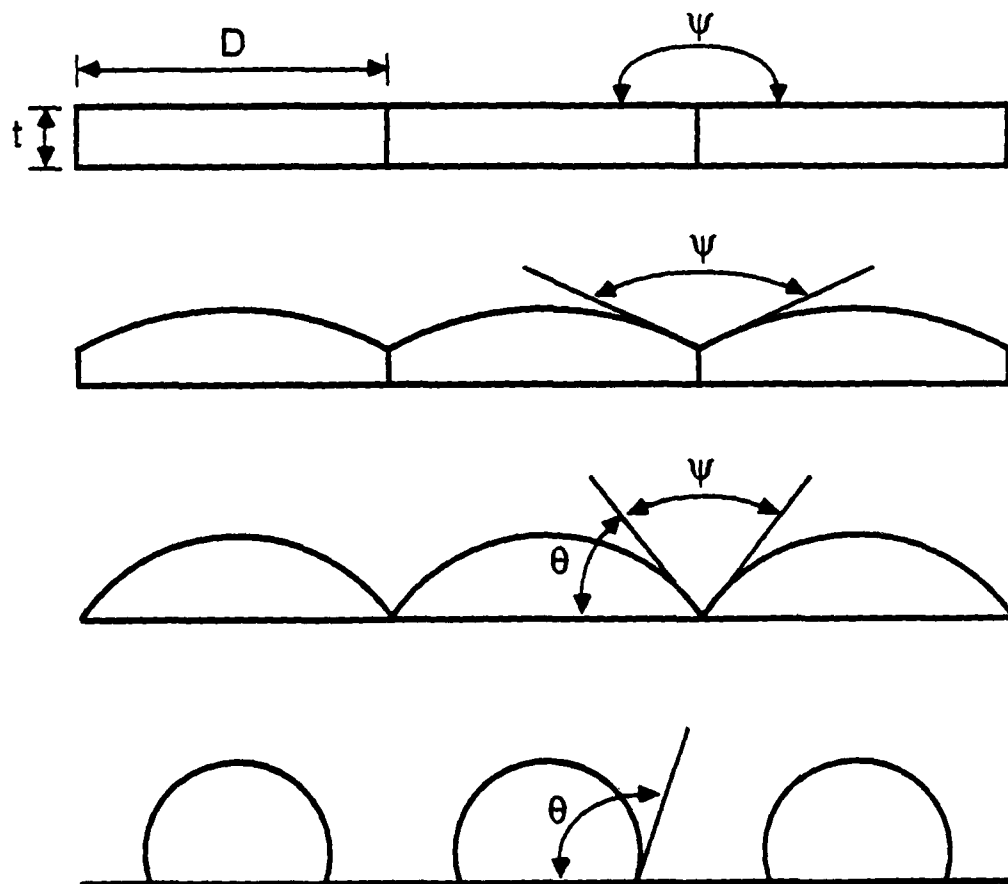


Figure 3. Spheridization of uniform 2-dimensional thin film. Initial thickness t , grain size D .

As shown in Figure 3, further spheridization will result in the uncovering of the substrate. The geometrical configuration can now be described using the angle θ , which is related to ψ by the equation $\theta + \psi/2 = \pi/2$.

The total free energy of the surfaces and interfaces is given, for all film configurations, by the relation:

$$E = A_s \gamma_s + A_b \gamma_b + A_i \gamma_i + A_{sub} \gamma_{sub} \quad (2)$$

where A_s is the film-vapor surface area, A_b the grain boundary area, A_i the film-substrate interfacial area, and A_{sub} the substrate-vapor area. Similarly, γ_s is the film-vapor interfacial energy, γ_b the grain boundary energy, γ_i the film-substrate interfacial energy, and γ_{sub} the substrate-vapor interfacial energy. This function was examined to determine the energy minimum as a function of film geometry. Such a minimum will determine the most stable configuration. The areas in Eq. 2, which are determined by the film geometry, are given as functions of ψ in Table I. Additionally, ratios of the surface energies can be expressed in terms of the equilibrium wetting and dihedral angles (Table II), reducing the number of independent energy variables from four to three.

Table I. Relations Between Areas and ψ

Area	$\psi \geq \psi_{crit}$	$\psi \leq \psi_{crit}$
A_s	$\frac{D(\pi - \psi)}{2 \cos(\psi/2)}$	$D(\pi - \psi) \sqrt{\frac{2t}{D(\pi - \psi - \sin \psi)}}$
A_b	$t - \frac{D(\pi - \psi - \sin \psi)}{4(1 + \cos \psi)}$	0
A_i	D	$2D \cos(\psi/2) \sqrt{\frac{2t}{D(\pi - \psi - \sin \psi)}}$
A_{sub}	0	$D(1 - 2 \cos(\psi/2)) \sqrt{\frac{2t}{D(\pi - \psi - \sin \psi)}}$

Table II. Relations Between Interfacial Energies

Relation	Variable
$\frac{\gamma_b}{\gamma_s} = 2 \cos \frac{\psi_e}{2}$	ψ_e
$\frac{\gamma_b}{\gamma_i} = 2 \cos \frac{\phi_e}{2}$	ϕ_e
$\frac{\gamma_{sub} - \gamma_i}{\gamma_s} = 2 \cos \theta_e$	θ_e

Figure 4 shows typical curves of the configurational energy, normalized by the initial energy, as a function of the geometrical angle ψ . These curves have been calculated for surface energy ratios given by $\psi_e = 120^\circ$, $\phi_e = 60^\circ$, and $\theta_e = 45^\circ$. For $D/t = 8$, the energy is continuously decreased until $\psi = \psi_e$; if ψ is further decreased, and the film force to uncover the substrate, the energy is increased. For these conditions, a continuous film is the most stable configuration. For $D/t = 10$, the energy is again decreased until a minimum is reached. In this case, however, if ψ is decreased past ψ_{crit} , the value of ψ at which the grain boundary disappears, the energy can be further decreased by the film uncovering the substrate. An uncovered substrate is the most stable configuration, and the first minimum is metastable. For $D/t = 13.3$, the grain boundary disappears before even the metastable equilibrium can be reached; in this case, again, an uncovered substrate has the lowest energy.

From such curves, the lowest energy configuration can be determined for any set of initial conditions. The results of such calculations can be shown in an equilibrium configuration diagram, which displays the minimum energy configuration for any desired values of D/t , ψ_e and θ_e . A cross section of this diagram, calculated for $\psi_e = 120^\circ$, is shown in Figure 5. The boundary between the regions is given by the criterion that the minimum energies of the configurations are equal. In general, this criterion is given by:

$$\frac{D}{t} = \frac{2 \cos^2(\psi_e/2)}{\theta_e - \frac{\sin(2\theta_e)}{2} - \frac{p}{4} - \sqrt{\left(\theta_e - \frac{\sin(2\theta_e)}{2}\right)\left(\theta_e - \frac{\sin(2\theta_e)}{2} - \frac{p}{2}\right)}} \quad (3)$$

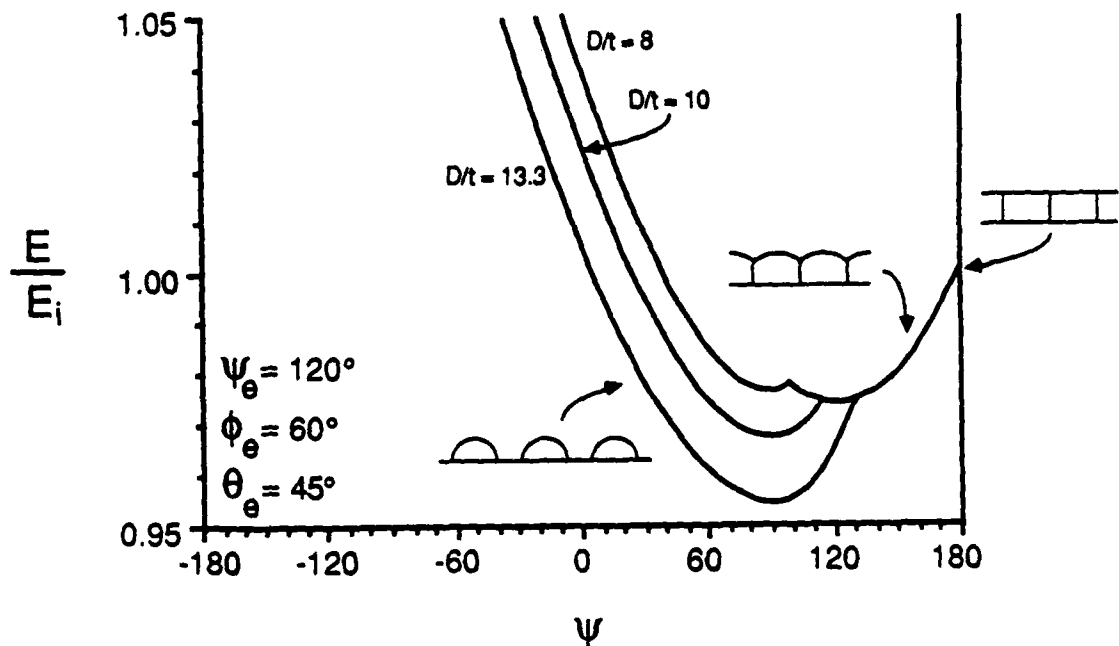


Figure 4. Configurational energy curves for the spheridization of a uniform 2-dimensional thin film, plotted for $\psi_e = 120^\circ$, $\phi_e = 60^\circ$, $\theta_e = 45^\circ$. Upper curve, $D/t = 8$. Middle curve, $D/t = 10$. Lower curve, $D/t = 13.3$.

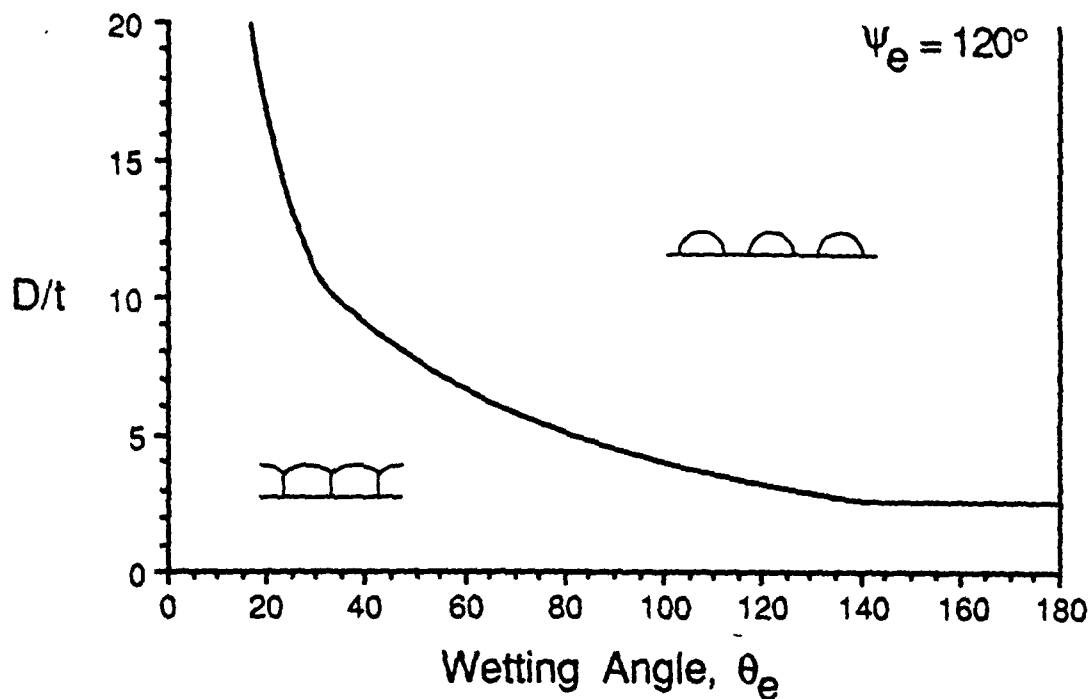


Figure 5. Equilibrium configuration diagram, plotted for $\psi_e = 120^\circ$.

where

$$p = \pi - \psi_e + \sin(\psi_e) - 4 \cos(\psi_e / 2) \cos \theta_e$$

This diagram shows, for any given ratios of the surface energies (as determined by ψ_e and θ_e), the thermodynamically stable thin film configuration for any grain size/film thickness ratio.

5. CONCLUSION

It has been experimentally observed that thin films of ZrO_2 (3 and 8 mol% Y_2O_3) break into islands with grain growth. Thermodynamic calculations show that this break up lowers the free energy of the system. These calculations predict the conditions which will result in a continuous film that is thermodynamically stable. With such knowledge, film break up can be prevented.

REFERENCES

1. F. F. Lange, J. Am. Ceram. Soc. **69** [3] 240-2 (1986).
2. D. J. Srolovitz and S. A. Safran, J. Appl. Phys. **60** [1] 247-54 (1986).
3. D. J. Srolovitz and S. A. Safran, J. Appl. Phys. **60** [1] 255-60 (1986).

Technical Report No. 3

**Morphological Stability of
Polycrystalline Fibers**

by

K.T. Miller and F.F. Lange

**Materials Department
College of Engineering
University of California, Santa Barbara
Santa Barbara, CA 93106**

Grant: AFOSR-87-0291

**Department of the Air Force
Air Force Office of Scientific Research
Electronic and Material Sciences
Bolling Air Force Base, DC 20332-6448**

**THE MORPHOLOGICAL STABILITY
OF POLYCRYSTALLINE FIBERS**

by

K. T. MILLER and F. F. LANGE

Department of Materials
College of Engineering
University of California
Santa Barbara, CA 93106

ABSTRACT

Zirconium acetate (yttrium nitrate) precursor fibers, produced by dry spinning, were placed upon a single crystal Al_2O_3 substrate. Upon heat treatment the precursor fibers pyrolyzed, densified to polycrystalline ZrO_2 (8 mol% Y_2O_3) fibers, and sintered to the substrate. Further heat treatment to induce grain growth produced the following sequential configurational changes: a) grain growth proceeded until single grains would span the fiber to produce a 'bamboo' configuration, b) grain boundary grooves would then deepen and the surfaces between boundaries would become curved, and c) if the fiber diameter was smaller than the distance between grain boundaries, the fiber broke into a row of separate grains. Thermodynamic calculations show that when the grain size to fiber diameter ratio exceeds a critical value, the break up of the fiber into individual grains lowers the free energy. These observations and calculations can be used to predict the conditions required to retain a fiber morphology within composites during high temperature processing and use.

1. INTRODUCTION

The thermal stability of fibers is an important concern in composite materials technology. Fibers can chemically react with the environment and embedding matrix. Mass transport at high temperatures can also lower the free energy of the system by decreasing the interfacial and grain boundary areas. The resultant morphological changes can be dramatic. As we will show for polycrystalline fibers, the mass transport associated with grain growth can lead to the breakup of a continuous fiber into a row of individual grains.

As first shown by Plateau,¹ when the length of a cylinder exceeds a critical value, its surface energy can be decreased by breaking into spheres. Rayleigh² expanded this into his theory of liquid jet instability, which showed that a cylindrical liquid jet of radius r could continuously decrease its surface energy by breaking into droplets when subjected to symmetrical disturbances with wavelengths greater than $2\pi r$. Nichols and Mullins³ extended this concept to solid rods within a solid body. These experimentally verified theories rely on the fact that large amplitude diametrical perturbations can grow by mass transport along the cylinder axis. We will show that such large amplitude perturbations in a polycrystalline cylinder develops by grain boundary grooving, and that grooving will break the fiber into individual grains if the grain size to fiber diameter ratio exceeds a critical value.

Recently, Miller *et. al.*⁴ have shown that the breakup of polycrystalline thin films occurs by a mechanism differing from Rayleigh instability. They observed that initially dense, polycrystalline ZrO_2 films would break first into polycrystalline islands and then into isolated grains as the grain size increased. The surface grains of the dense films had spherical surfaces, and the boundaries between the film grains were grooved to form the equilibrium dihedral angle. Since the grain centers were constrained from moving together by the substrate, the grain boundary grooves became deeper with increased grain size. Eventually, the grain boundaries disappeared to expose the substrate at three grain junctions. A model was developed which considered the total interfacial energy as a function of the film geometry. This model showed that the uncovering process can indeed lower the total interfacial energy of the system and predicted the critical grain size to film thickness ratio above which the uncovered configuration was thermodynamically more stable. Since the grain size to film thickness ratio increases with grain growth, initially dense and thermodynamically stable films which undergo grain growth will eventually enter the regime where the uncovered configuration has the lowest total interfacial energy.

The stability of polycrystalline fibers embedded in a matrix is similar to the thin film problem. Both the fiber and thin film are constrained from shrinking when enlarged grains attempt to develop a spherical surface morphology. In both, therefore, the grain surface and grain boundary

will attempt to approach the equilibrium configuration by grain boundary grooving. Thus, based upon the thin film analogy, one would expect that polycrystalline fibers would break up into individual grains once the grain size to fiber diameter ratio exceeded a critical value. In this study, we first examine the free energy change as a fiber changes from an initial non-equilibrium bamboo grain configuration to an equilibrium configuration. We then test the predictions of this model with direct observations.

2. FREE ENERGY CALCULATIONS

Figure 1 shows the geometrical changes used to calculate the free energy and equilibrium configuration of a polycrystalline fiber. The fiber is embedded within a homogeneous matrix material, which has an interfacial energy with the fiber, γ_s . The initial bamboo structure of the fiber is modeled by identical cylindrical grains of length L and diameter d . The aspect ratio of the grain, $a = L/d$, is used in subsequent calculations. The angle, ψ , defined by the surface normals at the grain boundary, is initially 180° . Two additional geometrical assumptions are needed for an analytical solution. First, it is assumed that the grain centers are fixed and that the grains develop a barrel shape during grain boundary grooving. To model the barrel shape, an arc of a circle is rotated about the central axis. Second, it is assumed that each grain retains its initial mass. With these assumptions, the surface and grain boundary area of each grain can be expressed as a function of ψ , which describes the deepening of the grain boundary groove.

The total free energy of each grain is given by:

$$E = A_s \gamma_s + A_b \gamma_b \quad (1)$$

where A_s is the grain surface area, A_b is the grain boundary area, γ_s is the interface energy, and γ_b is the grain boundary energy. The surface energies are related through Young's relation:

$$\frac{\gamma_b}{\gamma_s} = 2 \cos \frac{\psi_e}{2} \quad (2)$$

where ψ_e is the equilibrium dihedral angle.

Using the Theorem of Pappus, the grain surface area, A_s , can be shown to be given by:

$$A_s = \frac{\pi a}{\sin \alpha} \left[\alpha r_f + a (1 - \alpha \cot \alpha) \right] d^2 \quad (3)$$

where $\alpha = (\pi - \psi) / 2$, and r_f is the ratio of the grain boundary radius to the initial cylinder radius. The expression for r_f , determined by equating the grain volume to the initial cylinder volume, is given by:

$$r_f = -\frac{a}{2b} + \frac{1}{2} \sqrt{a^2 \left(\frac{1}{b^2} + \frac{4 \cot \alpha}{b} - \frac{8}{3} \right) + 4} \quad (4)$$

where

$$b = \frac{\sin^2 \alpha}{\alpha - \sin \alpha \cos \alpha}$$

The grain boundary area, A_b , is given by the expression:

$$A_b = \frac{\pi}{4} r_f^2 d^2 \quad (5)$$

Substituting these expressions into eq. (1), and normalizing by the energy of the initial cylindrical configuration, the free energy of the grain configuration, E_f , can be expressed as:

$$E_f = \frac{\frac{2a}{\sin \alpha} [\alpha r_f + a (1 - \alpha \cot \alpha)] + r_f^2 \cos\left(\frac{\psi_e}{2}\right)}{2a + \cos\left(\frac{\psi_e}{2}\right)} \quad (6)$$

This expression describes the normalized free energy as ψ decreases from 180° to the value of ψ where the grain boundary disappears ($r_f = 0$); beyond this point, the grains will become spherical. The free energy, E_s , of a spherical grain whose volume equals the initial cylinder, normalized by the initial energy of the cylindrical grain, is given by:

$$E_s = \frac{2\left(\frac{3a}{2}\right)^{\frac{2}{3}}}{2a + \cos\left(\frac{\psi_e}{2}\right)} \quad (7)$$

Figure 2 shows the normalized energy plotted as a function of the configurational angle ψ for an equilibrium dihedral angle, ψ_e , of 150° (a typical value in ceramic materials for a solid-gas interface). The free energy behavior is plotted for three increasing grain size aspect ratios; for a fixed fiber diameter, the aspect ratio will increase as the grain size increases. For each case, the free energy, E_f , is plotted as ψ decreases from 180° to the value of ψ where the grain boundary disappears ($r_f = 0$). Beyond this point, the curve is assumed to change continuously until it coincides with the normalized free energy of the sphere, E_s , i.e., when $\psi = 0$.

As shown in Fig. 2 the free energy of the fiber with the smallest aspect ratio, $a = 1.5$, decreases to a minimum while the fiber is still continuous; for this minimum ψ is near ψ_e . Since any further decrease in ψ will increase the free energy, the continuous fiber is the equilibrium configuration. For an increased aspect ratio of $a = 2$, the normalized free energy again decreases to a minimum corresponding to a continuous fiber. In this case, further decreasing ψ would first increase and then decrease the free energy of the fiber, reaching another minimum for a row of spherical grains. The minimum free energy of the connected fiber is higher than that of the unconnected spheres. Thus for this case, the intact configuration is metastable, viz., to achieve the equilibrium configuration, an energy barrier must be overcome. When the aspect ratio is further increased to $a = 3$, the row of spherical grains again has the lowest free energy. In this case the free energy continuously decreases with ψ . Such fibers will always break into a row of spheres, provided that mass transport can occur.

As shown by Miller *et al.*⁴ for thin films, the lowest energy configuration for any given set of initial conditions can be represented with an equilibrium configuration diagram. For polycrystalline fibers, the minimum energy configuration can be displayed as regions in aspect ratio vs. equilibrium dihedral angle (a vs. ψ_e) space. The boundary between these regions is determined by the condition that both configurations have identical free energies, which can be expressed by the system of equations:

$$\frac{\partial E_f}{\partial \psi} = 0 \quad (8a)$$

$$E_f^{\min} = E_s \quad (8b)$$

Equation (8a) determines the angle ψ where the free energy of the intact fiber is a minimum. Equation (8b) then equates the energy at this angle to the energy of the row of identical spheres. The numerical solution to these conditions is shown as the solid line in Figure 3, the equilibrium configuration diagram. Whenever the initial conditions of a and ψ_e fall below this line, the lowest free energy configuration is a continuous fiber. Above this line, the lowest free energy configuration is a row of identical spheres.

The region of continuous fiber metastability can also be illustrated on the equilibrium configuration diagram. In this region, which is illustrated by the middle curve $a = 2$ in Figure 2, an energy barrier must be overcome. The lower bound of this region is again given by equation (8) and shown as the solid line in Figure 3. The upper bound is determined by the condition that the free energy function (eq. 6) displays an inflection such that:

$$\frac{\partial E_f}{\partial \psi} = 0 \quad (9a)$$

$$\frac{\partial^2 E_f}{\partial \psi^2} = 0 \quad (9b)$$

For any given value of ψ_e , this set of equations will give the minimum aspect ratio for which the energy barrier disappears. The solution to this set of equations is given by the dashed line in the equilibrium configuration diagram (Figure 3). With the region defined by the solid and dashed lines, either configuration (continuous metastable fiber or row of spherical grains) can exist.

3. EXPERIMENTAL OBSERVATIONS

ZrO₂ (8 mol% Y₂O₃) fibers were drawn from acetate precursors, whose fiber forming abilities have been previously explored.⁵⁻⁹ Yttrium nitrate, sufficient to produce 8 mol% Y₂O₃ in the pyrolyzed fibers, was added to the zirconium acetate solutions. ZrO₂ (8 mol% Y₂O₃) has a cubic crystal structure and undergoes rapid grain growth¹⁰ at 1400 °C. The dried, precursor fibers were placed on single crystal Al₂O₃ substrates, pyrolyzed and densified by heating to 1000 °C at a rate of 5 °C/min, and subsequently subjected to a series of heat treatments at 1400 °C. Observations showed that the fibers sintered to the Al₂O₃ substrate. After each heat treatment, the microstructure of relocatable fiber areas were examined using SEM.

Figure 4 shows the microstructural evolution of a polycrystalline ZrO_2 fiber. After pyrolysis, a dense, polycrystalline fiber was formed. As the heat treatment period increased, the grains in the fiber grew until each grain spanned the entire fiber diameter, producing a 'bamboo' configurations with shallow grooves at the boundaries of the cylindrical grains. When subjected to heat treatment beyond that needed to form the 'bamboo' configuration, grain boundary positions stabilized and grain boundary grooves deepened.

Figure 5a shows the microstructure of a fiber whose diameter decreases along its length; it best illustrates the conditions of stability and instability discussed previously. This fiber was treated for 40 h at 1400 °C. Figures 5b-f, higher magnifications of evenly spaced areas along the fiber, shows that the intergranular spacing remains approximately constant (number of grains for identical lengths range between 10 to 12) while the fiber diameter decreases. The aspect ratio (grain size/fiber diameter) therefore increases along the length of the fiber. The section of the fiber with the smallest aspect ratio (Figure 5b) has developed barrel shaped grains. The grains in this micrograph have an average aspect ratio of 1.0. As the aspect ratio increases the grain boundary grooving of the barrels becomes more pronounced (Figure 5c). In this micrograph, the average aspect ratio is 1.4. As the aspect ratio is increased further, the fiber breaks into triplets (Figure 5d), doublets (Figure 5e), and finally single particles (Figure 5f). These observations are consistent with the free energy calculations presented above for the case where ψ_e lies between 120° and 160°, which can be estimated from Fig. 5b.

4. CONCLUSIONS

Polycrystalline fibers of ZrO_2 (8 mol% Y_2O_3), constrained from shrinking by a substrate, are observed to achieve a 'bamboo' morphology through grain growth. With further heat treatment, grain boundary grooves deepen. As the grain size to fiber diameter ratio increases, a continuous fiber breaks into a row of particles. Thermodynamic calculations show that this lowers the free energy of the system. These calculations predict, for any given equilibrium dihedral angle, the critical grain aspect ratio at which a continuous fiber can lower its free energy by breaking into a row of spheres. They also show that fibers are most stable for large values of the equilibrium dihedral angle, which correspond to low values of the grain boundary energy to surface energy ratio.

Several steps can be taken to prevent fiber breakup. First, the grain boundary energy to surface energy ratio should be as small as possible, ensuring maximum fiber stability. More importantly, grain growth in the fiber must be controlled so that critical grain aspect ratio is never exceeded.

5. ACKNOWLEDGEMENT

This work was supported by the Air Force Office of Scientific Research, under Contract Number AFOSR-87-0291.

6. REFERENCES

1. J. Plateau, *Statique expérimentale et théorique des liquides soumis aux seules forces moléculaires*, Paris, 1873.
2. J. S. W. Rayleigh, *Theory of Sound*, Volume II, Dover, New York, 1945.
3. F. A. Nichols and W. W. Mullins, "Morphological Changes of a Surface of Revolution to Capillarity-Induced Surface Diffusion," *J. Appl. Phys.*, 36 1826 (1965).

4. K. T. Miller, F. F. Lange, and D. B. Marshall, "The Instability of Polycrystalline Thin Films: Experiment and Theory" in *Better Ceramics Through Chemistry III*. Edited by C. J. Brinker, D. E. Clark, and D. R. Ulrich, The Materials Research Society, 1988 (to be published).
5. D. B. Marshall, F. F. Lange, and P. E. D. Morgan, "High-Strength Zirconia Fibers," *J. Am. Ceram. Soc.*, 70 [8] C-187-C-188 (1987).
6. M. E. Khavari, F. F. Lange, P. Smith, and D. B. Marshall, "Zirconia Fibers: Strength Processing Relations" in *Better Ceramics Through Chemistry III*. Edited by C. J. Brinker, D. E. Clark, and D. R. Ulrich, The Materials Research Society, 1988 (to be published).
7. M. J. Morton, J. D. Birchall, and J. E. Cassidy, "Fibers," Brit. Pat. No. 1 360 199 (1974).
8. E. Leroy, C. Robin-Brosse, and T. P. Torre, "Fabrication of Zirconia Fibers from Sol Gels," p. 219-31 in *Ultrastructure Processing of Ceramics, Glasses, and Composites*. Edited by L. L. Hench and D. R. Ulrich, Wiley, New York, 1984.
9. J. E. Blaze, "Process of Manufacturing Refractory Fibers," U. S. Pat. No. 3 332 865 (1967).
10. F. F. Lange, "Transformation-Toughened ZrO_2 : Correlations Between Grain Size Control and Composition in the System ZrO_2 - Y_2O_3 ," *J. Am. Ceram. Soc.*, 69 [3] 240-2 (1986).

FIGURE CAPTIONS

- Figure 1. Model microstructural evolution of a polycrystalline fiber. The initial fiber has a 'bamboo' grain morphology, with grain length L and fiber diameter d . As ψ decreases from 180° , the grains become barrel shaped and finally break into a row of spheres.
- Figure 2. Configurational energy curves for the microstructural evolution of a polycrystalline fiber, plotted for three values of the grain aspect ratio a . Upper curve, $a = 1.5$. Middle curve, $a = 2.0$. Bottom curve, $a = 2.5$. All are plotted for the equilibrium dihedral angle $\psi_e = 150^\circ$.
- Figure 3. Equilibrium configuration diagram of a polycrystalline fiber. Above the solid line, a row of spherical grains is the equilibrium configuration. Above the dashed line, a fiber can continuously decrease its free energy by breaking into a row of spherical grains.
- Figure 4. Microstructural evolution of a polycrystalline ZrO_2 (8 mol% Y_2O_3) fiber, heat treated at $1400^\circ C$. a) Fiber heated to $1400^\circ C$ and cooled. b) 1 h. c) 3 h. 'Bamboo' morphology complete. d) 20 h. Grain boundary grooves deepening.
- Figure 5. a) ZrO_2 (8 mol% Y_2O_3) fiber with decreasing diameter, heat treated at $1400^\circ C$ for 40 h. As the fiber diameter decreases, the grain boundary grooving becomes more pronounced and the fiber breaks into individual grains. b-f) Higher magnification of evenly spaced areas of the fiber.

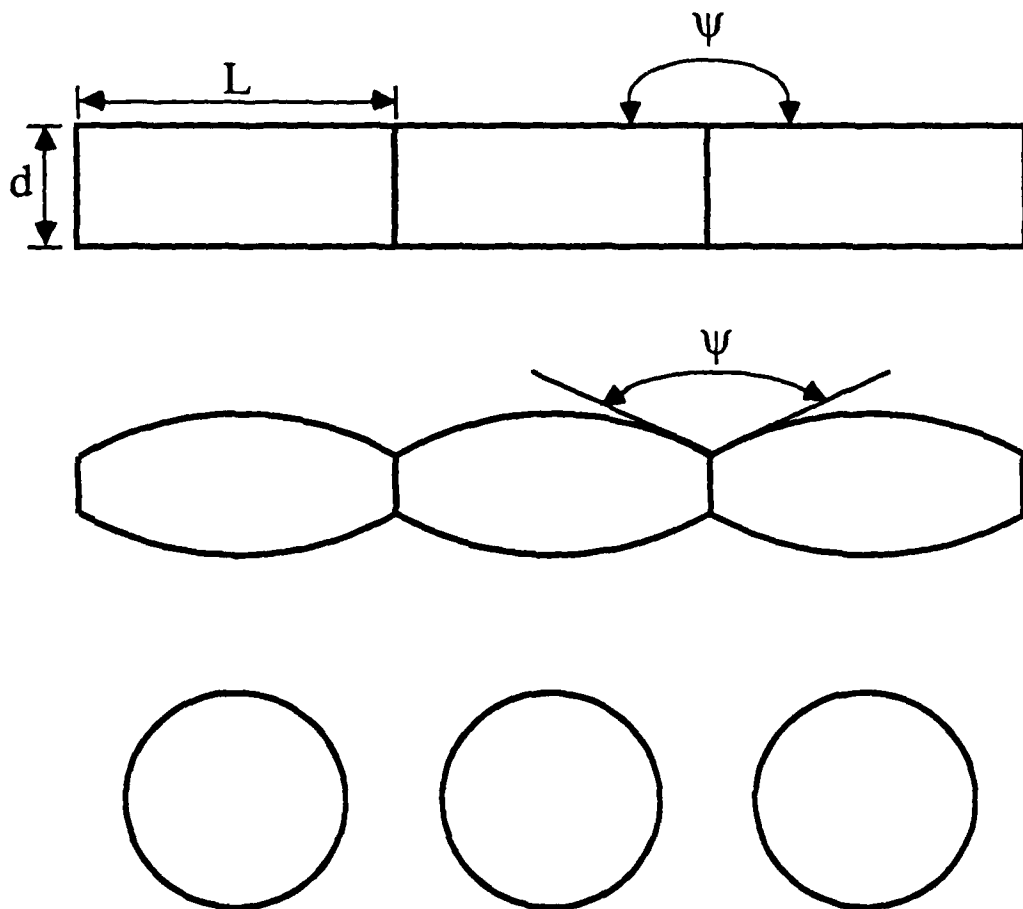


FIGURE 1

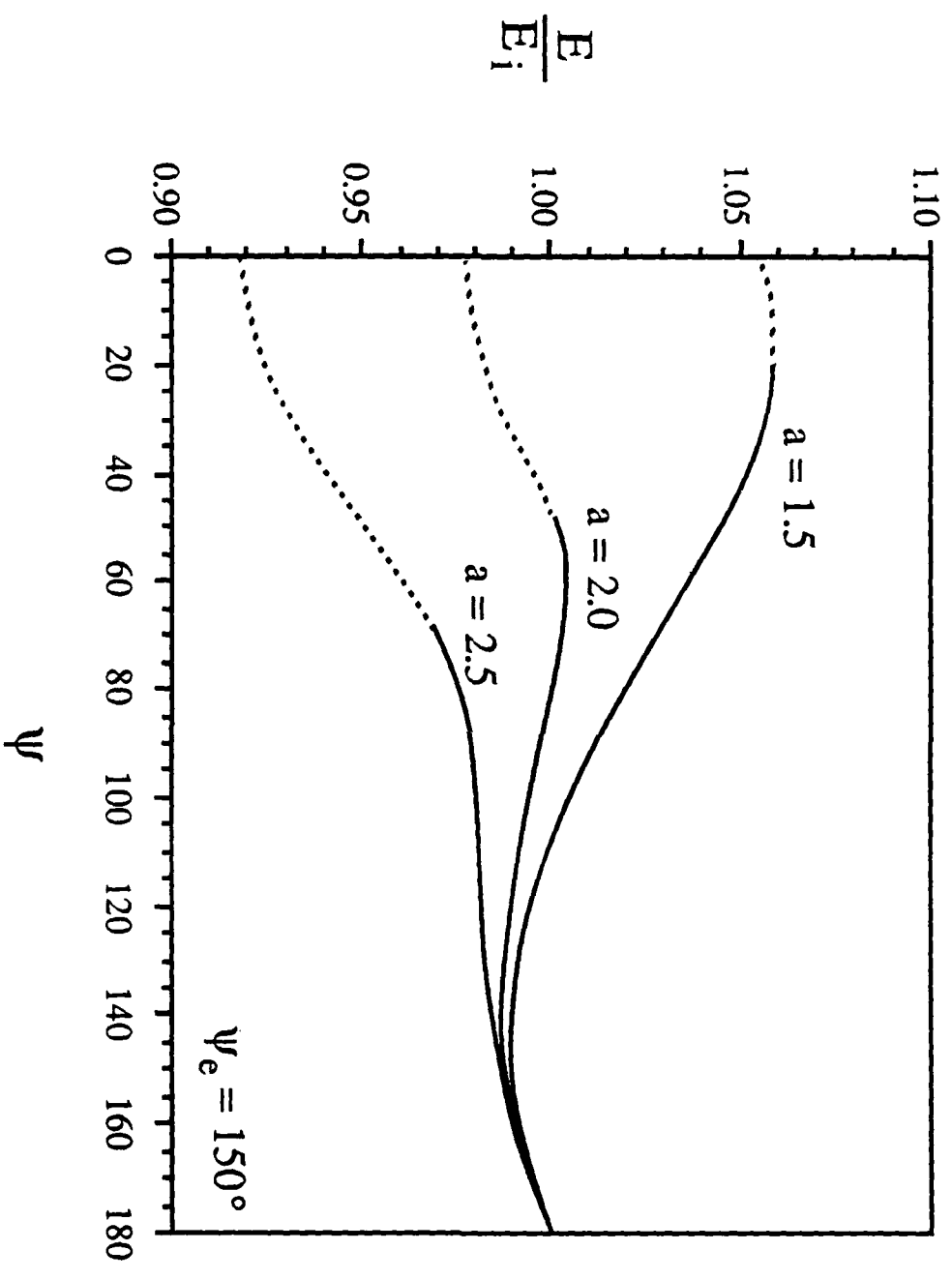


FIGURE 2

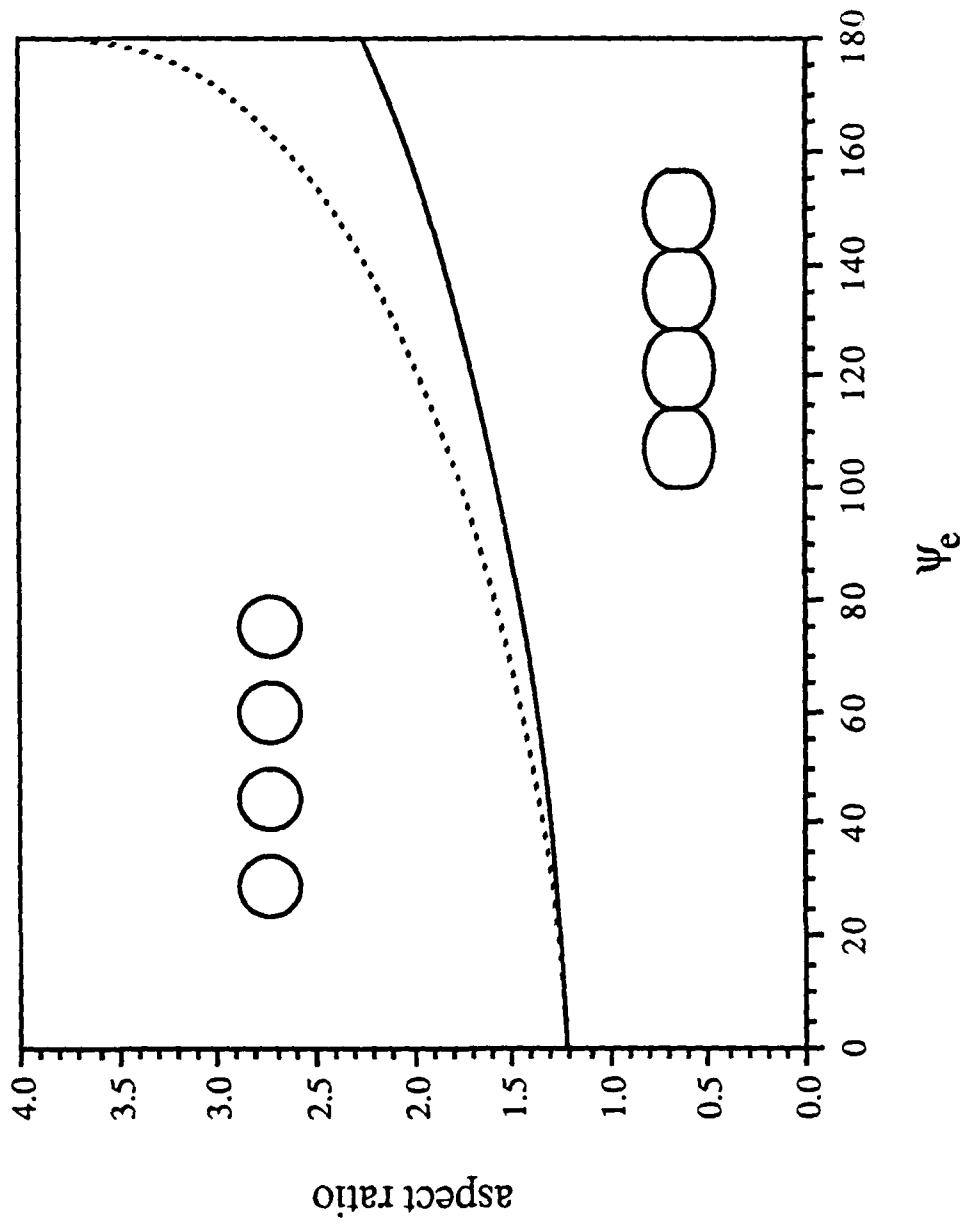


FIGURE 3

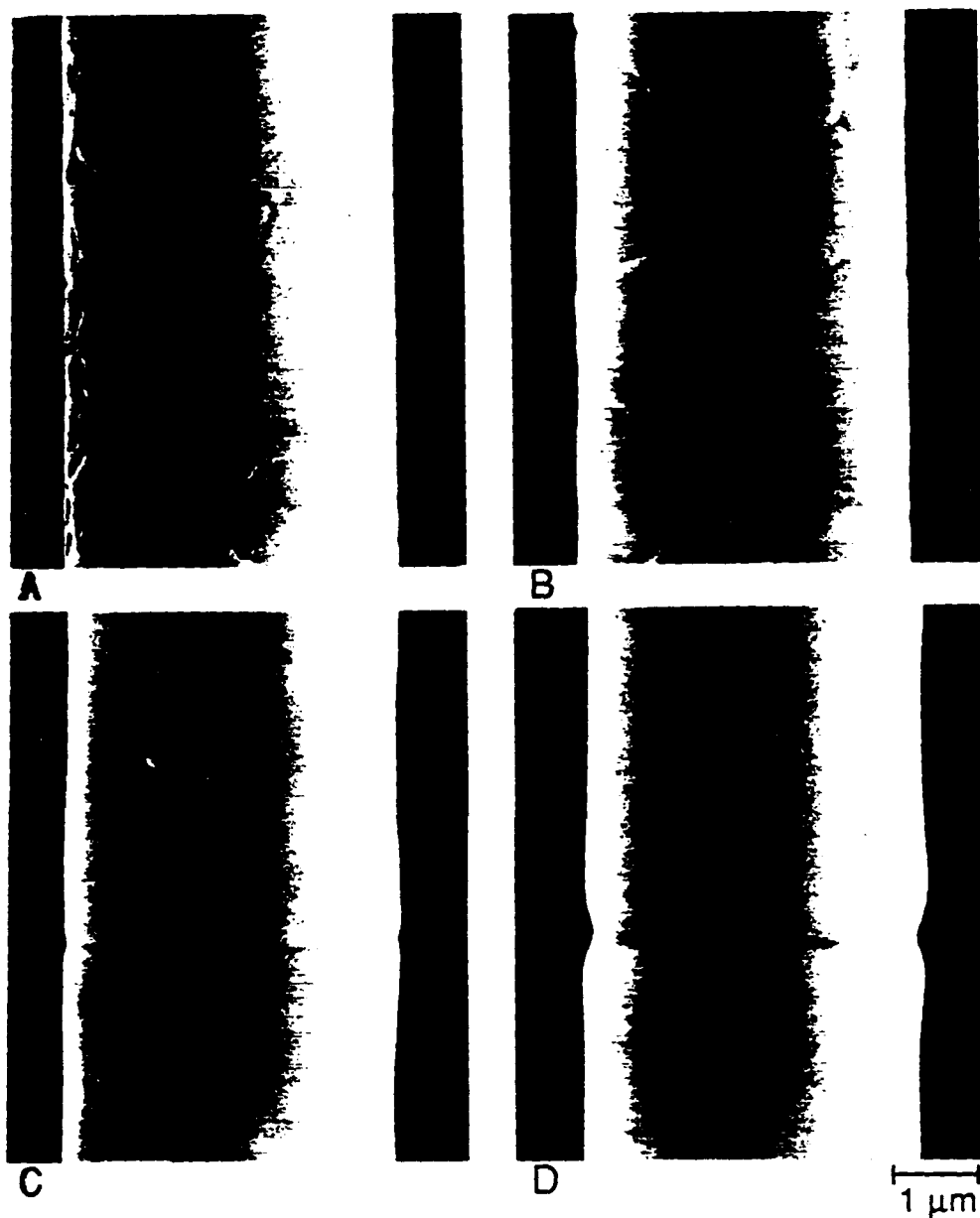


FIGURE 4

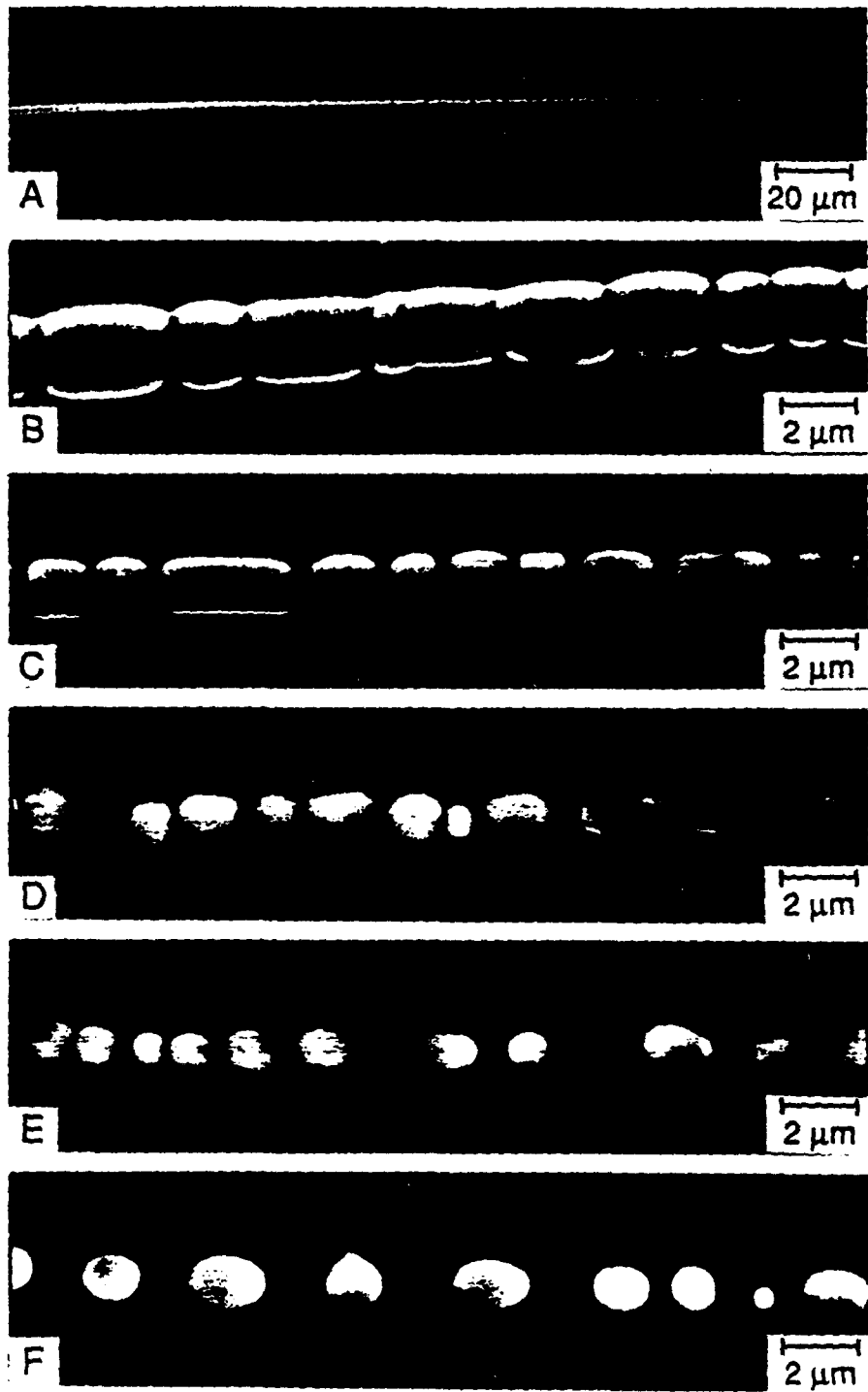


FIGURE 5

Technical Report No. 4

**Powder Processing Science and
Technology for Increased Reliability**

by

F. F. Lange

**Materials Department
College of Engineering
University of California, Santa Barbara
Santa Barbara, CA 93106**

Grant: AFOSR-87-0291

**Department of the Air Force
Air Force Office of Scientific Research
Electronic and Material Sciences
Bolling Air Force Base, DC 20332-6448**

Powder Processing Science and Technology for Increased Reliability

F. F. Lange

**Materials Department
College of Engineering
University of California
Santa Barbara, CA 93106**

Abstract

More reliable ceramics require improved processing reliability. Heterogeneities bought with powders and those inadvertently introduced during processing as well as non-uniform and undefined phased distributions contribute to unreliable processing. Colloidal powder treatments can eliminate many heterogeneities and ensure more uniform phase distributions. New slurry consolidation methods, which do not produce disruptive phenomena, are required to shape colloidally treated powders. Particle packing during consolidation is critical to densification by heat treatment. Microstructures developed during and subsequent to densification must be controlled. Each of these subjects, viz., heterogeneities, colloidal methods for preparing and mixing powders, slurry consolidation, particle packing, densification, and control of grain growth are reviewed to illustrate new approaches and thinking directed to increase the engineering reliability of ceramics processed with powders.

Sosman Memorial Lecture

**Presented: Annual Meeting of the American Ceramic Society
May, 1987**

To be published by the American Ceramic Society, 1988

Introduction

With their multiplicity of elemental combinations and crystal structures, ceramics have a multitude of unique properties that are still being uncovered. Ceramics are needed to implement many technology scenarios ranging from advanced heat engines to energy transmission.

Ceramic processing technology has advanced little beyond the needs of functional ceramics. Traditional ceramic processing inherently lacks a clear approach for controlling microstructure heterogeneities and microstructure uniformity. Property variability and thus, ambiguous engineering reliability, stems from uncontrolled microstructures. Engineering reliability is a matter of processing reliability.

Most forming methods are generally unacceptable for ceramics. Their brittle nature preclude deformation methods commonly used for metals. Melt casting produce friable ceramics due, in part, to uncontrolled grain growth during solidification. Some advanced ceramics, viz., Si_3N_4 and SiC , decompose prior to melting. Glass-ceramic processing, a special melt forming method that takes advantage of Newtonian rheology to form shapes and crystallization after solidification to control microstructure, produces non-equilibrium phase assemblages and is limited to glass forming chemistries. Columnar grain growth and uneconomical deposition rates are disadvantages for chemistries that can be shaped by vapor condensation methods. Liquid precursor methods, e.g., sol-gel processing, suffer from large volume changes during fluid removal, pyrolysis, and/or densification that limits this method to shaping small bodies, i.e., particles, thin films and fibers. Most advanced ceramics are formed as powder compacts made dense by heat treatment. Although powder processing is a many bodied problem prone to heterogeneities and non-uniform phase distributions, it is the most efficient method to form ceramics. The object here will be to review new approaches and thinking to increase the engineering reliability of ceramics processed with powders.

Heterogeneities Common To Powder Processing

Powder processing involves four basic steps: 1) powder manufacture, 2) powder preparation for consolidation, 3) consolidating to an engineering shape, and 4) densification/microstructural development that eliminates void space and produces the microstructure that optimizes properties. Each step has the potential for introducing a detrimental heterogeneity which will either persist during further processing or develop into a new heterogeneity during densification and microstructural development.

Since the number of heterogeneities per unit volume can be small, they are best observed with an experiment sensitive to heterogeneities. Since strength is sensitive to stress concentrators, microstructural heterogeneities that are stress concentrators can be best observed by fracture and examining fracture origins*. As schematically illustrated in Fig. 1, many different heterogeneities may co-exist. Each can be viewed as a strength limiting flaw population, introduced during some stage of processing. The ordering of the common flaw populations shown in Fig. 1 and their strength-size distribution depends on the material and its processing. For example, some materials such as SiC and β -Al₂O₃ are prone to develop a microstructure containing large, plate-like grains. These plate-like grains can be the first flaw population uncovered during strength determinations, whereas some other flaw population, e.g., crack-like voids produced by the differential shrinkage of agglomerates, can be the dominate heterogeneity observed either in the same materials processed in a different manner or in other materials not prone to abnormal grain growth. Once the dominate flaw population is identified and eliminated by processing changes, another flaw population with a higher mean strength will be uncovered. Its strength-size distribution will now dominate strength statistics. The processor interested in eliminating heterogeneities must first identify the dominate heterogeneity observed at fracture origins, ascertain how this heterogeneity is introduced during processing, and then make the appropriate processing changes to eliminate the heterogeneity. This is an iterative scheme.

Many microstructure heterogeneities stem from the powder itself. Agglomerates are a major heterogeneity in powders. The attractive interparticle forces responsible for free particle agglomeration include Van der Waals and capillary forces. Capillary forces are produced when water vapor condenses at particle contacts. Particles can also cement together after a fluid has been removed by evaporation leaving behind previously soluble salts (e.g., with hydroxides) at contact positions. Most ceramic powders are manufactured by decomposing and/or reacting a precursor at moderate temperatures. Nanometer size crystallites formed during pyrolysis, sinter together to a continuous low density crystallite network. When the pyrolyzed material is milled to make particles, the resulting particles can be partially dense, sintered crystallites, i.e., very strong agglomerates.

* The strength of several ceramics can be relatively insensitive to flaw size and thus insensitive to flaws introduced during processing. These ceramics include optimally aged transformation toughened ZrO₂¹ and certain fiber composites with very weak fiber-matrix interfacial bond strengths². These relatively few ceramics possess a toughening mechanism that increase the material's resistance to crack growth, i.e., critical stress intensity factor, as the crack grows. Unfortunately, these special toughening mechanisms are currently limited to certain material systems and temperatures, but when fully exploited, could result in structural ceramics that are relatively insensitive to flaw populations introduced during processing and thus produce a material with a relatively narrow strength distribution, i.e., high Weibull Modulus.

Current consolidation technology is based on dry pressing requiring flowable powders to uniformly fill die cavities. Particles within dry powders are held together by attractive van der Waals forces. Flowable powders require large particles because the separating force produced by differential acceleration during flow is proportional to particle mass. Since the separating force produced by the micron size particles desired for ceramic processing are insufficient to overcome attractive (e.g., van der Waals) forces, ceramic powder slurries containing polymer additions are spray dried to purposely form large ($> 50\mu\text{m}$) agglomerates and a flowable powder.

Agglomerates with different bulk densities can persist during powder consolidation to form crack-like voids during densification due to their different shrinkage relative to the surrounding powder compact.³ Agglomerates purposely produced by spray drying may not uniformly deform to fill interagglomerate void space⁴ during consolidation. They will leave irregular voids that persist after densification. Agglomerates also limit densification.^{5,6}

Powders contain organic and inorganic inclusions introduced both by the manufacturer and during powder preparation for consolidation by the processor. Some of these heterogeneities are introduced when powders are milled to reduce the size of hard agglomerates and/or simply exposed to the environment. Organic inclusions disappear during densification to leave irregularly shaped voids.⁷ Inorganic inclusions can react with the powder during densification and/or produce microcracks either during cooling from the densification temperature or upon subsequent stressing. Clean rooms are ineffective because the manufacturer supplies the inclusions with the powder.

Post-densification hot gas isopressing can eliminate some voids that remain after pressureless densification.⁸ Recent results strongly suggest that void closure occurs by deformation⁹ and crack-like voids, e.g., produced by the differential shrinkage of agglomerates, are the first to close.¹⁰ Unfortunately post-densification hot gas isopressing can not eliminate pores that intersect the surface and other heterogeneities, e.g., inclusions. In addition, post-densification hot gas isopressing can exaggerate the size of voids just beneath the surface when the ligament separating the void from the surface punctures by deformation.⁹

Many advanced ceramics contain more than one phase and are produced by mixing two or more powders prior to consolidation and densification. As discussed below, a second phase can be used to eliminate abnormally large grains which are common heterogeneities developed during densification of non-cubic crystalline structures. Phase homogeneity is a major issue in these multiphase ceramics, and even when the

desired homogeneity is obtained during mixing, heterogeneities can arise if mass segregation occurs by sedimentation after mixing.

If reliable ceramics are to be produced, methodologies must be developed to insure, with a high probability, that heterogeneities will be eliminated from powders and that they will not be reintroduced in subsequent processing steps. As discussed in the next section the colloidal approach has this potential.

The Colloidal Approach

Heterogeneities must be fractionated from current powders. When technologies develop to produce powders free of heterogeneities, a methodology must be available to handle these powders without introducing heterogeneities. Powders must flow to fill either die cavities or molds to consolidate shapes. Once a powder is fractionated and made flowable, powders can not be exposed to an uncontrolled environment prior to consolidation. As it will become evident, the colloidal approach is consistent with these requirements.

Many of the heterogeneities discussed above can be eliminated from their source, i.e., the powder, by manipulating and controlling interparticle forces as taught by colloid science. Certain aspects of colloidal processing require repulsive interparticle forces, while others require attractive forces. Powders disperse to form a system of separated particles when repulsive forces dominate and floc to form a low density network of touching particles when attractive forces dominate. Repulsive interparticle forces are used to break apart weak agglomerates, fractionate a desired particle size distribution, fractionate strong agglomerates and inclusions greater than a given size, and mix different fractionated powders together. Once fractionated and mixed, the interparticle forces can be made attractive to form a low density, deformable network that prevents mass segregation.

Slurry rheology depends on interparticle forces and particle volume fraction. ^{11,12} Dispersed slurries exhibit Newtonian rheology (viscosities independent of shear rate). At high volume fractions they become dilatant (viscosity increases with shear rate) as the system must increase its volume to allow closely spaced, repulsive particles to slip past one another. Flocced slurries exhibit thixotropic rheology (viscosity decreases with increasing shear rate and history dependent viscosity), because the applied forces separating attractive particles depends on differential acceleration (shear rate). Once separated, flocculation and network formation is time dependent. Pourable, dispersed slurries can contain up to 60 volume % solids, whereas the volume fraction of pourable, flocced slurries is much lower (between 0.05 and 0.2) and depends on the particle mass (size) which governs the forces separating particles during flow.

A number of basic interactions can be used to alter interparticle forces ¹³. These include attractive van der Waals forces, repulsive electrostatic forces, steric forces (attractive or repulsive), and attractive capillary forces. With the exception of van der Waals forces, the manipulation of interparticle forces usually requires the addition of a surface active agent to a liquid/particle system. Electrostatic repulsive forces develop when solute ions are attracted to or dissociated from particle surfaces to produce a system of similarly charged particles. Steric forces are developed by macromolecules that attach themselves to the particle's surface. Charged macromolecules, i.e., polyelectrolytes, can produce both repulsive electrostatic and steric forces. Although the science of interparticle forces has a strong theoretical base, verified through direct surface force measurements ¹³, the choice of the best surface active agent used to control interparticle forces is still a matter of trial and error for most ceramic systems.

Figure 2 illustrates one colloidal approach to treat and store ceramic powders prior to consolidation. ⁷ As received, dry powders are dispersed in an appropriate fluid with a surfactant that produces interparticle repulsive forces. These repulsive forces keep particles separated once shearing forces break apart weak agglomerates. Partially sintered and other strong agglomerates which can not be broken apart and inorganic inclusions greater than a given size are eliminated by sedimentation. This step can be accelerated by centrifuging. After removing the undesired larger particles, strong agglomerates and inclusions, the retained dispersed slurry containing the desired particles is flocced by changing the interparticle forces from repulsion to attraction. Floccing concentrates the particles to form a weak, continuous touching network which consolidates under its own weight, partially separating the particles from the fluid phase. Flocced slurries can be washed to remove excess salts and/or surfactants. Centrifuging can further concentrate this particle network. As discussed below, floccing also prevents mass segregation during storage even when acted upon by centrifugal forces.

Figure 2 also shows that two or more powder phases, separately treated as summarized above, can be mixed together to form multiphase slurries. If the different slurries are colloiddally compatible, i.e., do not floc one another, they can be redispersed (by again adding the proper surface agent) and mixed. More commonly, the phases are not colloiddally compatible. These systems can still be mixed because flocced mixtures can be mechanically redispersed by a device that produces a high shear-rate (an ultrasonic horn, high speed rotors, etc.). As the mechanically dispersed mixture leaves the high shear-rate field, it flocs to form a new, mixed particle network which prevents phase separation during storage and further processing.

The effect of interparticle forces on mass segregation due to sedimentation was investigated ¹⁴ by centrifuging both dispersed and flocced slurries containing a mixture of Al₂O₃ and ZrO₂ (30 volume %) powders colloidally treated and mixed as described above^{**}. The centrifuged masses were dried, densified and sectioned to examine phase distribution in the scanning electron microscopy using energy dispersion x-ray (EDX) analysis. Figure 3 illustrates the Zr/Al count ratio vs the normalized distance from the bottom to the top of the sintered, centrifuged mass. As shown, this ratio was nearly constant ($\pm 3\%$) across the specimen prepared from the flocced mixture and equal to that of the initial composited mixture. As expected, the dispersed slurry produced different results. First, although the Zr/Al count ratio was nearly constant ($\pm 13\%$) across $\sim 90\%$ of the normalized specimen thickness, it significantly increased near the top of the specimen. Second, the average Zr/Al count ratio corresponded to only ~ 14 volume % ZrO₂; much of the smaller, less massive ZrO₂ particles were left behind in the centrifuged supernatant. In addition, as shown in Fig. 4, larger particles of both phases were observed at the bottom of the specimen, and smaller particles at the top. Similar observations showed that both the phase distribution and the size of each phase was uniform through out the specimen prepared from the flocced slurry. These results clearly show that the touching particle network within a flocced slurry can prevent mass segregation due to sedimentation.

The question concerning mixed phase uniformity and what tools can be used to define its uniformity has recently been addressed ¹⁵. The method is simple and can be related to the slurry rheology ¹⁶, and it has potential to access mixing uniformity during processing as a non-destructive evaluation tool.

When a multiphase body is observed in a scanning electron microscope, the x-rays collected produce an EDX spectrum that quantitatively define the atomic fraction of each element. If different elements are associated with different phases, the content of each phase within the area scanned can be determined. At low magnifications, the EDX spectrum defines the fraction of each phase within the large body. With reasonable counting periods, the standard deviation for different areas examined at low magnifications is low (usually $< 3\%$) and associated with counting statistics. At very high magnifications, the area examined may not be representative of the large body, e.g., the scanned area may only cover one of the many phases, and the deviation of the spectrum relative to the large body can be very large. At some intermediate magnification, the standard deviation will begin to depart from that produced by counting statistics. At this magnification, the area scanned is statistically identical (within an acceptable standard deviation somewhat larger than

^{**} Both Al₂O₃ and ZrO₂ can be dispersed at pH = 2, and are colloidally compatible when mixed together, i.e., they remain dispersed. Both can be flocced at pH = 8.

that due to counting statistics) to the large body. The size of this area thus defines the smallest area that contains the same phase distribution as the whole body. This area (A_U) can be defined quantitatively and used to represent phase uniformity. The better the mixing, the smaller A_U . A_U is an extrinsic property of the multiphase material that depends on processing.

Values of A_U can be related to different mixing methods and mixing periods, e.g. different resident periods for mixed slurries within a high shear rate field, and to the properties of the mixed slurry itself. Lange and Miller¹⁶ have shown that A_U can be related to the viscosity of flocced, two phase slurries and have suggested that an inline viscosity measurement could be used to determine phase uniformity (defined by a number, i.e. A_U) during processing.

Consolidation From the Slurry State

Once colloidally treated, powders should not be dried. Drying produces agglomerates. Slurries contain soluble salts, produced, e.g., by a reaction with the powder itself, which can bond touching particles when the last bit of liquid evaporates from their pendular ring. Drying also reexposes the particles to uncontrolled environments which can reintroduce inclusions. Colloidally treated slurries could be piped directly to a consolidation machine.

How can powder compacts be formed from slurries? Two conventional slurry consolidation methods, slip casting and tape casting, can be directly used with colloidally prepared powders, and with some innovative changes, injection molding could be adapted to do the same. Each of these conventional forming methods are limited, e.g., slip casting best produces thin walled bodies and a large amount of polymer must be removed after injection molding. For these reasons, investigators are exploring alternative slurry shaping methods where either the solid/liquid ratio remains constant during shaping, i.e., slurry molding, or the particles are partially partitioned from the liquid during shaping, e.g. pressure filtration.

To avoid excessive shrinkage during fluid removable and/or densification, molding methods require slurries containing the highest possible fraction of particles. Molding also requires flow. As recently detailed by Aksay and students¹⁷, pourable ceramic slurries containing in excess of 60 volume percent of particulates require highly repulsive interparticle forces. In addition they¹⁸ have also shown that the volume fraction of particulates can be further increased with of the proper particulate size distribution. As shown in Fig. 5, adding a given fraction of finer particulates decreases the slurry viscosity.

Once molded, the rheological properties of the slurry must be dramatically altered

to allow shape retention during unmolding. This change can be induced by a variety of different phenomena that include: freezing (used in injection molding), gelation ¹⁹ and in-situ flocculation. Each can change a flowable slurry into a firm body without fluid phase removal. Rheological changes are not without problems; they can produce strain gradients. For example, volume changes can accompany freezing, and freezing initiates at the surface. In addition, if capillary pressure arises during fluid removal, bodies molded with dispersed slurries will shrink unless an attractive, touching particle network is formed first (e.g., by in-situ flocculation). Shrinkage and expansion gradients can lead to significant stresses and/or disruptive phenomena. The potential problem of mass and phase segregation produced by sedimentation within a highly filled, moldable dispersed slurry has not been addressed.

Moldable slurries can also be achieved when flocced bodies are rapidly sheared. Forces produced by differential acceleration break apart the attractive particle network to produce Newtonian rheology; the network reforms shortly after the shear field is removed. Firm, fully saturated bodies containing between 50 to 60 volume percent particulates can be produced by either centrifuging ¹⁴ or pressure filtering ²⁰ lower viscosity, flocced slurries. When these firm bodies are coupled to high intensity ultrasound, they fluidize to fill a cavity. Once the ultrasound is turned off, the rheology of the slurry quickly reverts to a firm, molded body. The author's experience with this innovative molding method suggests that attenuation of the ultrasound is one problem that must be addressed.

Pressure filtration produces a fully saturated powder compact as particles within a slurry are partitioned as liquid flows through a filter leaving particles behind to form a consolidated layer. Hard ferrite particles within a slurry can be aligned with a magnetic field prior to consolidation. Pressure filtration is used to form ceramic magnets with a variety of applications because the desired, permanent magnetic field is produced during consolidation. ²¹ With the development of moldable casting dies made of a porous plastic material, an innovative pressure filtration machine has recently been introduced ²² that enables the rapid production of large, relatively complex shaped bodies. Although these new filter presses are currently marketed to produce functional articles (plates to sinks) with traditional clay based slurries, they represent the first generation of machines to form advanced components with advanced ceramics. It has also been demonstrated that pressure filtration can also be carried out under conditions of isopressure ²⁰ which decreases the probability of disruptive phenomena occurring by die constraint during pressure release. In addition, with innovative design, pressure filtration offers the advantage that after consolidation, much of the liquid can be removed with a high-pressure gas i.e., through invasion percolation, before the body is removed from the molding die.

The kinetics of pressure filtration obeys Darcy's differential equation²³ for fluid flow through porous media, which when integrated with the appropriate boundary conditions shows that the thickness of the consolidated layer (h) formed under constant pressure (P) is parabolically related to time (t):

$$t = h^2 \frac{u}{2kP} \left(\frac{v_1 - v_0}{v_0} \right), \quad (1)$$

where u is the fluid viscosity; v_0 and v_1 are, respectively, the volume fractions of particulates within the slurry and consolidated layer. The permeability, k , is inversely related to the resistance of fluid flow through the consolidated layer. Assuming the particles are identical spheres with diameter d , one can estimate the permeability of a consolidated layer with the Kozeny-Carman relation which models the layer as a bundle of tortuous capillary tubes with hydraulic diameters resembling slits²⁴:

$$k = \frac{d^2 (1 - v_1)^3}{36 c v_1^2}, \quad (2)$$

where the Kozeny constant, c , defines the shape and tortuosity of the flow channels; $c = 5$ for many systems.

The mechanics of particle packing during filtration and the mechanics of pressure filtered bodies have been recently been examined for aqueous slurries containing Al_2O_3 powder with a mean diameter of approximately $0.6 \mu m$ ²⁰. The electrostatic method (pH control) was used to produce either dispersed or flocced slurries. Figure 6 shows the relative density of consolidated bodies after filtration is complete as plotted against the log of the applied pressure. Consistent with observations by Fennelly and Reed,²⁵ the highest packing density is achieved with dispersed slurries. Also, the packing density achieved with dispersed slurries is pressure independent for pressures > 0.5 MPa. Figure 6 also shows that the packing of consolidated layers from flocced slurries is very pressure sensitive and appears to obey a consolidation law (relative density linearly related to log pressure) similar to dry powders⁴.

The mechanics of particle packing during pressure filtration can be explained with the aid of Fig. 7, which schematically describes the pressure distribution within the filtration system. Assuming the particles have not formed a continuous network (case of dispersed slurry), the slurry pressure is identical to the fluid pressure and

equal to the pressure (P_a) exerted by the plunger. Ambient, atmospheric pressure (P_o) exists on the external side of the filter. The differential pressure across the filter and consolidated layer ($P_a - P_o$) is the driving force for fluid flow. A gradient in fluid pressure exist across the consolidated layer, i.e., at the slurry/layer interface $P_f = P_a$, and neglecting the pressure gradient across the filter, $P_f = P_o$ at the filter/layer interface. Since the total pressure within the consolidated layer must be equal to the applied pressure, the particle network must support a pressure gradient equal but opposite to the fluid pressure. That is, at the filter/layer interface the network pressure, $P_n = P_a$ and at the slurry/layer interface $P_n = 0$. Since network pressure will produce particle rearrangement, during filtration the packing density will be greatest at the filter/layer interface and decrease to the layer/slurry interface. Once the plunger meets the consolidation layer, filtration will continue until the differential fluid pressure dissipates, i.e., the fluid pressure decreases to ambient pressure. During this period, the gradient in the network pressure dissipates to the applied pressure to produce a uniform particle packing density across the consolidation layer.

With this information and that presented in Fig. 6 it can be seen that during pressure filtration, flocced slurries produce large gradients in packing density relative to dispersed slurries. For this case, there is no clear demarcation between the slurry and the consolidated layer as there is for dispersed slurries.

The mechanics of particle packing have only been addressed with static models ²⁶, which does not address particle rearrangement. Why dispersed slurries produce high packing densities at very low pressures has not yet been detailed, but must be related to the effect of repulsive interparticle forces on rearrangement.

It is rarely recognized in ceramic technology that powders exhibit non-linear elastic stress-strain behavior similar to that described by Hertz ²⁷ for two spheres pressed together. As recently detailed by Walton ²⁸, the compressive stress-strain response of a powder can be expressed as $\sigma = A \epsilon^{3/2}$, where A depends on the relative density of the powder compact (average number of contacts per particle) and the elastic properties of the particles. A is independent of particle size. Figure 8a describes this response for Al_2O_3 powder compacts as determined with strain recovery measurements after pressure filtration of both flocced and dispersed slurries. ²⁰ As illustrated, relatively small stresses produce large strains and the compact becomes stiffer as the stress is increased. It is not the porosity that produces this behavior, but the large displacements between particle centers when a 'point' contact is elastically compressed into an area contact. Thus, after a powder has been consolidated and the pressure is released, large elastic strains are recovered and the compact grows.

The greater the consolidation pressure, the greater the recoverable strain. Inclusions within the powder which are either stiffer (e.g. dense agglomerates, whiskers or fibers) or more compliant (organic inclusions) will store less or more strain relative to the powder compact, respectively, during consolidation. Figure 8a also illustrates the elastic response of a dense Al_2O_3 inclusion ($E = 400$ GPa) and a very compliant polymer inclusion ($E = 1$ GPa). The differential strain relieved by the inclusion relative to the powder will produce detrimental stresses during strain recovery. Likewise, the powder compact can be damaged by metal die cavities which constrain the strain recovery of powders pressed within them.

For consolidated dry powders, strain recovery is nearly instantaneous with pressure release. As shown in Fig. 8b, the strain recovery for compacts produced by pressure filtration is time dependent²⁰, e.g., a compact produced from a flocced slurry will continue to release strain and grow many hours after pressure release. This time dependent strain release phenomenon arises because fluid (liquid or air) must flow back into the compact to allow the compressed particle network to grow and relieve its stored strain. Release of the applied pressure will cause the fluid within the compact to share the stored network strain and thus place the fluid in tension. Fluid flow after pressure release is driven by the negative fluid pressure within the compact relative to the ambient pressure outside the compact. Since fluid must flow from the surface to the interior, the strain within the compact is not uniformly released, i.e. strain is first released from the surface of the body.

In practice, strain is likely to be relieved first at one region on the surface. The growth of this region during strain release will be constrained by the rest of the body and it will produce tensile stresses like an inclusion. These tensile stresses can produce radial cracks. Cracks are more frequently observed at higher filtration pressures where more stored strain is released. As detailed elsewhere²⁰, cracking after pressure filtration can be avoided by increasing the compact's resistance to crack growth, e.g., by adding small amounts (< 2 w/o) of certain polymers to the slurry which apparently bonds the particles together as they form the consolidated layer during pressure filtration.

Figure 8b also illustrates that bodies formed with dispersed slurries relieve their stored strain within a much shorter period relative to bodies formed with flocced slurries. The reason for this is that the body formed with the dispersed slurry is still a fluid after pressure filtration, albeit, with a higher viscosity relative to the initial slurry. That is, the consolidated body can flow itself to release stored strain after filtration. Bodies formed with dispersed slurries will continue to flow after removal from their die cavity much like 'silly putty' which has similar dilatant rheology.

Pressure filtration is not the only method to fractionate particles from slurries to form a shape. Centrifugation of flocced slurries can accomplish the same task and avoids the mass segregation produced by centrifuging dispersed slurries¹⁴. Although not as well developed as pressure filtration, with innovative design, centrifugation offers great potential in shaping colloiddally prepared powders.

Densification

Powder compacts are densified at temperatures where mass transport eliminates the void phase. Mass transport is driven by the excess free energy associated with the surface area of the powder. The difference in surface curvature where the particles touch (net negative curvature) relative to the rest of the particle's surface (positive curvature) causes mass to 'fill' the contact region between touching particles. This process is known as sintering. If mass is removed from between particle centers, mass transport will lead to shrinkage and densification. If the particles are crystals, a grain boundary forms and grows as sintering proceeds. In considering the free energy change of a powder compact, the increased energy associated with growing grain boundaries must be taken into account as well as the decrease in particle surface energy. With this thermodynamic consideration, one can shown²⁹ that sintering will stop, i.e. mass transport to form a neck between touching particles terminates, when

$$-dA_s/dA_b = \gamma_b/\gamma_s , \quad (3)$$

where dA_s is the change in surface area, dA_b is the change in grain boundary area, and γ_b and γ_s are the energy per area associated with grain boundaries and particle surfaces, respectively.

When a linear array of touching particles sinter together, they form an equilibrium configuration which satisfies eq. (3). If mass is removed from between particle centers, the shrinkage of the linear array can be predicted with knowledge of γ_b/γ_s . Although the linear array can be used to estimate shrinkage during sintering, it does not enclose and define a void space and thus can not be used to fully understand and predict the disappearance of pores within powder compacts.

The void space within a powder compact can be divided into entities called pores which are defined by irregular polyhedra of touching particles connected to one another to form the particle network.³⁰ Each polyhedron contains one pore. The number of touching particles surrounding and defining a particular pore (equivalent to the number of vertices) is called the pore's coordination number, n . The question that now arises is: can sintering eliminate each and every pore defined by the connective network of different polyhedra?

To answer this question Kellet and Lange²⁹ used eq (3) to analytically determine the sintered, equilibrium configuration of different regular polyhedra formed with identical, touching spherical particles. It was shown that pores within all polyhedra shrink (decrease their volume) during sintering, but only pores with a coordination number less than a critical value ($n \leq n_c$) disappear. Pores with $n > n_c$ shrink to an equilibrium size. The critical coordination number is related to the ratio, γ_b/γ_s ²⁹; the greater γ_b/γ_s , the greater n_c . It was therefore concluded all pores within a powder compact will shrink during sintering, but not all would disappear, i.e., sintering alone may not result in full densification.

The sintered network of touching ZrO₂ spherical particles developed by heating at 1300 °C for 10 hrs is shown in Fig 9a. Note in Fig. 9b and 9c that when the same area is view after a subsequent heat treatment at 1300 °C for 18 hrs and 1400 °C for 4 hrs, respectively, the particle network appears self similar. Differences between the micrographs can be seen. First, smaller particles (or grains) have either become smaller or disappear, while larger particles become larger, i.e., coarsening has occurred. Second, groups of grains rearranged relative to others. Third, measurements show that some shrinkage, i.e., densification occurred. And fourth, very few new contacts are made. The more comprehensive study³¹ from which these micrographs are taken show that once the initial touching particles sinter together to form a metastable network, further densification is related to grain coarsening which continuously alters the network configuration.

Although mass transport to the contact region may stop when eq. (3) is satisfied, adjacent sintered grains will have different radii of curvature that will drive interparticle mass transport. Interparticle mass transport will cause coarsening, i.e., smaller grains disappear as larger grains grow. It can be shown that the decrease in free energy for interparticle mass transport is much smaller than the decrease associated with transport to the contact region. That is, the differential curvature between two particles is much smaller than the differential between particles and their contact region. In addition, during coarsening, the grains become larger. Larger grains result in larger radii and a lower driving force for interparticle mass transport. Thus, one might expect the kinetics for interparticle mass transport leading to coarsening (grain growth) will be slower than the transport to the contact regions (sintering).

If we argue that rapid transport to the contact region leads to shrinkage by sintering and the development of an metastable network similar to that shown in Fig. 9a, and further shrinkage is controlled by slower interparticle transport, then the kinetics of densification should be separated by two regimes: an initial regime controlled by sintering kinetics and a subsequent regime controlled by coarsening kinetics. Since

the sintering regime results in shrinkage to a metastable network with a given relative density, further densification must be controlled by coarsening kinetics. Thus, the two regimes will be separated by the relative density of the metastable network produced by sintering.

Figure 10 shows the shrinkage strain rate determined when different specimens cut from a single powder compact of Al_2O_3 where heated to 1550°C at different heating rates.³² In each case, the shrinkage strain rate increases to a maximum and then decreases. The maximum shrinkage strain rate corresponds to the inflection in relative density vs temperature curves commonly obtained in densification experiments. For each curve, the maximum shrinkage strain rate occurs at the same relative density of 0.77. These data strongly suggest that sintering kinetics dominate up to a relative density of 0.77 where coarsening kinetics dominate during further densification.

The question of how coarsening phenomena is related to the thermodynamics of pore stability can be viewed in two different but complimentary ways. First, it can be seen that coarsening will decrease the coordination number of stable pores, i.e., convert a stable pore with $n > n_c$ to an unstable pore with $n \leq n_c$. With this view, Kellett and Lange³³ have shown that isolated pores produced in a powder compact when polymer spheres pyrolyze during heating will only disappear when grain growth decreases their coordination number below a critical value.

Second, the relation between coarsening, configurational changes in the network during coarsening, and shrinkage can be obtained by examining what happens when grains disappear within a sintered network. Figure 11 a illustrates three truncated, spherical particles taken from a network which has shrunk to a metastable configuration by sintering. The dihedral angle φ_e defines the equilibrium between the surface and grain boundary energies which will be achieved when eq (3) is satisfied, viz. $2\cos(\varphi_e/2) = \gamma_b/\gamma_s$. As coarsening proceeds, the smaller grain becomes smaller and there neighboring grains become larger while φ_e is maintained wherever the grain boundary intersects the surface. At some point during coarsening, the neighboring grains touch one another as illustrated in Fig. 11c. It can be shown³⁴ that when the neighboring grains touch, the angle formed with the surface tangents and the new grain boundary is less than φ_e . Since $\varphi < \varphi_e$, mass transport to the contact region, i.e., sintering, will reinitiate. Contrary to intuition, it can also be shown³⁴ that very little shrinkage occurs as the smaller particle disappears, i.e., for pertanant values of γ_b/γ_s , the larger particles grow at the same rate the smaller one shrinks. Once the larger particles touch one another, shrinkage occurs by the reinitiation of sintering until a new metastable configuration develops that satisfied eq (3) as shown in Fig 11d. Thus, although

most of the mass transport period is consumed by coarsening, coarsening reinitiates sintering and shrinkage. At the same time coarsening decreases the pore coordination number.

The amount of grain growth (coarsening) required to fully densify a powder compact after the initial stage of sintering depends on the coordination number distribution of pores within the compact. Compacts where all pores have $n \leq n_c$ require no grain growth; for this case, all pores disappear during the initial stage of sintering. A predictive relation between grain growth, relative density and pore coordination number distribution does exist³⁴ and mimics the experimental relation reported by Gupta for a variety of different powder compacts³⁵.

It can also be imagined that a major role of applied pressure during densification (hot-pressing, hot-gas-isopressing) is to deform the sintering network to form new particle contacts which are infrequently formed during pressureless sintering. Forming new particle contacts via deformation decreases the need for coarsening.

The above discussion illustrated how particle packing influences both the thermodynamics and kinetics of densification. The ultimate objective is to form a powder compact where all pores are defined by $n \leq n_c$. Methods for achieving this packing arrangement are still controversial. The periodic packing of identical particles have been suggested as one means to achieve this objective³⁶. Unfortunately, it appears that periodic packing is limited to small domains which produces a granular periodic packing arrangement much like the granular microstructure of polycrystals. Figure 12 illustrates the problem that can arise when such a periodic, granular arrangement is heat treated, viz., crack-like voids open at domain boundaries. For this reason, some investigators have shifted their attention to find particle size distributions that produce high packing densities with disordered arrangements which minimize the volume of pores with $n > n_c$.

Today, one must live with and use commercial powders. Using the colloidal approach, such powders can be fractionated to achieve desired particles size distributions which maximize packing density when one of the colloidal compatible consolidation methods is employed. Although the ultimate goal may not be economically achieved with these powders (all pores with $n \leq n_c$) a secondary goal should be pursued: powder compacts with a uniform, narrow distribution of pore coordination numbers such that the pores that disappear last during the coarsening stage are as closely spaced as possible. This goal does not necessarily required high packing density, but does require packing uniformity. One pore with a very large coordination number will not only require extensive grain growth to satisfy its thermodynamics for instability, but its disappearance will also be kinetically limited once it is unstable.

Control of Grain Growth

The last section concluded that some grain growth via coarsening is required to fully densify a powder compact. Although much of this coarsening takes place by the disappearance and growth of adjacent grains through intergranular mass transport, grain boundaries can also move as they would in a fully dense body before full density is achieved. Because matter need only diffuse over atomic distances, grain boundary motion will lead to more rapid grain growth than the coarsening phenomenon. Grain boundary motion will also trap unstable pores within grains before they have the opportunity to disappear via grain boundary diffusion. In addition, if a nearly dense body is left at the densification temperature for a short period, grains in many ceramics can grow more than an order magnitude larger than the average particle size used to form the powder compact. Some grains in ceramics with non-cubic crystalline structures can grow to an enormous size relative to their surrounding grains. Although the reasons for abnormal grain growth are still unclear, abnormally large grains can be a dominant, strength degrading flaw population in many important ceramics. For these and other reasons, grain growth via boundary motion must be controlled both to optimize density and properties.

Second phase inclusions have become increasingly important in controlling grain size in ceramics. Inclusions generally give rise to residual stresses due to differential thermal contraction and therefore are usually thought of as strength degrading flaw populations themselves. But, it has been shown both through experiments³⁷ and theory³⁸ that if the inclusions are less than a critical size, their residual stress will not induce microcracking either during cooling from the densification temperature or during subsequent stressing. Inclusions with a size that will not induce microcracking can be used to both control grain growth and engineer new composites for desired properties without the fear of degrading strength. For example, large and/or abnormal grain growth can be prevented with the addition of an appropriate inclusion phase as demonstrated by the dramatic strengthening achieved with additions of SiC to Al₂O₃³⁹, ZrO₂ to β' -Al₂O₃⁴⁰, and Al₂O₃ to cubic ZrO₂⁴¹. In each of these cases, the inclusions eliminate the most detrimental flaw population, viz., large and/or abnormal grains.

For ceramics, inclusions used to control grain size can be introduced by mixing two-phase powders, e.g., via the colloidal approach. Namely, the inclusions must be effective in retarding grain growth before the powder compact achieves a relative density > 0.9, where rapid grain growth is commonly observed in single-phase materials³⁵.

Grains are classified by their size (volume) and polyhedron type, defined by the number of faces ⁴². As grains decrease their volume, they progressively and sequentially decrease their number of faces. During grain growth the number of grains per unit volume decreases, i.e. some grains decrease their volume and disappear. Only tetrahedral-shaped grains disappear. Thus, in modeling the effect of perturbations on grain growth, one need only to model the shrinkage and disappearance of simply shaped, tetrahedral grains. The tetrahedral grain decreases its free energy as it decreases its volume. (Grains with many more faces (>14) will decrease their free energy by growing.) The derivative of the free energy with respect to the grain's volume (the Laplace equation) is proportional to the grain boundary energy per unit area (γ_g) and inversely proportional to the radius of curvature (r) of its grain boundaries, viz. $dE/dV = 2\gamma_g/r$. dE/dV has the dimensions of stress and is referred to as the driving stress, σ_d , to decrease the volume of a grain. For the tetrahedral grain, the radius of curvature is positive (grain boundaries are concave when looking from within), and $r \approx 0.6 D_t$, where D_t is the diameter (grain size) of the equivalent spherical volume of the tetrahedron. Thus, for the tetrahedron, $\sigma_d = 3.3\gamma_g/D_t$.

Zener ⁴³ was the first to explain how inclusions retard grain growth. Zener's concept can be visualized with the aid of Fig. 13 a, which shows, in two dimensions, how a shrinking tetrahedral grain interacts with spherical inclusions of radius, R . ⁴⁴ As the shrinking grain encounters the inclusion, an increasing proportion of boundary area is removed from the grain. When N inclusions are simultaneously intersected, the maximum amount of grain boundary area removed is $N\pi R^2$, which corresponds to a decrease in free energy of $N\pi R^2\gamma_b$. If the grain shrinks further, the grain boundary area adjacent to the inclusions must bow out as it attempts to break away. This bowing and the fact that the grain boundary regains its area occupied by the inclusion during bowing causes the free energy of the system to increase. Using line tension arguments, Zener showed that as the grain boundary breaks away, the inclusions exert a maximum restraining 'stress', $\sigma_r = 0.75f\gamma_b/R$, where f is the volume fraction of inclusions. Thus the net driving 'stress' for the grain boundaries of a tetrahedral grain to breakaway from the inclusions is

$$\sigma_n = \sigma_d - \sigma_r = \gamma_b \left(\frac{3.3}{D_t} - \frac{0.75f}{R} \right) \quad (5)$$

If it is assumed that the kinetics of grain disappearance (growth) are proportional to σ_n , then eq (5) shows that inclusions will reduce the kinetics for grain growth.

The free energy vs volume function for inclusion encounter and break-away is

schematically shown in Fig. 13b for the cases where $\sigma_n > 0$, 0 , and < 0 . The latter case ($\sigma_n < 0$) represents the condition ($f > 4.4 R/D_t$) where the tetrahedral grain is trapped within a potential well and will not decrease its volume unless thermally activated to 'jumb out'.⁴⁴

Zener's concept and equation (5) lays down rules in using inclusions to hinder grain growth. First, the inclusion must be smaller than the grains. Recent experiments indicate that even when f is large, inclusions will have no effect on grain growth until their mean grain size is > 1.5 times the inclusion size⁴⁵. Second, the smaller the inclusion size the greater the hindrance to grain growth at a given volume fraction. And, third, larger volume fractions will produce greater hindrance. These rules appear to be obeyed for ceramics when the inclusions are immobile as assumed by the analysis^{45,46}. It is still questionable if inclusions will completely prevent grain growth as suggested for the case where $\sigma_n \ll 0$.

Inclusions can also retard the motion of 3- and 4-grain junctions. But since it costs much less energy for the inclusion to either break away from a 4-grain junction and slip onto a 3-grain junction or break away from a 3-grain junction onto a 2-grain junction (grain boundary) relative to the much greater energy required to break away from a grain boundary and slip into the crystal, inclusions are much more effective in retarding grain growth when they interact with grain boundaries⁴⁴.

The above analysis assumes that the inclusions are spatially fixed, i.e., immobile. If the inclusions exhibit sufficient self diffusion, they can become mobile and can be dragged along by the moving boundaries.⁴⁷ Although mobile inclusions can still be effective in retarding grain growth as Evans⁴⁸ has shown for analogous pore drag, they soon coalesce to become larger and less effective. The kinematics of coalesce can be viewed as follows⁴⁴. Mobile inclusions are first collected by moving grain boundaries. Three grain junctions move together to eliminate grain boundaries and push together inclusions already collected by the disappearing boundary. Finally, 4-grain junctions move together to collect all inclusions on 3-grain junctions to form a new 4-grain junction which contains all collected inclusions. With grain growth, mobile inclusions are relocated to 4-grain junctions, their lowest free energy location. During coalescence, inclusions sinter together and undergo grain growth themselves. As grain growth in the major phase proceeds, coalescence of inclusions at 4-grain junctions will continue and the ratio of inclusion size to grain size will be maintained constant during further grain growth. Immobile inclusions that effectively retard grain growth at lower temperatures can become mobile at higher temperatures where they become much less effective because of coalescence.

Because inclusions are introduced into ceramics by mixing powders, their distribution is a critical processing issue. When the inclusions are not uniformly distributed during powder mixing, grain growth in some regions will be less hindered than others. In the extreme case, e.g., where major phase agglomerates are not removed by colloidal fractionation and inclusions can not be introduced into these agglomerates, the region containing few inclusions will undergo rapid grain growth as shown in Fig. 14. In addition, when very small volume fractions of inclusions are used, their intrinsically poor distribution can exaggerate abnormal grain growth relative to single phase material.⁴⁹ Thus, grain growth controlled with inclusions starts with uniformly prepared powders.

Control of grain growth can also be achieved with minor additions of selected cations which exhibit slight solid-solubility.⁵⁰ It is usually presumed that these 'impurities' will prefer to concentrate at boundaries where they better accommodate the special 'crystal chemistries' of grain boundary structures, i.e., ion size ratio, charge balance, and coordination number. If the grain boundary were to break away from this planer 'cloud of impurities', i.e., boundary motion is more rapid than the diffusion required to keep the impurities moving with the boundary, then the planer 'cloud of impurities' with area A_b will now reside within the grain. Grain boundary break away will increase the free energy by $dG = \Delta G A_b dD_t$, where ΔG is the free energy per unit volume for the 'impurity cloud' residing within the crystal relative to the boundary; dD_t is the change in grain size. The restraining 'stress' for the shrinkage of a tetrahedral grain with $A_b = \alpha D_t^2$ and volume, $V = \beta D_t^3$, is $\sigma_r = dG/dV = (\alpha/3\beta)\Delta G$, where α and β are numerical factors⁵¹. The net driving 'stress' for boundary breakaway during grain shrinkage is given by

$$\sigma_n = \sigma_d - \sigma_r = \frac{3\gamma_b}{D_t} - \frac{\alpha}{3\beta}\Delta G \quad (6)$$

Similar to the case for inclusions, when $\sigma_n > 0$, the 'cloud of impurities' will momentarily hinder grain growth, but boundaries can easily break away. With further grain growth, a grain size will be obtained where $D_t > 10(\alpha/\beta)(\gamma_b/\Delta G)$ and $\sigma_n < 0$. Here, the 'cloud of impurities' will severely restrain grain growth and grain growth might be expected to be limited by the diffusion kinetics of the 'impurity cloud'⁵². Thus, the 'impurities' will have very little effect when the grains are small, but a major effect as the grains grow larger. It is obvious that the greatest effect on grain growth is obtained by choosing 'impurities' that maximize ΔG .

The same reasoning has been applied to the case where phase partitioning is

concurrent with grain growth. It was observed⁵³ that grains of the same structure develop different compositions during partitioning. Grain growth in the two-phase compositional region is severely limited relative to single phase regions, yet second phase grains which might hinder grain growth as discussed above for inclusions are not observed⁵³ as initially postulated.⁵⁴ If compositional differences between grains did not alter during grain growth (i.e., if boundary motion is faster than the period required to equilibrate compositional gradients), it was reasoned that boundary would leave behind a 'ghost' boundary within the growing grain where the lattice parameters change abruptly due to the compositional gradients. If the compositional gradient between the two grains is a step function, then the 'ghost' boundary would appear as a coherent interface. The different lattice parameters on either side of the 'ghost' boundary would produce a strain energy density, $U_{se} = k\varepsilon^2/E$, where ε is the strain due to the change in lattice parameters, E is the material's elastic modulus, and k is a dimensionless constant.⁵³ In the same manner used to develop eq (6), the net driving 'stress' for shrinkage of the tetrahedral grain is given by

$$\sigma_n = \sigma_d - \sigma_r = \frac{3.3}{D_t} \gamma_b - k \frac{\varepsilon^2}{E} . \quad (7)$$

As described for 'impurity clouds', the grain boundary could easily move to form a 'ghost' boundary when D_t is small ($\sigma_n > 0$), whereas as grain growth proceeds, a condition will arise ($D_t > 3.3\gamma_b E / (k\varepsilon^2)$) where grain growth will be limited ($\sigma_n < 0$) by the diffusion kinetics required to equilibrate composition, i.e., grain growth kinetics will be related to partitioning kinetics. In systems that exhibit extended solid-solution, grain growth control will be more pronounced when small compositional differences produce large differences in lattice parameters.

Today, our use of 'impurity clouds' and phase partitioning to control grain growth is one of accidental discovery due to our lack of understanding of how to systematically chose and engineer compositions that utilize and optimize these important phenomena.

Concluding Remarks

The above review of processing science and technology leading to ceramics with increased reliability suggests certain research directions. The concepts leading to the colloidal methodology to fractionate and consolidate powders were developed out of a need to eliminate heterogeneities common to powders that produce unwanted flaw populations in structural ceramics.⁷ Although the fundamental understanding of interparticle forces is relatively mature, relations between

surfactant chemistries and ceramic surface chemistries leading to a predictive choice of surfactants and conditions that optimize and alter interparticle forces consistent with ceramic powder processing is an open research field. Likewise, research leading to a predictive understanding of the slurry rheology as affected by interparticle forces, particulate volume fraction, size, size distribution and mixed phase content will significantly aid new ceramic processing technology. Our understanding of powder consolidation mechanics, viz., how particles rearrange during powder flow under conditions of constrained dilatancy, is non-existent but critical to optimize packing density to optimize densification kinetics. The mechanics of powder compacts themselves, ranging from strain release after consolidation to fracture phenomena, is a research void that must be filled to learn how to consolidate powders from slurries without producing disruptive phenomena. In the past, densification research has emphasized kinetic models of sintering that neglect the effects of particle arrangement. The link between coarsening kinetics and densification kinetics would be one fruitful research topic. Our ability to control grain growth would be greatly enhanced with a fundamental understanding of the effect of impurities on the 'crystal chemistry' of grain boundary structures and how compositional gradients produced by partitioning effect grain boundary motion and partitioning kinetics itself. This research would be directed to increase property reliability via increased processing reliability, i.e., processing reliability equals material reliability.

Acknowledgement

Writing this review and portions of the work concerning control of grain growth was supported by the Air Force Office of Scientific Research, Contract No. AFOSR-87-0291.

References

1. M. V. Swain, "R-Curve Behavior of Magnesia-Partially-Stabilized Zirconia and Its Significance for Thermal Shock," pp 355-70 in Fracture Mechanics of Ceramics, Vol. 5, ed. by R. C. Bradt, A. G. Evans, D. P. H. Hasselman, and F. F. Lange, Plenum (1983).
2. D. B. Marshall and A. G. Evans, "Failure Mechanisms in Ceramic-Fiber/Ceramic-Matrix Composites," *J. Am. Ceram. Soc.* 68 [5] 225-31 (1985).
3. F. F. Lange and M. Metcalf, "Processing-Related Fracture Origins: II. Agglomerate Motion and Crack-Like Internal Surfaces Caused by Differential Sintering," *J. Am. Ceram. Soc.* 66, 398 (1983).
4. R. G. Frey and J. W. Halloran, "Compaction Behavior of Spray-Dried Alumina," *J. Am. Ceram. Soc.* 67 [3] 199-203 (1984).
5. W. H. Rhodes, "Agglomerate and Particle Size Effects on Sintering Yttria-Stabilized Zirconia," *J. Am. Ceram. Soc.* 64 [1] 19 (1981).
6. F. F. Lange, "Sinterability of Agglomerated Powders," *J. Am. Ceram. Soc.* 67, 83 (1984).
7. F. F. Lange, B. I. Davis and E. Wright, "Processing-Related Fracture Origins: IV, Elimination of Voids Produced by Organic Inclusions", *J. Am. Ceram. Soc.* 69[1]66-9 (1986).
8. V. Engle and H. Hubner, "Strength Improvement of Cemented Carbides by Hot Isostatic Pressing," *J. Mater. Sci.*, 13 [9] 2003-13 (1978).
9. B. J. Kellett and F. F. Lange, "Experiments on Pore Closure During Hot Isostatic Pressing and Forging," *J. Am. Ceram. Soc.* 71 [1] 7-12 (1988).
10. F. F. Lange, "Processing-Related Fracture Origins: I. Observations in Sintered and Isostatically Hot-Pressed Al₂O₃/ZrO₂ Composites," *J. Am. Ceram. Soc.* 66, 396 (1983).
11. J. W. Goodwin, "The Rheology of Dispersions," in Colloid Science, Vol. 2, pp. 246-293, D. H. Everett (Senior Reporter), The Chemical Society, London, (1975).
12. M. D. Sacks, "Rheological Science in Ceramic Processing," Science of Ceramic Chemical Processing, pp 522-38, Ed. by L. L. Hench and D. R. Ulrich, John Wiley, New York (1986).

13. J. N. Israelachvili, Intermolecular and Surface Forces, Academic Press, London (1985).
14. F. F. Lange, "Forming a Ceramic by Flocculation and Centrifugal Casting," U.S. Patent 4,624,808, November 25, 1986.
15. F. F. Lange and M. M. Hirlinger, "Phase Distribution Studies Using Energy Dispersive X-Ray Spectral Analysis," *J. Mat. Sci. Let.* 4, 1437-41 (1985).
16. F. F. Lange and K. T. Miller, "A Colloidal Method to Ensure Phase Homogeneity in Beta"-Al₂O₃/ZrO₂ Composite Systems," *J. Am. Ceram. Soc.* 70 [12] 896-900 (1987).
17. J. Cesarano, I. Aksay, and A. Bleier, "Stability of Aqueous alpha-Al₂O₃ Suspensions with poly(methacrylic acid) polyelectrolyte," *J. Am. Ceram. Soc.* (in press-April, 1988).
18. K. P. Darcovich and I. Aksay, "Particle Sized Distribution of Dense Ceramic Suspensions," (to be submitted).
19. R. D. Rivers, "Method of Injection Moulding Powder Metal Parts," U.S. Patent 4,113,480 Sept 12, 1978.
20. F. F. Lange and K. T. Miller, "Pressure Filtration: Kinetics and Mechanics," *Bul. Am. Ceram. Soc.* 66 [10], 1498-1504 (1987).
21. S. Strijbos, "Pressure Filtration of Permanent Magnetic Powders," Proc. Conf. Hard Magnetic Materials, Ed. H. Zijlstra, Publ. Bond voor Materialenkennis, Den Haag, Netherlands (1974); C. A. M. Van den Broek and A. L. Stuijts, "Ferroxdure," *Philps Tech. Rev.* 37 [7] 157-75 (1977).
22. Gebruder Netzsch, Maschinenfabric GmbH & Co., Tech. Inform. Bul. GK 012, D-8672 Selb/Bavaria, FRD (1985).
23. F. M. Tiller and C.-D. Tsai, "Theory of Filtration of Ceramics: I Slip Casting," *J. Am Ceram. Soc.* 69 [12], 882-87 (1986).
24. J. Dodds and M. Leitzement, "The Relation Between the Structure of Packing Particles and Their Properties," pp 56-75, in Physics of Finely Divided Mater., ed by N. Boccara and M. Daoud, Proc. in Physics 5, Springer (1985).
25. T. J. Fennelly and J. S. Reed, "Mechanics of Pressure Casting," *J. Am. Ceram.*

Soc. 55[5] 264-8 (1972).

26. R. A. Davis and H. Deresiewicz, "A Discrete Probabilistic Model for Mechanical Response of a Granular Medium," *Acta Mechanica* 27, 69-89 (1977).

27. S. Timoshenko and J. N. Goodier, Theory of Elasticity, 2nd ed. pp 372-80, McGraw-Hill (1951).

28. K. Walton, "The Effective Elastic Modulus of a Random Packing of Spheres," *J. Mech. Phys. Solids*. 35 [2], 213-26 (1987).

29. B. J. Kellett and F. F. Lange, "Thermodynamic of densification, Part I: Sintering of Simple Particle Arrays, Equilibrium Configurations, Pore Stability, and Shrinkage," *J. Am. Ceram. Soc.* (in review)

30. H. J. Frost, "Overview 17: Cavities in Dense Random Packing," *Acta. Met.* 30 [5] 899-904 (1982).

31. E. B. Slamovich and F. F. Lange, "Electrostatic Route to Micoro-Sized Zironia Spheres from Liquid Precursors," *Better Ceramics Through Chemistry III*, MRS Meeting, April 1988, Proc. to be published.

32. F. F. Lange, to be published.

33. B. J. Kellett and F. F. Lange, "Thermodynamic of densification, Part III: Experimental Relation Between Grain Growth and Pore Closure," *J. Am Ceram. Soc.* (in review)

34. F. F. Lange and B. J. Kellett, "Thermodynamic of densification, Part II: Grain Growth in Porous Compact and Relation to Densification," *J. Am Ceram. Soc.* (in review)

35. T. K. Gupta, "Possible Correlations Between Density and Grain Size During Sintering", *J. Am. Ceram. Soc.* 55 [5], 176 (1972).

36. Barringer, and H. K. Bowen, "Synthesis and Processing of Submicrometer Ceramic Powders," Science of Ceramic Chemical Processing, ed. by L. L. Hench and d. R. Ulrich, pp 482-96, Wiley (1986).

37. D. B. Binns, "Some Physical Properties of Two-Phase Crsytal-Glass Solids," Science of Ceramics, ed. by G. H. Steward, pp. 315-35, Academic Press, New York (1962).

38. D. J. Green, "Microcracking Mechanisms in Ceramics" Fracture Mechanics of Ceramics, ed by R. C. Bradt, A. G. Evans, D. P. H. Hasselman, and F. F. Lange , Vol 5 p 457 Plenum Press (1983).
39. F. F. Lange and Nils Claussen, "Some Processing Requirements for Transformation Toughened Ceramics," Ultrastructure Processing of Ceramics, Glasses and Composites, ed by L. L. Hench and D. R. Ulrich, p 493, John Wiley (1984).
40. D. J. Green, "Transformation Toughening and Grain Size Control in beta"-Al₂O₃/ZrO₂ Composites," J. Mat. Sci. 20 [7] 2639 (1985).
41. F. J. Esper, I. H. Friese, and H. Geier, " Mechanical, Thermal, and Electrical Properties in the System of Stabilized ZrO₂(Y₂O₃)/Al₂O₃," Advances in Ceramics, Vol. 12 Ed by N. Claussen, M. Ruhle, and A. H. Heuer, p528, Am. Ceram. Soc. , Columbus, Ohio (1985).
42. S. K. Kurtz and F M A Carpay, "Microstructure and Normal Grain Growth in Metals and Ceramics: Part I, Theory," J. Appl. Phys. 51 [11], 5725 (1980).
43. C. Zener, kindly quoted by C. S. Smith, Trans. Met. Soc. AIME, 175, 15 (1949).
44. F. F. Lange, "Controlling Grain Growth," Ceramic Microstructures '86: Role of Interfaces, Plenum (in press).
45. F. F. Lange and Margaret M. Hirlinger, "Grain Growth in Two-Phase Ceramics: Al₂O₃ Inclusions in ZrO₂ ," J. Am. Ceram. Soc. 70 [11] 827-30 (1987).
46. D. L. Olgaard and Brian Evans, "Effect of Second-Phase Particles on Grain Growth in Calcite," J. Am. Ceram. Soc. 69 [11] C-272-277 (1986).
47. M. F. Ashby and R. M. A. Centamore, "The Dragging of Small Oxide Particles by Migrating Grain Boundaries in Copper," Acta. Met. 16[9] 1081 (1968).
48. C. H. Hsueh, A. G. Evans, and R. C. Coble, "Microstructural Development During Final/Intermediate Stage Sintering-I: Pore/Grain Boundary Separation," Acta. Met. 30[7] 1269 (1982).
49. F. F. Lange and M. M. Hirlinger, "Hindrance of Grain Growth in Al₂O₃ by ZrO₂ Inclusions," J. Am. Ceram. Soc. 67 [3], 164 (1984).

50. S. J. Bennison and M. P. Harmer, "Grain Growth Kinetics for Alumina in Absence of a Liquid Phase," *J. Am. Ceram. Soc.* 68 [1], C22-24 (1985).
51. P. J. Clemm and J. C. Fisher, "The Influence of Grain Boundaries on the Nucleation of Secondary Phases," *Acta Met.* 3, 70-3 (1955).
52. J. W. Cahn, "Impurity Drag Effect on Grain Boundary Motion," *Acta Metall.* 10 [9], 789-98 (1962).
53. F. F. Lange, D. B. Marshall and J. R. Porter, "Controlling Microstructure Through Phase Partitioning From Metastable Precursors: the ZrO_2 - Y_2O_3 System," Ultrastructure Processing of Ceramics, Glasses and Composites, Ed. by J. D. Mackenzie and D. R. Ulrich, Wiley (in Press).
54. F. F. Lange, "Transformation-Toughened ZrO_2 : Correlations Between Grain Size Control and Composition in the System ZrO_2 - Y_2O_3 ," *J. Am. Ceram. Soc.* 69 [3] 240-2 (1986).

Figure Captions

Fig. 1 Schematic plot of frequency vs potential strength of different flaw populations potentially present in a ceramic material. Frequency distribution and ordering depends on processing method and material characteristics.

Fig 2 One colloidal method for breaking apart weak agglomerates and fractionating desired particles from unwanted hard agglomerates and inclusions. Each powder in a multiphase system is treated the same before mixing.⁷

Fig. 3 Zr/Al count ratio (obtained from an EDX spectra) vs the normalized distance detailing the ZrO₂ and Al₂O₃ distribution for mixed powder slurries centrifuged in the dispersed and flocced states.

Fig. 4 Micrographs of dense, Al₂O₃/ZrO₂ composite ceramic formed by centrifuging a dispersed slurry illustrating particle size and phase distributions at the (a) bottom and (b) top of the specimen.

Fig. 5 Viscosity (extrapolated to zero shear rate) vs. fine fraction for Al₂O₃ (0.55 volume fraction) slurries, dispersed with a polyelectrolyte, containing coarse (0.8 μm) and fine (0.2 μm) powders.¹⁸

Fig. 6 Relative density of different bodies produced from the same Al₂O₃ powder by filtration at different applied pressures. Bodies were consolidated from either dispersed (pH = 2) or flocced (pH = 8) aqueous slurries containing 20 volume % solids.

Fig. 7 Schematic of pressure distribution during pressure filtration showing that a pressure gradient exists within the network of consolidated particles.

Fig. 8 a) Elastic strain recovered after different saturated, Al₂O₃ powder bodies were consolidated from either dispersed or flocced slurries by pressure filtration at different applied pressures. Note that the non-linear stress/strain relation is similar to that expected from Hertzian elastic behavior, viz., $\sigma = A \epsilon^{3/2}$.²⁰ b) Time dependent strain recovered after pressure filtration (80 MPa) of dispersed and flocced Al₂O₃ slurries.²⁰ Note that the recovery period for body formed with the flocced slurry is much longer.

Fig. 9 Micrographs of spherical ZrO₂(+8 mole % Y₂O₃) particles produced by electrostatic atomization of Zr-acetate. a) After sintering by heating to 1300 °C for 10 hrs, b) same area after further heat treatment at 1300 °C, 18 hrs, c) 1400 °C, 4

hrs where self similar network has undergone coarsening and further densification. 31

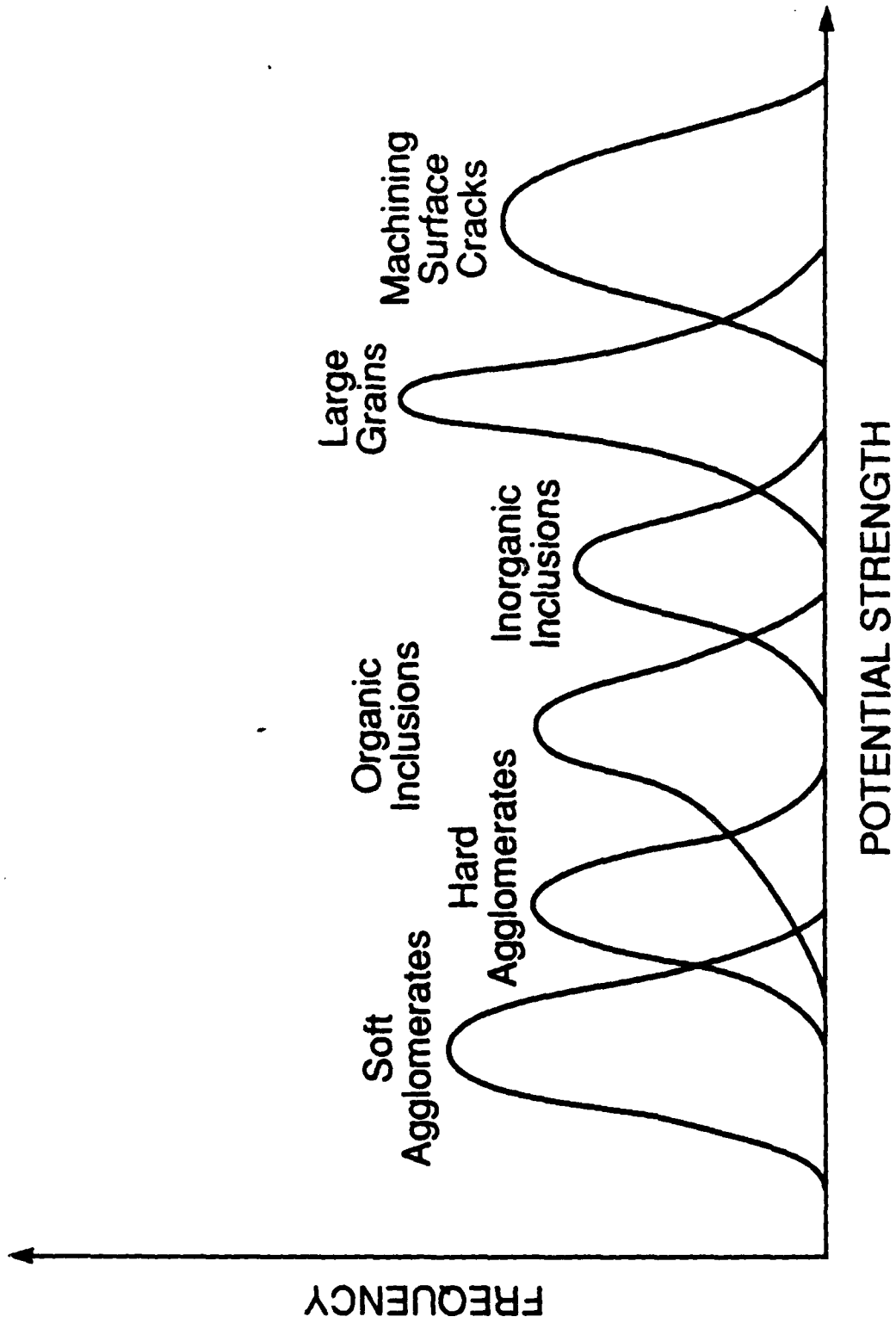
Fig. 10 Shrinkage strain rate vs temperature for identical Al_2O_3 compacts heated to 1550 °C at different heating rates. Maximum strain rate occurred at a relative density of 0.77 for all three specimens.

Fig. 11 Three particles, in two configurations, which (a to b) shrink together by sintering and (b to c) coarsen (center particle shrinks) and then (c to d) sinter again. Note that the configuration development on the right is observed in the upper left of Fig. 9.

Fig. 12 Partial densification of periodically packed, multilayered arrangement of 1 μm polymer spheres. Note opening displacements at domain boundaries.

Fig. 13 Two dimensional schematic of grain boundaries of a tetrahedral grain interacting with spherical inclusions. Different positions illustrate the shape of the boundary as it encounters and breaks away from the inclusions. b) Energy of the tetrahedral grain vs its volume as it encounters and breaks away from inclusions. Three different curves are for three different retarding 'stresses' produced by inclusions.

Fig. 14 Micrograph showing that ZrO_2 inclusions (white phase) could not restrain grain growth within Al_2O_3 agglomerate during densification as in surrounding matrix where phases are well mixed. Note trapped porosity within one larger Al_2O_3 grain.



F 2

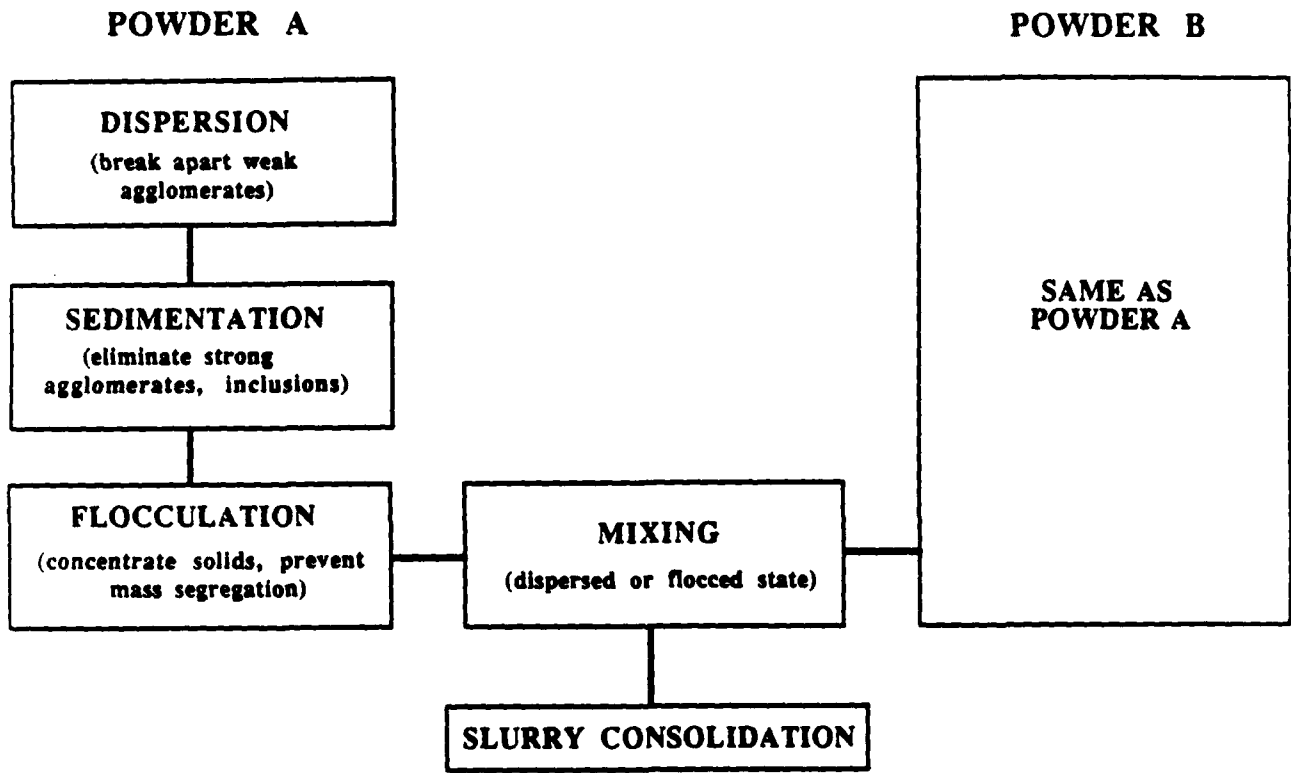
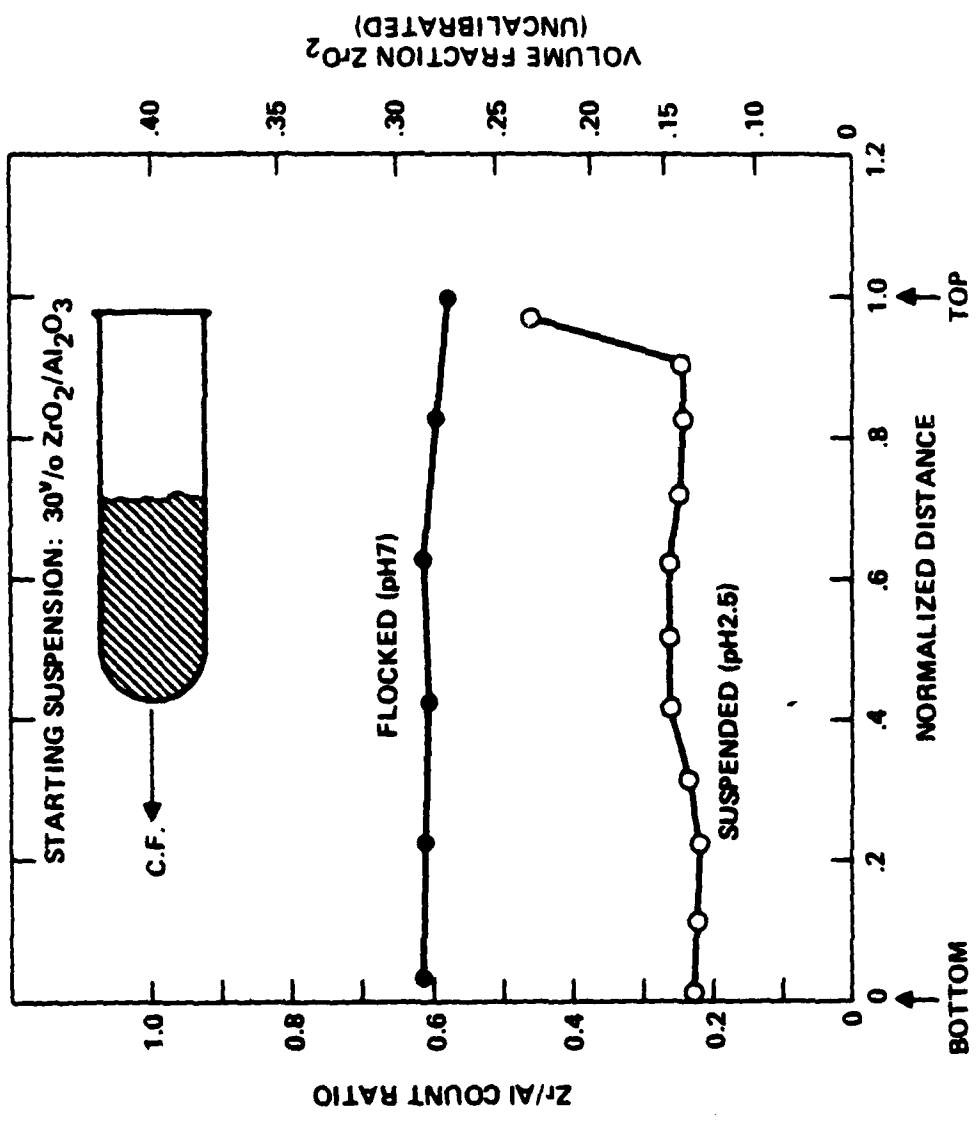
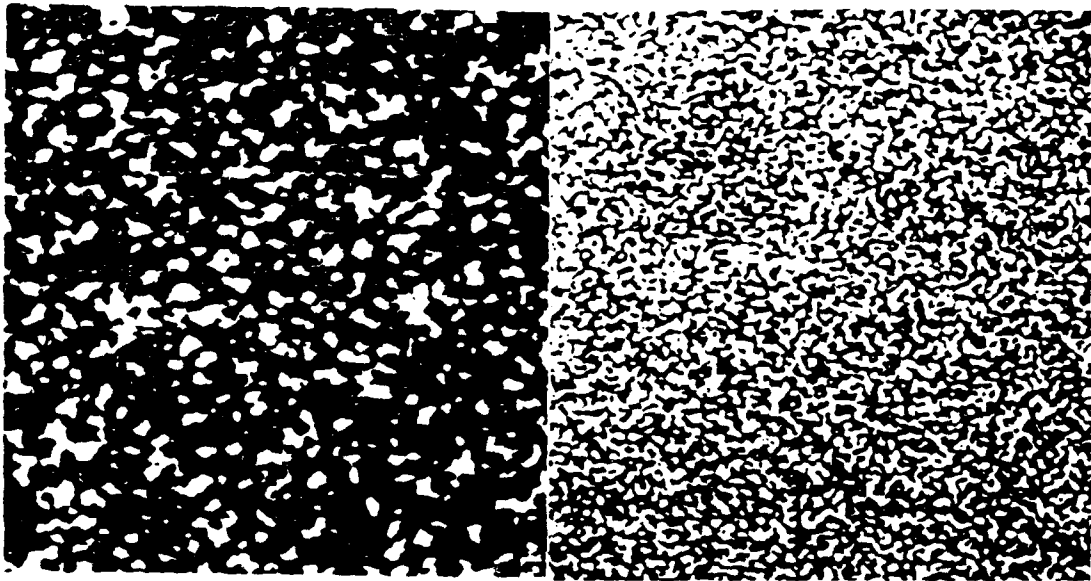


Fig 2, F.F. King



30 30 30

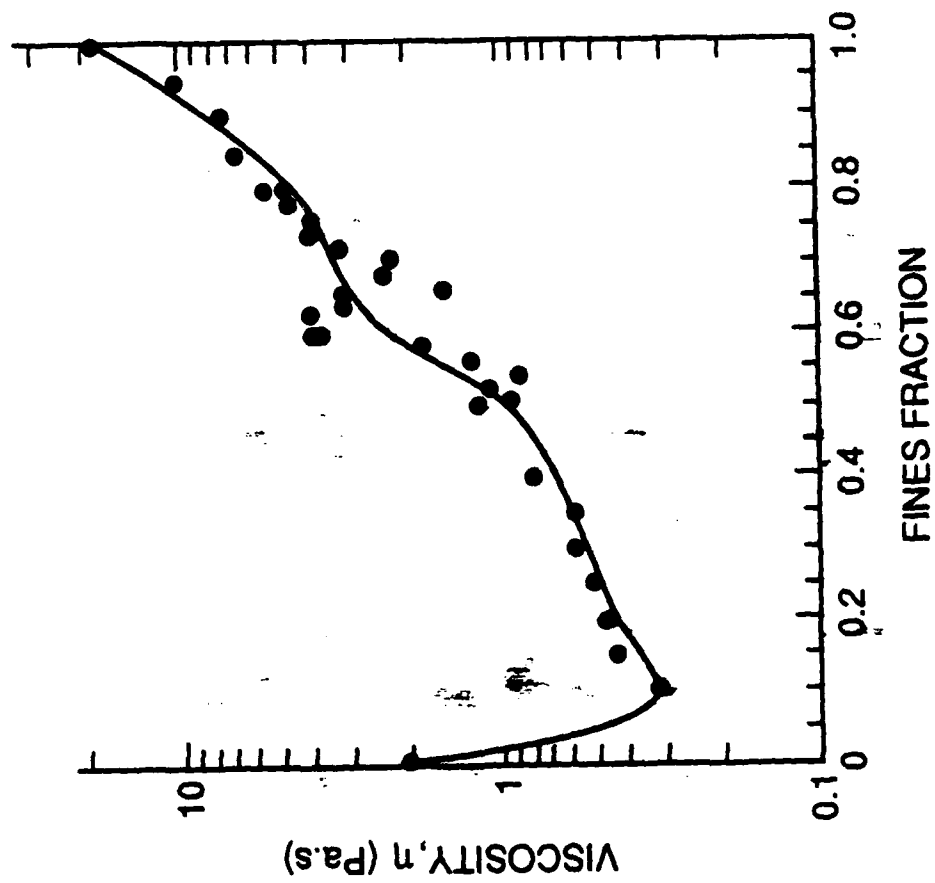


BOTTOM

10µm

TOP

Fig 4. F.F. Lang



0.025 0.05 0.1 0.2 0.5 1 2 5 10

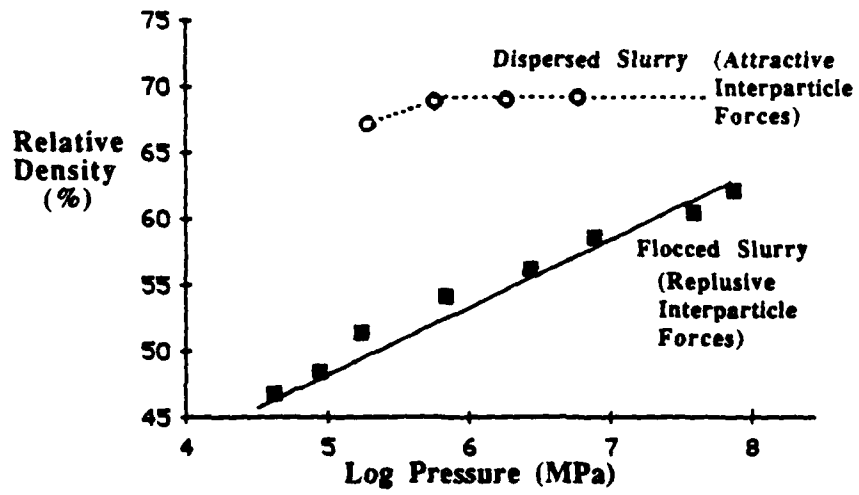


Fig 6, F. Filson, 4

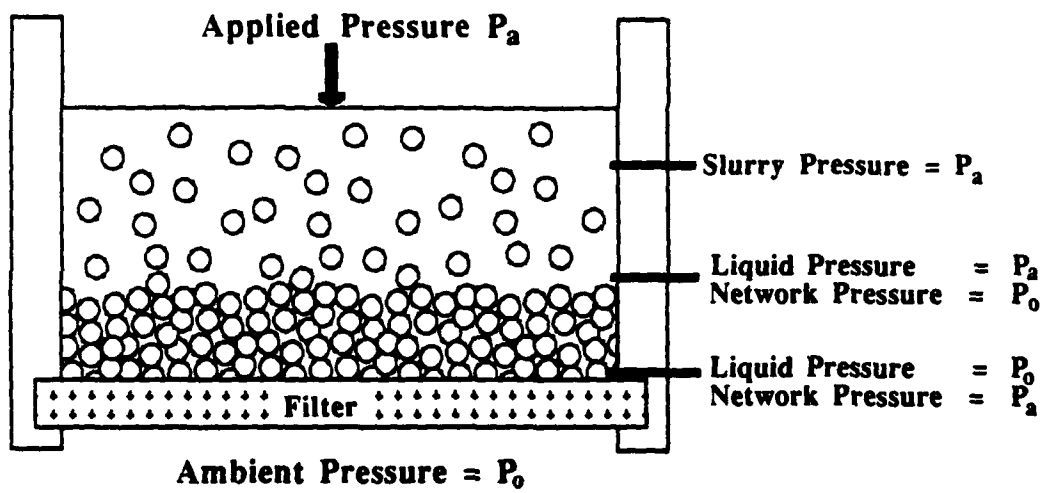


Fig 7 F. Filtration

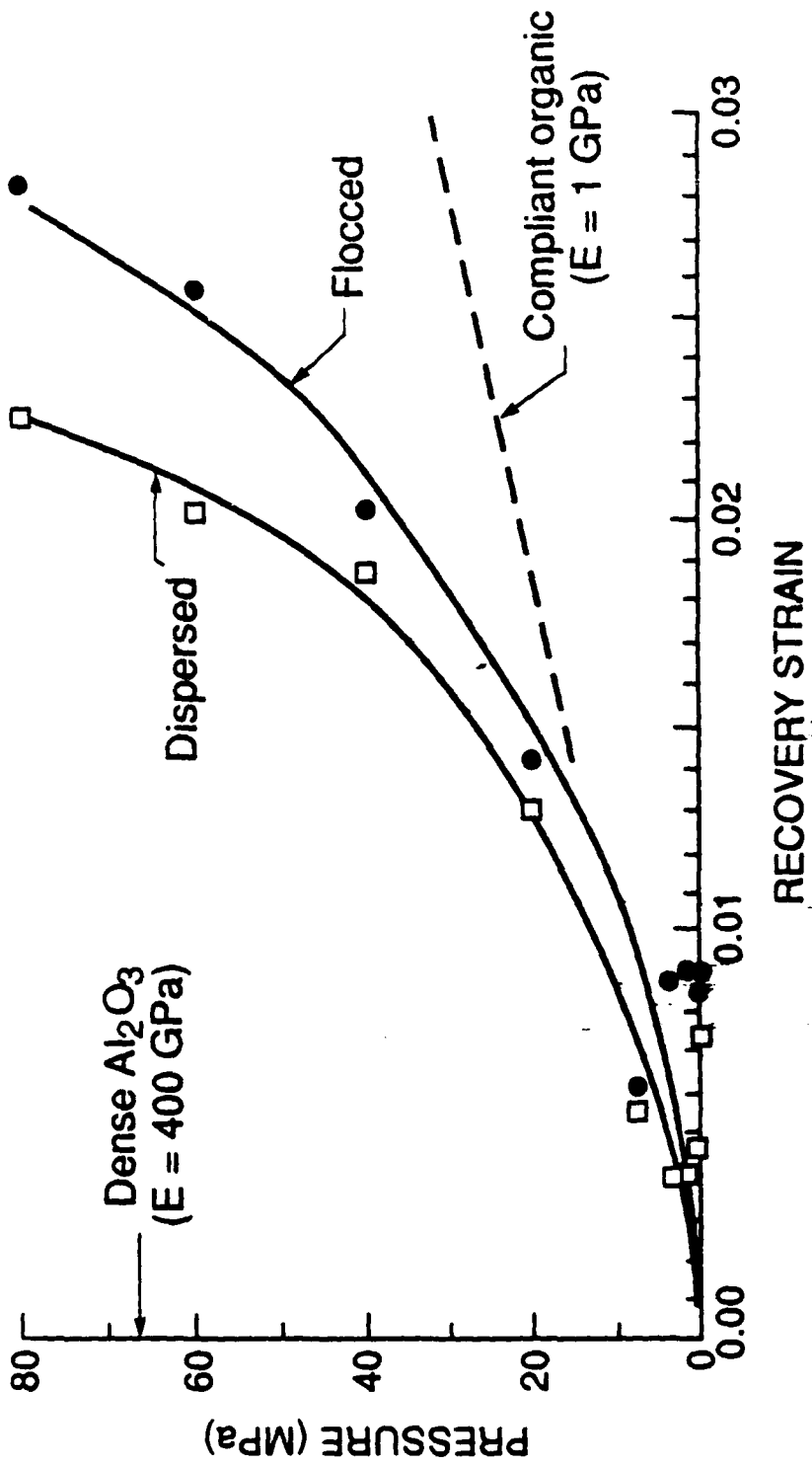


Fig. 2. F. F. ...

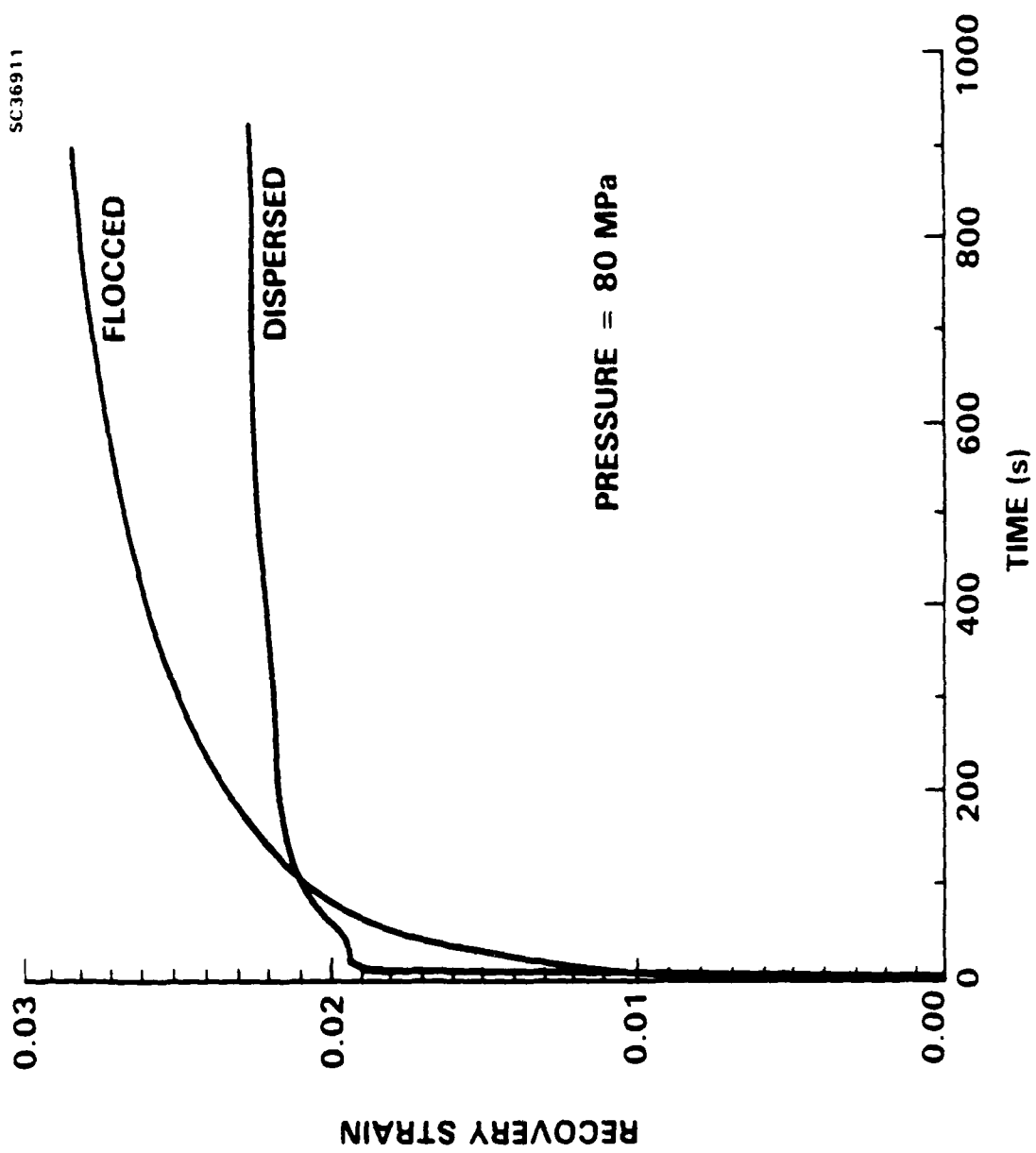


Fig 2b, F Flow

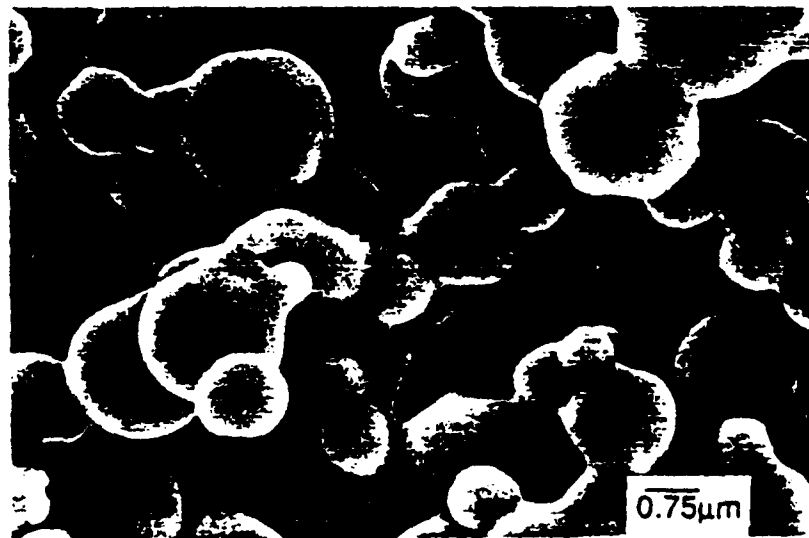
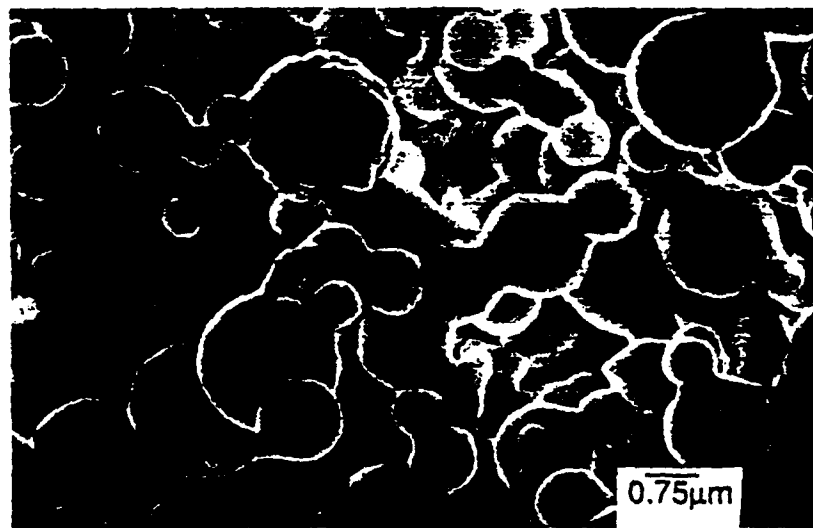
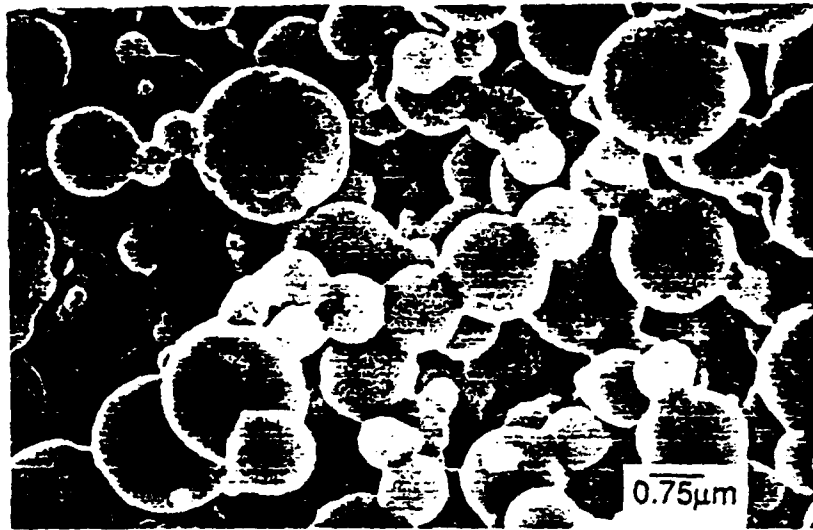


Fig 9
F.Fila

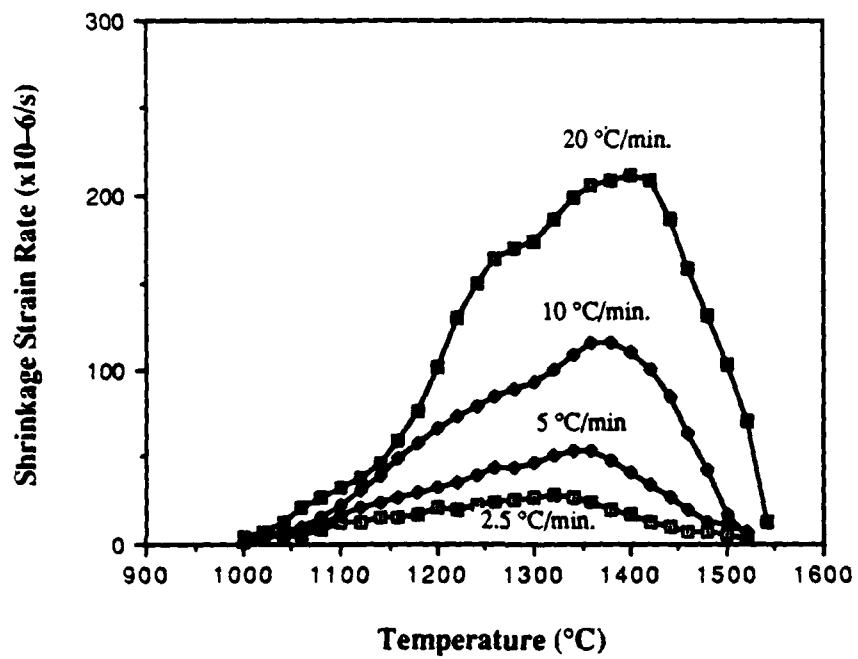


Fig. 10 F.F. 10

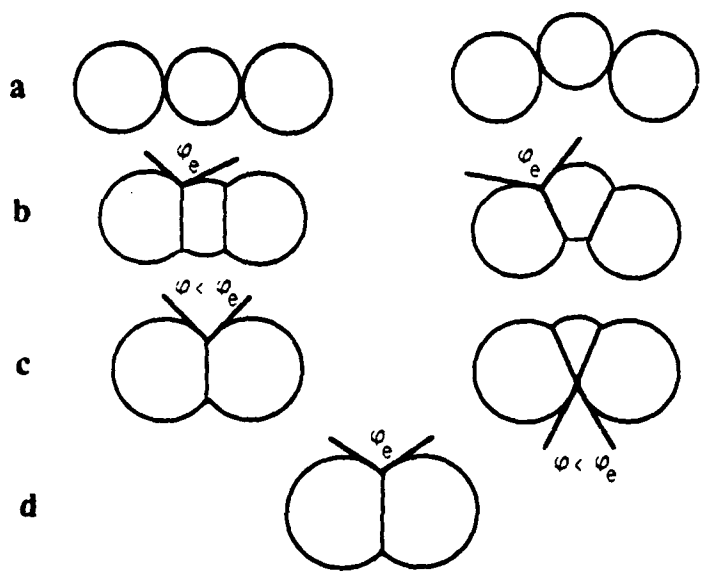


Fig 11, I.F. 12/21

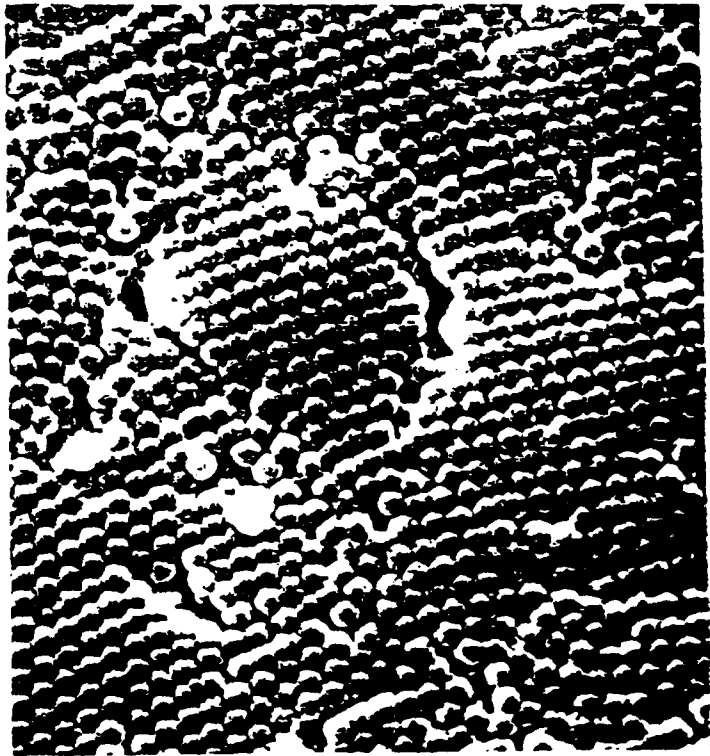
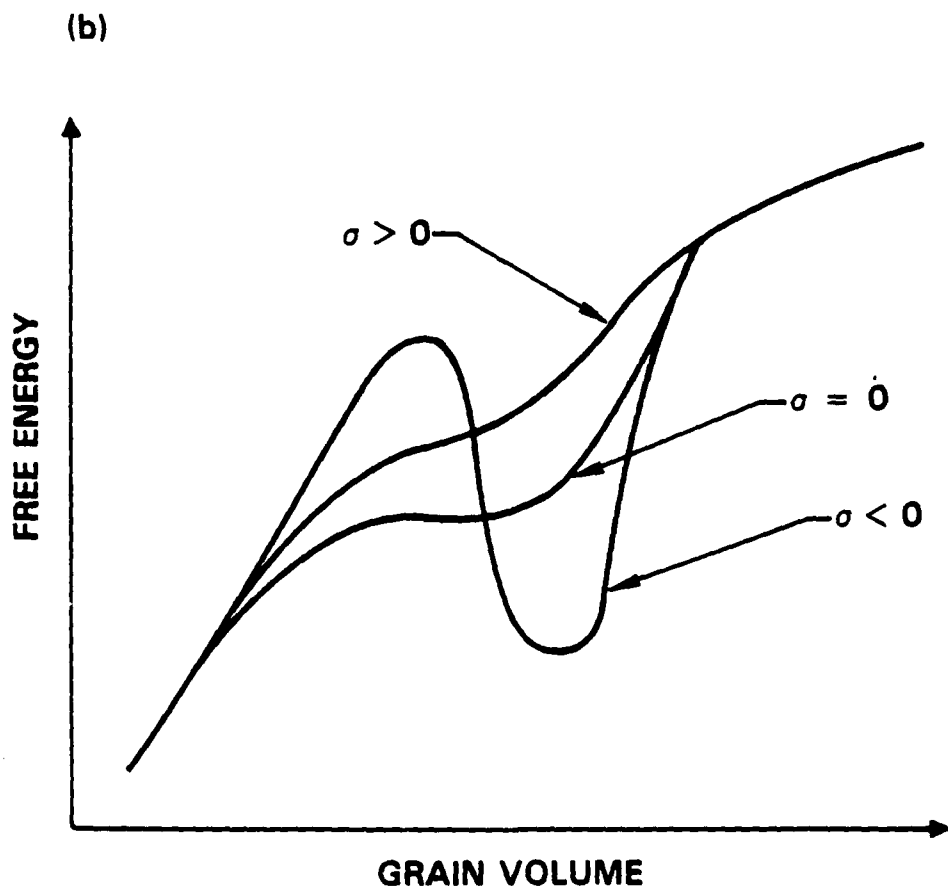
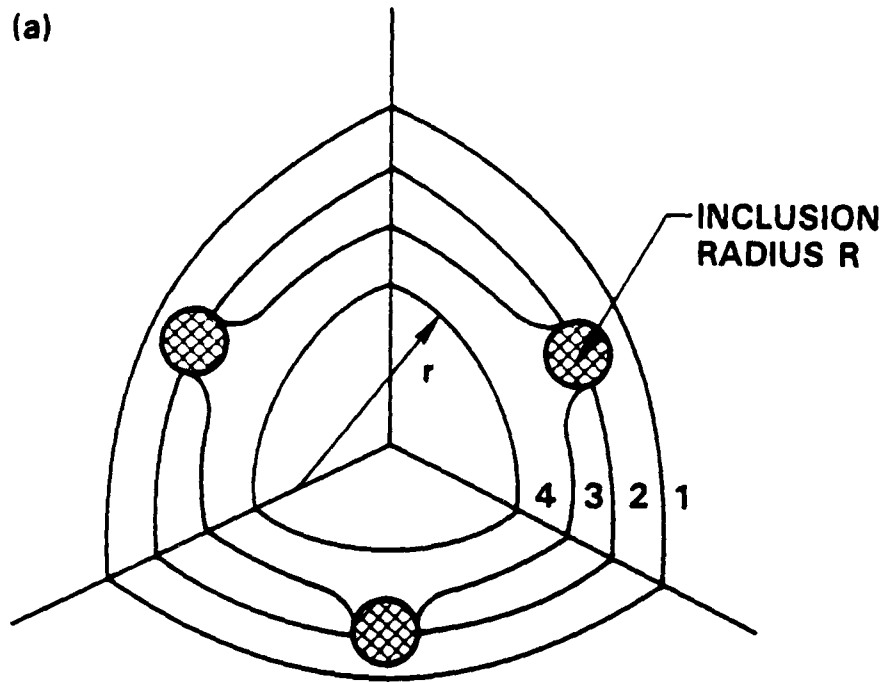


Fig. 13. F.F. 13



F_{113}, F_{112}

SC84-27394



Fig. 14, F. F. Lang